INFLUENCE OF CARBON NANOSTRUCTURES IN PHOTOELECTROCATALYTIC WATER-SPLITTING OF ZnO PHOTOANODES

TEH SWE JYAN

INSTITUTE OF GRADUATE STUDIES
UNIVERSITY OF MALAYA
KUALA LUMPUR

2017

INFLUENCE OF CARBON NANOSTRUCTURES IN PHOTOELECTROCATALYTIC WATER-SPLITTING OF ZnO PHOTOANODES

TEH SWE JYAN

THESIS SUBMITTED IN FULFILMENT OF THE REQUIREMENTS FOR THE DEGREE OF DOCTOR OF PHILOSOPHY

INSTITUTE OF GRADUATE STUDIES
UNIVERSITY OF MALAYA
KUALA LUMPUR

2017

UNIVERSITY OF MALAYA

ORIGINAL LITERARY WORK DECLARATION

Name of Candidate: **TEH SWE JYAN** (I.C/Passport No: [redacted])

Matric No: **HHC130009**

Name of Degree: **Doctor of Philosophy (Ph.D.)**

Title of Project Thesis ("this Work"):

Influence of Carbon Nanostructures in Photoelectrocatalytic Water-splitting of ZnO Photoanodes

Field of Study: **Nanotechnology**

I do solemnly and sincerely declare that:

(1) I am the sole author/writer of this Work;
(2) This Work is original;
(3) Any use of any work in which copyright exists was done by way of fair dealing and for permitted purposes and any excerpt or extract from, or reference to or reproduction of any copyright work has been disclosed expressly and sufficiently and the title of the Work and its authorship have been acknowledged in this Work;
(4) I do not have any actual knowledge nor do I ought reasonably to know that the making of this work constitutes an infringement of any copyright work;
(5) I hereby assign all and every rights in the copyright to this Work to the University of Malaya ("UM"), who henceforth shall be owner of the copyright in this Work and that any reproduction or use in any form or by any means whatsoever is prohibited without the written consent of UM having been first had and obtained;
(6) I am fully aware that if in the course of making this Work I have infringed any copyright whether intentionally or otherwise, I may be subject to legal action or any other action as may be determined by UM.

Candidate's Signature Date:

Subscribed and solemnly declared before,

Witness's Signature Date:

Name:

Designation:

ABSTRACT

Photoelectrocatalytic (PEC) water-splitting is an active field of research as a sustainable technology utilising solar energy to produce hydrogen, H_2 fuel from water. The application of nanostructured carbon materials e.g. reduced graphene oxide (rGO) as promoters for PEC water-splitting photoelectrodes offers many advantages such as cost-effectiveness, chemical stability and tunable properties. Nanostructured carbons obtained from the hydrothermal carbonisation (HTC) of renewable carbon precursors (HTC-biocarbon) shows interesting catalytic activity but its poor electroconductivity limits its application in PEC water-splitting; thus, efforts to increase the sp^2 content and diffusion distance may enhance its potential application as promoter for PEC water-splitting. As such, the present thesis sought to investigate the optimal conditions for preparing electrochemically reduced GO (rGO) for the synthesis of rGO-hybridised ZnO photoanodes. Also, HTC-biocarbons were produced using $ZnCl_2$/NaCl and polyvinyl alcohol (PVA) in the hydrothermal carbonisation of renewable carbon precursors for the purpose of modifying the sp^2 content and morphology of the HTC-biocarbon product, respectively. The Ph.D. project was carried out to achieve the following objectives: (1) To identify the potential of HTC-biocarbon materials prepared through modified HTC synthesis method as carbon-based promoter for PEC water-splitting photoanodes and (2) To identify optimum preparation methods to obtain higher photoelectric performances in carbon-supported ZnO photoanodes. The effect of modifying the HTC process with $ZnCl_2$/NaCl activating agent and PVA soft template on the sp^2 content and morphology of the HTC-biocarbon was investigated. In this study, a porous HTC-biocarbon with surface area up to 597.6 $m^2\ g^{-1}$ was prepared using $ZnCl_2$/NaCl as activating agent in the HTC of oil palm shell fibre. An increase in sp^2 content was observed with increasing temperature and in the presence of activating

agent. The application of PVA as soft template changed the morphology of the HTC-biocarbon product to form a hybrid carbon-carbon structure, consisting of graphene-like sheets and carbonaceous microspheres. rGO-hybridised ZnO thin films were prepared using electrochemical reduction of GO and electrodeposition to deposit the rGO and ZnO layers, respectively. The thin films were prepared in two configurations i.e. (1) ZnO grown on rGO (rGO/ZnO) and (2) rGO coated on ZnO (ZnO/rGO), in order to investigate the effect of layer ordering on the Applied Bias Photon-to-Current Efficiency (ABPE). The rGO/ZnO sample demonstrated the highest ABPE of 0.89 %, due to enhanced electron transfer at the collector-semiconductor interface. The effect of GO electrochemical reduction method was further investigated for rGO/ZnO thin films. It was found that rGO prepared under high flux and rate-controlled conditions during the electrochemical reduction of GO resulted in optimum photo-conversion efficiency in rGO/ZnO films. The highest photocurrent density was observed for rGO/ZnO prepared using CV(1,1) and CV(10,50) ERGO films, at 0.73 and 0.69 mA cm^{-2} respectively. The onset potential of ZnO was reduced from -0.46 to -0.56 V vs Ag/AgCl for the rGO/ZnO film prepared using CV(10,50), which suggested that rGO/ZnO film prepared using CV(10,50) ERGO film provided the lowest overpotential for the oxygen evolution reaction (OER). The scan rate, number of scan cycles, duration and applied potential are important parameters which allow control between diffusion- and rate-controlled reactions.

ABSTRAK

Photoelectrocatalytic (PEC) water-splitting merupakan suatu teknologi mapan yang giat diselidiki untuk menghasilkan bahan api gas hidrogen, H_2 daripada H_2O. Penggunaan bahan karbon bersaiz nano, contohnya grafena oksida terturun (*reduced graphene oxide, rGO*) untuk meningkatkan kadar tindakbalas penghasilan H_2 daripada H_2O menawarkan pelbagai kelebihan seperti kos yang berpatutan, kestabilan kimia dan ciri-ciri permukaan yang boleh dikawal. *HTC-biocarbon*, iaitu produk bahan karbon bersaiz nano yang diperolehi daripada kaedah karbonisasi hidrotermal (HTC), menunjukkan aktiviti pemangkinan yang menarik tetapi ciri-ciri kekonduksian elektriknya menghadkan penggunaannya untuk menggalakkan tindakbalas redoks pada permukaan fotoelektrod. Oleh itu, usaha-usaha untuk meningkatkan kandungan sp^2 serta jarak resapan (*diffusion distance*) boleh meningkatkan potensinya sebagai penggalak (*promoter*) tindakbalas penghasilan H_2 daripada H_2O. Oleh itu, kajian ini bertujuan untuk menyiasat keadaan yang optimum untuk menyediakan rGO menggunakan kaedah electrokimia untuk digunakan dalam penyediaan fotoanod komposit rGO-ZnO. Sampel *HTC-biocarbon* telah dihasilkan menggunakan $ZnCl_2$/NaCl dan polivinil alkohol (PVA) untuk tujuan mengubahsuai kandungan sp^2 dan morfologi produk *HTC-biocarbon*. Projek Ph.D. ini telah dijalankan untuk mencapai objektif berikut: (1) Untuk mengenal pasti potensi sampel *HTC-biocarbon* yang disediakan menggunakan kaedah HTC terubahsuai untuk menggalakkan tindakbalas di permukaan fotoanod, dan (2) Untuk mengenal pasti kaedah penyediaan yang optimum untuk mendapatkan prestasi fotoelektrik yang lebih tinggi daripada fotoanod komposit rGO-ZnO. Kesan mengubahsuai proses HTC dengan $ZnCl_2$/NaCl (ejen pengaktifan) dan PVA (acuan) terhadap kandungan *sp2* dan morfologi *HTC-biocarbon* disiasat. Dalam kajian ini, produk HTC-Biocarbon berrongga yang mempunyai kawasan permukaan sebanyak

597.6 m^2 g^{-1} dihasilkan daripada sabut kelapa sawit menggunakan $ZnCl_2$/NaCl sebagai ejen pengaktifan. Peningkatan kandungan sp^2 diperhatikan apabila ejen pengaktifan digunakan dalam proses HTC, dan apabila suhu dinaikkan. Penggunaan PVA sebagai acuan mengubah morfologi produk *HTC-biocarbon* untuk membentuk karbon berstruktur hibrid yang berbentuk mikrosfera dan lembaran. Filem nipis komposit rGO-ZnO telah disediakan dengan menggunakan kaedah penurunan elektrokimia dan pengelektroenapan (*electrodeposition*). Filem-filem nipis telah disediakan dalam dua konfigurasi iaitu (1) ZnO dienap di atas rGO (rGO/ZnO) dan (2) rGO disalut pada ZnO (ZnO/rGO), untuk mengkaji kesan lapisan penukaran konfigurasi terhadap prestasi *Applied Bias Photon-to-Current Efficiency* (ABPE). Sampel rGO/ZnO menunjukkan prestasi ABPE yang paling tinggi, iaitu 0.89%, disebabkan oleh peningkatan ciri-ciri pemindahan caj di kawasan antaramuka pengumpul-semikonduktor. Kesan kaedah penurunan elektrokimia disiasat terhadap filem nipis rGO/ZnO. Kajian ini mendapati bahawa rGO yang disediakan di dalam keadaan fluks yang tinggi dan kadar tindakbalas yang terkawal menghasilkan kecekapan photo-penukaran yang optimum untuk rGO/ZnO. Ketumpatan arusfoto tertinggi diperhatikan untuk sampel rGO/ZnO disediakan menggunakan kaedah CV (1,1) dan CV (10,50), iaitu 0.73 dan 0.69 mA cm^{-2} masing-masing. Filem rGO/ZnO yang disediakan menggunakan filem CV (10,50) ERGO mendemonstrasikan tenaga pengaktifan yang terendah untuk OER, sepertimana ditunjukkan oleh peralihan fotovoltan dari -0.46 ke -0.56 V vs Ag/AgCl untuk filem ZnO and rGO/ZnO, masing-masing. Kadar imbasan, bilangan kitaran imbasan, tempoh dan voltan yang dikenakan adalah parameter penting yang membolehkan kawalan kadar tindakbalas.

ACKNOWLEDGEMENTS

The completion of this work has been made possible by the support of many, and I am truly thankful to the following people who have played a significant role along this doctoral journey:

To Professor Dr. Sharifah Bee Abdul Hamid, I am inspired by your passion, dedication and success in research. Thank you for the honour to work under your supervision, and for believing in me to achieve more than I myself could imagine. To Dr. Lai Chin Wei, your spirit of excellence in research encourages me to strive for the same in my own career. I am grateful for your comprehensive advice towards the completion of this work. I also thank the University of Malaya for their generous support through grants RP022-2012-A (UMRG) and H-21001-F0032 (HIR).

The completion of this undertaking could not have been possible without the contribution of valuable research expertise from Dr. Zaira Zaman Chowdhury, Dr. Lee Kian Mun, Dr. Md. Rakibul Hasan and Dr. Samira Bagheri towards the development of this project. To the dedicated staff at the Nanotechnology and Catalysis Research Centre (NANOCAT): thank you for your service and technical support, and for always delivering with a cheerful heart.

To my family, thank you for being the best moral support team ever. To the friends I have met at NANOCAT, I count it my privilege to walk together with you along this journey.

To Almighty God, thank You for enabling me to grow into the person I am today, through Your gifts of Life, Hope and Strength.

TABLE OF CONTENTS

LIST OF FIGURES

LIST OF TABLES

LIST OF SYMBOLS AND ABBREVIATIONS

BET	:	Brunauer-Emmett-Teller
CB	:	Conduction band
CVD	:	Chemical vapour deposition
DMF	:	Dimethylformamide
EIS	:	Electrochemical impedance spectroscopy
ERGO	:	Electrochemically-reduced graphene oxide
FESEM	:	Field emission scanning electron microscopy
FTO	:	Fluorine-doped tin oxide
GO	:	Graphene oxide
HER	:	Hydrogen evolution reaction
HTC	:	Hydrothermal carbonisation
ITO	:	Indium-doped tin oxide
J_{SC}	:	Short-circuit current density
NC	:	Nanostructured carbon
OER	:	Oxygen evolution reaction
PEC	:	Photoelectrocatalytic
PCD	:	Photocurrent density
PL	:	Photoluminescence
PV	:	Photovoltaic
PVA	:	Polyvinyl alcohol
rGO	:	Reduced graphene oxide
ROI	:	Return-of-investment
STH	:	Solar-to-H_2
UV-Vis	:	UV-Visible

VB : Valence band

V_O : Oxygen vacancy

V_{OC} : Open circuit potential

VOC : Volatile organic compound

XRD : X-ray diffraction

ZnO : Zinc oxide

CHAPTER 1: INTRODUCTION

The unique characteristics of ZnO offers potential for photocatalytic applications, such as photoelectrocatalytic (PEC) water-splitting. However, practical issues such as limited usage of the light spectrum, recombination and photocorrosion inhibit the widespread use of ZnO as photoanode material in PEC water-splitting systems (J. Yang et al., 2013). For this reason, innovative approaches are in demand to increase the overall catalytic activity of ZnO photoanodes (and metal oxide photoelectrodes in general) in an affordable manner. This Introduction begins by presenting the motivation of enhancing ZnO as a potential photocatalyst material, as well as the justification behind selecting carbon-based promoters to enhance the photocatalytic ability of ZnO. The chapter ends with a disclosure of the thesis' research objectives, scope of research and outline.

1.1 Research Background

PEC water-splitting is a technology that relies on renewable solar energy to produce hydrogen, H_2 fuel from water. Similar to the electrolytic cell, a PEC water-splitting cell consists of two electrodes immersed in an electrolyte (H_2O) and is connected together through an external circuit. The electrodes in a PEC water-splitting cell are photocatalytically-active and generates charged species (i.e. photoexcited electrons and holes) at its surface, enabling water molecules and protons to undergo redox reactions, forming H_2 and O_2 at the cathode and anode, respectively (Gratzel, 2001). Hence, electrodes which respond to light are also referred to as photoelectrodes. PEC water-splitting has been first demonstrated by Fujishima and Honda, who produced the first

viable PEC water-splitting cell with an approximate quantum efficiency of 0.1 %. To date, we have been able to achieve solar-to-H_2 (STH) efficiencies of 12.7 % using a p-$GaInP_2$/GaAs electrode as photoanode (Oscar Khaselev and Turner, 1998), and the record has only recently been surpassed to 14 % using a Z-scheme tandem cell comprised of Rh-functionalised $AlInPO_x$ photocathode and RuO_2 as photoanode (May et al., 2015).

The development of PEC water-splitting technology will be able to replace unsustainable, conventional H_2 production methods to support industries of significant economic value. Three primary techniques are currently used to produce H_2 at the commercial scale: (1) extraction from fossil fuels (van Heek, 2000), (2) steam reformation of hydrocarbons (Braga et al., 2013; Cortright et al., 2002; D. Wang et al., 1998) and (3) electrolysis (Carmo et al., 2013). Producing H_2 from fossil fuels is four times more expensive than using the fuel itself, whereas, the water-gas shift reaction produces carbon emissions. Electrolysis has since become a potential candidate for green H_2 production, although only a small proportion of the current H_2 production originates from electrolysis, i.e. the contribution of H_2 production through electrolysis stands at 4% compared to 48%, 30% and 18% from natural gas, oil and coal, respectively (R. Gupta, 2008). The limited application of electrolysis is mainly attributed to its high electricity consumption, cost and maintenance (Zeng and Zhang, 2010), although the sustainability of the electrolysis process was subsequently improved by sourcing electricity from renewable sources e.g. photovoltaics (PV), hydro and wind (Carrasco et al., 2006; O. Khaselev et al., 2001).

The development of sustainable H_2 production technologies will support the manufacturing of ammonia (Leigh, 2004; Modak, 2002), hydrogenation of unsaturated lipids for food and fuel products e.g. margarine and biodiesel (Coenen, 1976; Sugami et

al., 2016; Veldsink et al., 1997), as well as refined petroleum products (Duerksen, 1992; Murphree et al., 1940). H_2 has also been identified as a promising clean energy carrier due to its high energy conversion efficiency, ease of production and practical storage requirements: liquid H_2 possesses the highest specific energy of 33.3 kWh/kg, compared to 13.9, 12.8 and 12.6 kWh/kg for liquid natural gas, diesel and petrol, respectively (Edwards et al., 2008). The projected energy storage of H_2 also exceeds lithium ion batteries, redox flow batteries and compressed air energy storage options (US Department of Energy, 2013).

The development of efficient photocatalysts i.e. photoelectrode materials lie at the heart of a reliable PEC water-splitting system. Therefore, the development of metal oxide photocatalysts as cost-effective photoelectrode materials for PEC water-splitting will have far-reaching impacts to society. A suitable candidate as a photoanode for H_2 production must satisfy three basic requirements: (1) the band gap has to be higher than 1.23 eV, (2) suitable band-edge potentials with respect to OH^- oxidation potential, and (3) stable against photocorrosion (Juodkazis et al., 2010; Walter et al., 2010). A variety of materials have been investigated, including transition metal oxides (e.g. ZnO, Fe_2O_3, Cu_2O, WO_3) and perovskites (e.g. $BaTi_4O_9$, $K_4Nb_6O_{17}$, $SrTiO_3$, ZrO_2, Ta_2O_5, $K_2Ti_6O_{13}$, TaON, $In_{1-x}Ni_xTaO_4$, $BaZn_{1/3}Nb_{2/3}O_3$). ZnO has also emerged as a leading candidate as cost-effective photoanode material for PEC water-splitting.

1.2 Problem Statement

ZnO is an n-type, direct band gap material with a theoretical band gap width of 3.37 eV (Srikant and Clarke, 1998). As a result, ZnO possesses photocatalytic abilities, i.e. it can absorb solar energy and photoexcite electrons from the valence band (VB). The high electron mobility of ZnO allows for effective charge separation, forming vacant

sites at the VB of ZnO. Fast transport of photoexcited electrons across the bulk crystal corresponds with effective charge separation (Jayah et al., 2015), and this property is desirable to prevent loss of energy caused by radiative, Shockley-Hall-Read or Auger recombination. ZnO offers higher electron mobility compared to other metal oxide semiconductor materials, due to the formation of large conduction band (CB) dispersion caused by the stabilisation of d^{10} orbitals with Zn s and p orbitals (Hisatomi et al., 2014; Inoue, 2009). Thus, effective charge separation causes vacant sites i.e. "holes" to accumulate at the electrode surface. These holes located at the ZnO VB (highest occupied molecular orbital, HOMO) possess sufficient energy (overpotential) to oxidise OH^- species (accept electrons from OH^-), which is the basis of the oxygen evolution reaction (OER) in PEC water-splitting reactions.

Nevertheless, ZnO suffers from the drawback of high recombination rate of photogenerated electron-hole pairs, whereby OH and H bonds at the surface of the ZnO crystal were found to facilitate the recombination process (L. L. Yang et al., 2010). Efforts to facilitate the efficient separation of photogenerated electron-holes will, in effect, reduce its recombination rate (X. Zhang et al., 2014). Moreover, the well-known photocorrosion of ZnO often leads to a decrease in the photostability of ZnO under prolonged light irradiation (Rudd and Breslin, 2000; Sapkal et al., 2012). Therefore, it is crucial to design synthesis strategies to enhance the charge separation of photoexcited electron hole pairs and ultimately, photocatalytic activity.

Strategies to control the particle size and incorporate extrinsic modifiers have been proposed to enhance the photocatalytic activity of ZnO and metal oxides in general. Controlling the size of ZnO particles to the nanoscale have been useful to reduce the recombination of photo-excited electron-hole pairs (by limiting the diffusion distances for charge carriers to reach active surface sites) and increase the surface active area.

Extrinsic modifications such as adding dopants, co-catalysts and photosensitisers to ZnO have effectively enhanced its photocatalytic ability by changing the material's band gap width and position, as well as electron mobility. However, the available co-catalysts and photosensitisers such as CdSe are often rare, toxic or unstable. The development of abundant and sustainable extrinsic modifiers is one key area to improve the electron transport properties of ZnO and metal oxides in general.

Consequently, carbon-based promoters are actively considered as alternative co-catalysts and sensitisers materials. Many reports account the improvement of solar-to-H_2 efficiencies due to enhanced, nanostructured carbon-hybridised ZnO photoanodes (C. Han et al., 2014; Liwu Zhang et al., 2009a). The hybridisation between carbon materials and ZnO has demonstrated improved anti-photocorrosion ability due to the following strategies: by anchoring fullerene, C_{60} on vacant O sites on the ZnO crystal surface (Fu et al., 2008), increasing the availability of redox species to increase competition against ZnO dissolution (Liwu Zhang et al., 2009a) and passivation layer through C-O bond formation (Yanhui Zhang et al., 2013c). Coupling ZnO with carbon materials could also greatly improve the photocatalytic performance of ZnO, either as a photoelectron reservoir to transfer the photogenerated electrons from the metal oxide (Khoa et al., 2015), or act as an organic dye-like macromolecular ''photosensitiser'' (M.-Q. Yang and Xu, 2013). The impacts of nanostructured carbon hybridisation is not limited to ZnO, as other metal oxides e.g. TiO_2 and CdTe also demonstrated improved electron transfer as a result of hybridisation with graphene and graphene oxide (GO) (Du et al., 2011; W. Fan et al., 2011; Kaniyankandy et al., 2012).

1.3 Research Objective

The preparation of ZnO nanostructures hybridised with carbon-based promoters offers a sustainable, metal-free option to overcome issues limiting its photocatalytic activity. A systematic investigation would be beneficial to determine an optimum preparation method of carbon-ZnO hybrid materials, in order to produce maximum photo-conversion efficiency.

Therefore, the objectives of the project were as follows:

1. To identify the potential of HTC-biocarbon materials prepared through modified hydrothermal carbonisation (HTC) synthesis method as carbon-based promoter for PEC water-splitting photoanodes.
2. To identify optimum preparation methods to obtain higher photoelectric performances in carbon-supported ZnO photoanodes.

1.4 Scope of Research

The scope of this work involved the preparation of nanostructured carbon using various chemical agents in the HTC process. The chemical agents were selected based on their role as activating agent and soft scaffolding template. As this project utilised the HTC technique and renewable carbon feedstocks, the nanostructured carbons prepared in this project are referred to as HTC-biocarbons, with the prefix “bio-” indicating the natural origin of the carbon feedstock. The HTC-biocarbon products are characterized for its physical and chemical properties (morphology, crystallinity, chemical bonding, optical absorbance, thermal stability, surface area). Subsequently, the role of rGO and HTC-biocarbons to promote PEC water-splitting was investigated beginning with the preparation of rGO-hybridised and HTC-biocarbon-hybridised ZnO

photoanodes. The chemical and physical properties of the hybridised ZnO photoanodes were analysed using X-ray diffraction (XRD), Raman spectroscopy, photoluminescence (PL) spectroscopy, UV-Visible (UV-Vis) spectroscopy, field emission scanning electron microscopy (FESEM). The effect of rGO and HTC-biocarbons on the charge-transfer properties of hybridised ZnO photoanodes were determined by electrochemical characterisation techniques i.e. electrochemical impedance spectroscopy (EIS) and chronoamperometry.

1.5 Outline of Thesis

The findings of this Ph.D. project is outlined as follows. In Chapter 2, a summary of the state-of-the-art in nanostructured carbon synthesis and enhancement of photoelectrocatalysts are presented, highlighting potential areas for research. This section also highlights key research fundamentals and directions from scientific literature which informed the experimental design process in order to achieve each research objective in the Ph.D. project. As this Ph.D. thesis is organized following an article-based format, Chapter 3 presents the preparation methods and properties of HTC-biocarbons *via* $ZnCl_2$/NaCl-activated and PVA-assisted HTC. Chapter 4 summarises the findings obtained from an investigation into the promoting effect of rGO in ZnO thin film photoanodes to enhance photoelectrocatalytic water-splitting. Subsequently, the effect of layer ordering as well as the potential of HTC-biocarbon as surface passivation material are explored in Chapter 5. The thesis concludes with a synthesis of the research findings in Chapter 6.

CHAPTER 2: LITERATURE REVIEW

2.1 Fundamentals of PEC water-splitting

A PEC water-splitting device utilizes solar energy to drive redox reactions in the OER and HER reactions. Various components are necessary to ensure the device produces H_2 successfully. In this section, the working principle of PEC water-splitting is explained according to the function of each component in a PEC water splitting device, criteria for selecting a photoanode material, as well as an overview of the OER mechanism.

2.1.1 Anode/Photoanode

An anode is the electrode where the OER takes place i.e. H_2O and/or OH^- ions are oxidised to form O_2. If solar energy is used to enable the electrode to oxidise water molecules, then the electrode is called a photoanode. Photoanodes are usually made up of n-type transition metal oxides such as ZnO and TiO_2 (Alexander et al., 2008; Trotochaud et al., 2012), due to its ability to favour the OER process, and its abundance potentially reduces the cost of manufacture.

The band gap structure of n-type semiconductors favours the OER process primarily because of the formation of a Schottky barrier at the electrode-electrolyte interface. When an electron-rich, n-type semiconductor is immersed into an aqueous electrolyte, a transfer of charges occur between the electrode and electrolyte until an equilibrium in Fermi energy levels is achieved (Bott, 1998). At equilibrium, the surface of the n-type semiconductor is electron-deficient, and this region is referred to as the depletion layer, space-charge region or Schottky barrier (Gratzel, 2001). When the metal oxide absorbs

a photon with energy equal to or greater than its band gap, an electron is excited from the VB to the CB, generating a positively-charged hole in the VB (step ①, Figure 2.1). In the case of ZnO, photons must possess a minimum energy of 3.37 eV in order to excite electrons to the CB. Subsequently, the photoexcited electrons migrate away from the site of excitation towards the cathode/photocathode in a process called charge separation (step ②, Figure 2.1). The Schottky barrier formed at the semiconductor-electrolyte interface supports the unidirectional flow of photoexcited electrons towards the cathode/photocathode. The positively-charged holes that remain on the surface of the semiconductor act as active sites for the adsorption and oxidation of H_2O and OH^- species under acidic and alkaline electrolyte conditions, respectively (step ③, Figure 2.1).

2.1.2 Cathode/Photocathode

The reduction of H^+ ions to H_2 molecules i.e. the HER process takes place at the cathode (step④, Figure 2.1). Pt, Ir and Ru are the most efficient cathode materials available to catalyse the OER and HER processes, but are too expensive to be applied on a commercial scale. The electrode is called a photoanode if solar energy is used to enable the electrode to reduce protons. Complementary to the photoanode, the photocathode usually comprises of a p-type semiconductor which is able to form an electron-rich layer at the semiconductor-electrolyte interface and supply electrons to the H^+ species (Bott, 1998).

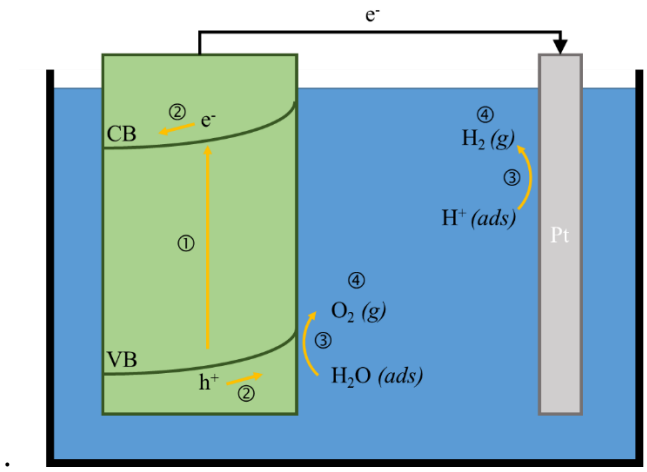

Figure 2.1 Schematic diagram of PEC water-splitting mechanism in an electrochemical cell comprising an n-type photoanode (e.g. ZnO) and Pt cathode immersed in an aqueous electrolyte.

2.1.3 Electrolyte and External Circuit

The various arrangements of photoelectrodes in a PEC water-splitting cell are summarised in Figure 2.2: (a) photoanode made of an n-type metal oxide and a metal cathode, (b) photocathode made of a p-type metal oxide and a metal anode, and (c) photoanode made of an n-type metal oxide and a photocathode made of a p-type metal oxide. Essentially, the electrodes (anode/photoanode and cathode/photocathode) are connected to each other via an external circuit to allow for electron transport from the anode/photoanode to the cathode/photocathode, and immersed in the electrolyte to allow for ion migration.

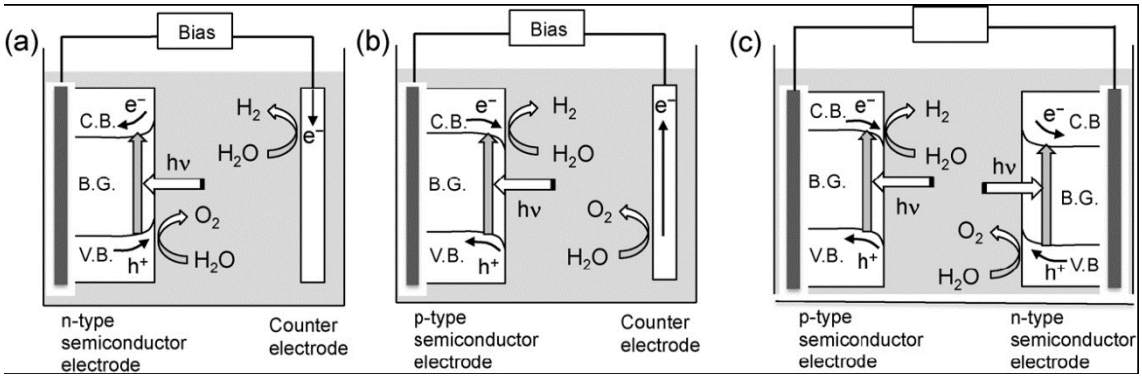

Figure 2.2 Photoelectrochemical water-splitting systems using (a) n-type metal oxide photoanode, (b) p-type metal oxide photocathode, and (c) tandem system under solar illumination (Abe, 2010)

In general, the PEC water-splitting reaction occurs by the following mechanism (Suib, 2013):

Photon Absorption:	$2h\nu \rightarrow 2e^- + 2h^+$	
Anode:	$H_2O + 2h^+ \rightarrow {}^1/_2O_2 + 2H^+$	E°= +1.23 V vs NHE at pH 0
Cathode:	$2H^+ + 2e^- \rightarrow H_2$	E°= 0.00 V vs NHE at pH 0
Overall:	$\mathbf{H_2O + 2h\nu \rightarrow H_2 + {}^1/_2O_2}$	E°= +1.23 V vs NHE at pH 0

2.1.4 Selection criteria for photoanode materials

The search for suitable materials to catalyse the OER process is an active area of research, and one that is motivated by the opportunity to design and synthesise alternative catalysts that can operate at acceptable catalytic activities compared to noble metal electrodes (Ru, Ir and Pt), but at the fraction of the cost. Thus, an efficient photoanode should possess the following properties:

- A suitable band gap energy and position to allow for absorption of solar energy over a broad range of wavelengths.

- Sufficient reactive sites at the surface of the photoanode to allow for high turnover number.
- Efficient charge transport is necessary to prevent recombining *via* inter-band transition or charge trapping at recombination centres within the crystal lattice.
- The PEC water-splitting system should also take into consideration conditions which are able to retard the recombination of H_2 and O_2 to form H_2O (Abe et al., 2003).
- Stable during the PEC or photocatalytic reactions to ensure long-term durability of the system.

The successful design and implementation of affordable catalysts towards the OER process will be able to further increase the STH conversion efficiency and ultimately, increase the rate of H_2 production.

2.1.5 Mechanism of the OER

Various mechanisms have been proposed in an attempt to elucidate a detailed interaction between primary reactants, intermediate species and products with catalytically active materials e.g. metal and metal oxides (J. O. Bockris and Otagawa, 1983; J. O'M. Bockris and Huq, 1956; Damjanovic et al., 1966; Hoare, 1967; Kobussen and Broers, 1981; Krasil'shchikov, 1963). A comparison of the proposed reaction pathways is presented in Table 1, and are categorized according to the following phases: initiation, intermediate reactions and termination.

Table 2.1. Proposed mechanisms of the oxygen evolution reaction

Mechanism	Initiation	Intermediate reactions	Termination
Damjanovic (Damjanovic et al., 1966)	$M + OH^- \rightarrow MOH + e^-$	$MOH + OH^- \rightarrow MO\text{-}H\text{-}OH^-$ $MO\text{-}H\text{-}OH^- \rightarrow MO\text{-}H\text{-}OH + e^-$ $MO\text{-}H\text{-}OH \rightarrow MO + H_2O$ $MO + OH^- \rightarrow MHO_2 + e^-$	$MHO_2 + OH^- \rightarrow M + O_2 + H_2O + e^-$ Or: $2MO \rightarrow O_2 + 2M$
Krasil'shchikov (Krasil'shchikov, 1963)	$M + OH^- \rightarrow MOH + e^-$	$MOH + OH^- \rightarrow MO^- + H_2O$ $MO^- \rightarrow MO + e^-$	$2MO \rightarrow O_2 + 2M$
Hoare (Hoare, 1967)	$M + OH^- \rightarrow MOH + e^-$	$MOH + OH^- \rightarrow MH_2O_2^-$ $2MH_2O_2^- \rightarrow M + MO_2^- + 2H_2O$	$MO_2^- \rightarrow M + O_2 + 2e^-$
Bockris oxide path (John O'M. Bockris and Otagawa, 1984)	$M + OH^- \rightarrow MOH + e^-$	$2MOH \rightarrow MO + M + H_2O$	$2MO \rightarrow 2M + O_2$
Bockris electrochemical oxide path (John O'M. Bockris and Otagawa, 1984)	$M + OH^- \rightarrow MOH + e^-$	$MOH + OH^- \rightarrow MO + H_2O + e^-$	$2MO \rightarrow 2M + O_2$
Kobussen (Kobussen and Broers, 1981)	$M + OH^- \rightarrow MOH + e^-$	$MOH + OH^- \rightarrow MO + H_2O + e^-$ $MO + OH^- \rightarrow MO_2H^-$ $MO_2H^- + OH^- \rightarrow MO_2^- + H_2O + e^-$	$MO_2^- \rightarrow M + O_2 + e^-$

Initiation. All proposed mechanisms begin the OER process with the binding of an OH^- ion to the active catalyst site, forming a metal hydroxide (M-OH) complex.

Intermediate reactions. The M-OH complex may decompose to form adsorbed atomic O (Bockris oxide path). Alternatively, the M-OH complex may undergo nucleophilic attack by a hydroxyl, OH^- ion, leading to the formation of either adsorbed species on the active site: (1) atomic O (Krasil'shchikov, Bockris electrochemical oxide path and Kobussen mechanisms), or (2) H_2O_2 (Damjanovic and Hoare mechanisms). H_2O_2 adsorbed on active sites are proposed to decompose to superoxide anions ($M\text{-}O_2^-$). The Kobussen mechanism features both the formation of atomic O and H_2O_2 as a result of the M-O species being subjected to multiple nucleophilic attack reactions.

Termination. O_2 may be produced either via (1) the formation of O-O bond between two M-O species (Damjanovic, Krasil'shchikov, Bockris oxide and Bockris

electrochemical oxide mechanisms) or (2) the dissociation of O_2 from the $M\text{-}O_2^-$ complex (Hoare and Kobussen mechanisms).

The formation of M-O species is favoured at the surface of metal electrodes as the M-O species is mobile and free to rearrange itself at the surface. Ru, Ir and Pt are the best materials for water splitting due to the optimal binding energy. Although these materials are valued for their optimal binding energy and inertness, the reverse reaction i.e. recombination of H_2 and O_2 are fast reactions, thus limiting the output of O_2 to the rate of O_2 desorption from the electrode surface.

For semiconductor electrodes, the mobility of adsorbed species is restricted and the formation of $M\text{-}O_2^-$ species is favoured in order to circumvent the need for atomic rearrangement leading to O-O bond formation. A recent discovery has been made on the mechanism of OER at hematite surfaces: the Fe^{3+}-OH complex undergoes dehydrogenation to form a Fe^{4+}=O species before interacting with H_2O to form the Fe^{3+}-O-O-H species (Zandi and Hamann, 2016). For a summary on the techniques for measuring catalytic activity and kinetics of the OER process, the reader is referred to an excellent review by Fabbri et al. (Fabbri et al., 2014).

2.2 Strategies to enhance the photocatalytic activity of semiconductors

At present, the solar-to-H_2 (STH) efficiency of current PEC water-splitting photoanodes remain lower compared to commercial PV panels. The STH efficiency is an indicator expressing the amount of solar energy that the device is able to convert into H_2 fuel, and is expressed in the following equation (Dotan et al., 2014):

$$STH = \frac{|J_{SC}\,(mA\,cm^{-2})| \times 1.23(V) \times \eta_f}{P(mA\,cm^{-2})} \qquad \text{(Eq. 2.1)}$$

Whereby J_{sc} is the PCD at short-circuit potential, η_f the Faradaic efficiency for H_2 evolution, and P the power density of incident illumination.

The PV+electrolysis system is able to achieve a 24.4 % STH energy conversion efficiency (Akihiro et al., 2015). In comparison, a monolithic photovoltaic-photoelectrochemical device for H_2 production yielded a H_2 production efficiency of 12.4 % (Oscar Khaselev and Turner, 1998), but has since increased slightly to 14 % using a complex tandem cell comprising Rh-functionalised $AlInPO_x$ photocathode and RuO_2 as photoanode (May et al., 2015). Therefore, to enhance its photocatalytic efficiency, it is of crucial importance to design strategies which can suppress the recombination of electron-hole pairs and photocorrosion of ZnO. Two main research approaches have emerged in the development of photocatalytic materials with improved photon-to-current conversion efficiency (PCE). The first is to extend the ability of photocatalysts to harvest photons in the visible region of the light spectrum (band gap engineering), secondly is to promote effective photogenerated charge separation and transport (Hao Ming Chen et al., 2012).

2.2.1 Band-gap engineering and sensitisation to extend light harvesting

The introduction of foreign ions (cations or anions) into the semiconducting material changes its electronic structure and optical properties. Thus, the energy requirement to generate photoexcited electrons (band gap) can be reduced by introducing a small amount of impurity atoms into the semiconductor crystal lattice (Sengupta et al., 2016). The tuning of electronic properties of metal oxides have been carried out via non-metal doping, transition metal doping and co-doping (Rehman et al., 2009). Non-metal doping, e.g. nitrogen, carbon or sulphur into ZnO, has been extensively studied with a view to narrowing the band gap (W. Yu et al., 2016). The narrowing of the band gap

using non-metal dopants was previously attributed to the mixing of O *2p* states with the dopant's *2p* states, thereby forming occupied states with higher energy in the VB (G. Liu et al., 2010a). The amount of dopant atoms in the metal oxide semiconductors ought to be well-controlled so that the doping does not introduce recombination sites, which affects the lifetime and efficiency of the photoelectrode.

The addition of sensitiser molecules increases the flow of electrons in a water-splitting device. The sensitiser molecules absorb photons at wavelengths different to that of the semiconductor and creates photoexcited electrons, which are then injected into the CB of the semiconductor metal oxide. The optimisation of dyes and quantum dots as sensitiser agents is an active field of research, for the purpose of enhancing the stability and electron injection properties, strengthening the sensitiser-metal oxide bond, and shifting light absorption towards the visible region. There are two classes of dyes, namely organometallic and organic dyes. Both classes are made up of organic chromophores, except that organometallic dyes contain an additional transition metal in the structure. Conventional photosensitisers, e.g. dyes possess poor stability but is valued for its low cost of fabrication (Swiegers et al., 2012). CdS and CdSe quantum dots have demonstrated promising photoconversion efficiency (G.-C. Fan et al., 2016; Yun et al., 2016), but suffers from poor stability due to buildup of sulphur (Licht, 2002). Carbon quantum dots have also recently been considered as an affordable and environmentally-friendly photosensitiser material (Na et al., 2015; D. Sharma et al., 2016).

2.2.2 Enhancing electron transfer properties

When a photoelectrode is exposed to solar irradiation, the electrons in the VB of the semiconductor absorbs electromagnetic energy and is excited into the CB; electron-hole

pairs are generated. These electron-hole pairs ideally participate directly in the PEC water-splitting half reactions. However, we do not observe a 100 % Faradaic efficiency of the photogenerated electron-hole pairs. This is because recombination mechanisms hinder the transport and participation of photoexcited electron-hole pairs in the PEC water-splitting process.

Recombination can occur *via* band-to-band, Shockley-Read-Hall or Auger recombination. Band-to-band recombination occurs when an electron from the CB directly combines with a hole in the VB releases its energy in the form of a photon (Figure 2.3a). Shockley-Read-Hall recombination is also referred to as trap-assisted recombination, as this form of recombination occurs in the presence of defects in the semiconductor crystal lattice (Figure 2.3b). Defects in a crystal can introduce an energy state in the forbidden region between the VB and CB. Charge carriers recombine at this intermediate energy state with the release of phonons instead of photons. The Shockley-Read-Hall effect applies also to traps at the electrode surface. The abrupt termination of the semiconductor crystal results in a large number of electrically active states, i.e. recombination centres. In addition, the surfaces and interfaces are more likely to contain impurities since they are exposed during the device fabrication process. Auger recombination is the phenomenon whereby the energy released when an electron and hole recombine is transferred to a third electron, instead of emitting a photon (Figure 2.3c). Auger recombination limits the lifetime and ultimate efficiency of photoelectrodes.

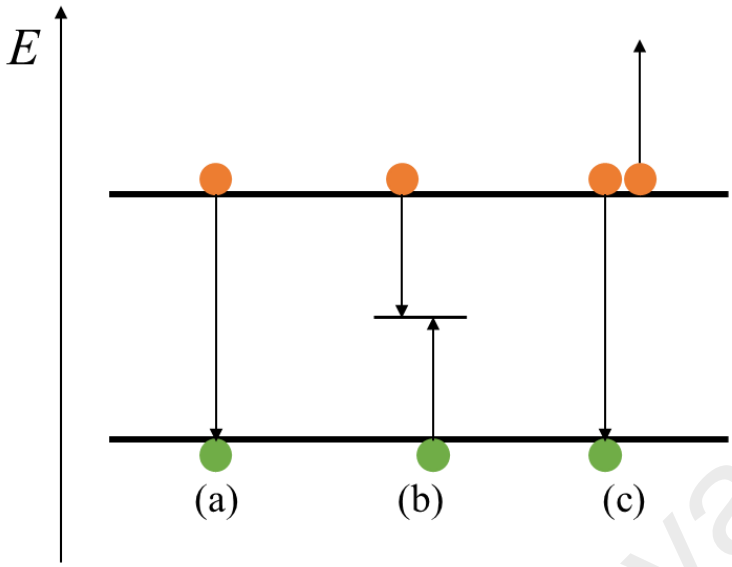

Figure 2.3 Schematic diagram depicting (a) band-to-band, (b) Shockley-Read-Hall and (c) Auger recombination

Electron transfer properties are affected by the nature of the interface between electron transfer agent and catalyst interface. Charge transfer can be modulated according to the work function, defects and doping in the semiconductor material (Yongqing Cai and Feng, 2016). When two materials with varying work functions are placed in contact with each other, electrons tend to transfer from materials with smaller work functions to the material with a larger work function (Harinipriya and Sangaranarayanan, 2002; Menamparambath et al., 2014). The presence of dopants and defects such as oxygen vacancies (V_o) introduces new energy states into the band structure of the semiconductor and may shift the Fermi level upwards or downwards (M. X. Chen et al., 2016; X.-X. Gao et al., 2016). The application of an external bias on the semiconductor material affects the degree of band-bending at the metal-semiconductor interface and ultimately, the charge distribution at the semiconductor-electrolyte interface (Zhen Zhang and Yates, 2012). The electric field was able to depress the electron-hole recombination rate and increase hole availability at the TiO_2 solution interface (Yi et al., 2008). Similarly, the formation of hybrid materials may also

affect the band bending properties and carrier transport across the heterojunction interface, facilitating the separation of electron-hole pairs and suppressing recombination (Singh et al., 2016; J.-S. Yang and Wu, 2017; J. Zhang et al., 2017).

Hence, the general strategies to suppress recombination include reducing the amount of defects in the crystal lattice, and controlling photocatalyst particle size to the nanoscale and modulating the electric properties at the interfaces (Jafari et al., 2016). Defects at the surface and bulk serve as trapping sites for electrons or holes and facilitate recombination. Secondly, nanosized materials possess short diffusion distances thus reducing the probability of charge trapping. Additionally, the modulation of the localised electric field through the formation of heterojunctions is another strategy to facilitate efficient electron transfer in a semiconductor photocatalyst. A summary of the various strategies used (metal- and carbon-based) to enhance the PCE of ZnO is presented in Table 2.1, for comparison.

Table 2.1 Summary of modification strategies to enhance ZnO photocurrent density

Structure	Preparation method	Enhancement strategy	Electrolyte	Reference electrode	Photocurrent density (mA cm^{-2})			Ref.
					Applied potential (V)	Control electrode	Modified electrode	
ZnO nanorods	Electrochemical deposition + photochemical deposition	Cobalt phosphate co-catalyst	0.1M K_3PO_4	Ag/AgCl	0.0	0.009	0.023	(Steinmiller and Choi, 2009)
ZnO nanorod @nanoplatelet core-shell array	Hydrothermal + photoreduction	Au co-catalyst	0.5M Na_2SO_4	SCE	0.6	0.01	0.06	(C. Zhang et al., 2015a)
ZnO film	Electron-beam glancing angle deposition	Crystal growth method	0.5M $NaClO_4$	Ag/AgCl	1.0	0.045	0.142	(Wolcott et al., 2009)
ZnO nanowires	Hydrothermal + sol-gel	TiO_2 heterojunction	0.1M NaOH	RHE	0.85	0.08	0.19	(Hernández et al., 2014)
ZnO nanorods	Hydrothermal	MWCNT hybridisation	0.5M Na_2SO_4	Ag/AgCl	0.0	0.06	0.25	(Tian et al., 2012)
ZnO nanorods	Hydrothermal + electron beam evaporation	Ag co-catalyst	0.5M Na_2SO_4	Ag/AgCl	0.0	0.089	0.325	(Y. Wei et al., 2012)
ZnO nanowires	Hydrothermal	Graphene quantum dot photosensitiser	0.5M Na_2SO_4	-	0.6	0.11	0.34	(Guo et al., 2013)
ZnO film	Spray pyrolysis	Cu-doping	0.5M NaOH	SCE	0.6	0.05	0.35	(Dom et al., 2013)
ZnO nanowires	Hydrothermal	N-Doping	0.5M $NaClO_4$	Ag/AgCl	1.0	0.017	0.4	(X. Yang et al., 2009)
ZnO nanowires	Hydrothermal	MWCNT hybridisation	0.1M Na_2SO_4	Ag/AgCl	0	0.05	0.4	(Liwu Zhang et al., 2009a)
ZnO nanorods	Ammonia-assisted hydrolysis	Surfactant mediated crystal growth	0.1M LiI 0.05M I_2 0.5M TBP	-	0	0.37	0.47	(Rahman et al., 2015)
ZnO nanowires	Hydrothermal + atomic layer deposition	TiO_2 heterojunction	0.1M KOH	Ag/AgCl	0.25	0.4	0.5	(Mingzhao Liu et al., 2013a)
ZnO nanosheets	Electrodeposition	Exposed polar facet	0.5M Na_2SO_4	Ag/AgCl	1	0.2	0.51	(Hsu et al., 2011)

ZnO nanotubes	Anodisation	Control of morphology	0.5M Na_2SO_4	SCE	0.25	0.25	0.52	(Faid and Allam, 2016)
ZnO nanorods	Chemical bath deposition + photodeposition	Cobalt phosphate co-catalyst	0.1M KH_2PO_4	SCE	0.5	0.36	0.54	(Jeon et al., 2011)
ZnO nanorods	Spin-coating	Cu-doping	0.1M NaOH	SCE	0	0.312	0.752	(V. Sharma et al., 2011)
Fe_3O_4-ZnO core-shell	Hydrothermal	Fe_3O_4 heterojunction+rGO hybridisation	0.1M KOH	RHE	1.23	0.52	0.85	(Yusoff et al., 2015)
ZnO nanotetrapods	Thermal evaporation + chemical bath deposition	Morphology + N-doping	0.5M Na_2SO_4	RHE	0.92	0.046	0.99	(Qiu et al., 2012)
ZnO triangles	Hydrothermal	Control of morphology + graphene oxide hybridisation	1.0M NaOH	RHE	1.23	0.321	1.29	(Chandrasekaran et al., 2016)
ZnO nanoparticles	Spin coating	Effect of annealing temperature	0.1M NaOH	SCE	0	0.105	1.321	(M. Gupta et al., 2009)
ZnO NAs/RGO/$ZnIn_2S_4$	Hydrothermal	Heterojunction + $ZnIn_2S_4$ photosensitiser	1.0M Na_2SO_4	Ag/AgCl	0.5	0.6	1.41	(Bai et al., 2015)
ZnO nanopencil arrays	Hydrothermal + photoreduction	Au photosensitiser	0.5M Na_2SO_4	Ag/AgCl	1	0.7	1.5	(T. Wang et al., 2015a)
ZnO nanorod	Electrodeposition	rGO hybridisation	0.1M KOH	Ag/AgCl	1	1	1.8	(Hamid et al., 2016)
ZnO nanowires	Hydrothermal + wet chemical impregnation	CdTe quantum dot photosensitiser	0.5M Na_2SO_4	Ag/AgCl	1	0.7	2	(Hao Ming Chen et al., 2010)
ZnO nanowires	Sol-gel spin coating + electrochemical deposition	Au co-catalyst	0.1M NaOH	SCE	0.5	1.5	2.6	(Kumari et al., 2015)
ZnO nanorods	Hydrothermal + ion exchange	$AgSbS_2$ co-catalyst	1.0M Na_2S	Ag/AgCl	+0.212 (Control) +0.096 (Modified)	0.41	5.08	(J. Han et al., 2015)
ZnO nanorod	Electrodeposition	Effect of applied potential	1.0M NaOH 1 wt. % ethylene glycol	SCE	1	5.74	12.94	(Abd Samad et al., 2016)

2.3 Strategies to enhance photocatalytic activity of carbon-promoted ZnO

Following the discovery of TiO_2 as a photocatalyst material, ZnO has since emerged as a leading candidate as photoelectrode material for PEC water-splitting. ZnO is a wide band gap (3.37 eV), n-type metal oxide material with direct band gap properties (Srikant and Clarke, 1998). Similar to TiO_2, the band gap is able to straddle both the H_2O reduction (arbitrarily assigned as 0.00 eV vs normal hydrogen electrode (NHE)) and OH^- oxidation reactions (-1.23 eV vs NHE) (Gratzel, 2001). ZnO possesses high electron mobility compared to TiO_2 due to the formation of a large band dispersion caused by the stabilisation of d^{10} orbitals and utilisation of Zn *s* and *p* orbitals in the CB (Hisatomi et al., 2014; Inoue, 2009). A high electron mobility corresponds with fast transport of photoexcited electrons across the bulk crystal (Jayah et al., 2015), hence more efficient charge separation and H_2 production efficiency. ZnO can be synthesised by applying a wide range of synthesis techniques (Baruah and Dutta, 2009; Lockett et al., 2012) to obtain a great variety of different morphologies and nanostructured electrodes (Gonzalez-Valls and Lira-Cantu, 2009; Skompska and Zarębska, 2014). The unique characteristics of ZnO has gained significant scientific interest for its photocatalytic properties, thus the design and development of ZnO nanostructure assemblies has become the subject of intense investigation as a promising PEC water-splitting photoelectrode material.

However, practical issues such as limited usage of the light spectrum, recombination and photocorrosion inhibit the widespread use of ZnO as photoelectrode material in PEC water-splitting systems (J. Yang et al., 2013). ZnO absorbs light in the UV region due to its band gap of approximately 3.37 eV (Janotti and Van de Walle, 2009). This means that photons with wavelength > 400 nm are largely unutilised by the ZnO thin film. To allow for optimum harvesting of solar light, the band gap needs to be close to

the peak of the energy range of the AM1.5 spectrum (1 eV to 3 eV). There is a broad agreement that an optimal photoelectrode material possesses band gap energy of approximately 2 eV, to account for the decomposition potential of 1.23 V, overpotential and ohmic drop losses (Alexander et al., 2008; Xiang et al., 2016). ZnO suffers from the drawback of high recombination rate of photogenerated electron-hole pairs, whereby -OH and -H bonds at the surface of the ZnO crystal were found to facilitate the recombination process (L. L. Yang et al., 2010). Efforts to facilitate the efficient separation of photogenerated electron-holes will, in effect, reduce its recombination rate (X. Zhang et al., 2014). Moreover, the well-known photocorrosion of ZnO often leads to a decrease in the photostability of ZnO under prolonged light irradiation (Rudd and Breslin, 2000; Sapkal et al., 2012). PEC water-splitting is commonly performed in alkaline conditions such as KOH and NaOH. When immersed in alkaline solutions, the ZnO surface is transformed to $Zn(OH)_2$ and the rate of transformation increases with increasing pH. $Zn(OH)_2$ will further dissolve into Zn^{2+} ions due to the presence of OH^- ions to reduce $Zn(OH)_2$.

Carbon-based promoters are a promising alternative to metal-based promoters for enhancing the electron-transfer properties of n-type semiconductor photoanodes. Metal-based promoters are able to enhance charge separation because possess of its high density of states in the CB. Alternatively, carbon-based promoters can enhance charge separation because the presence of delocalised sp^2 electrons and long diffusion lengths enable electron transport. The chemical stability of carbon-based promoters provide an additional incentive to develop novel structured carbon-based promoters.

Metal-free carbon-based materials offer various advantages compared to metal-based catalysts e.g. low cost, thermal and chemical stability, with the opportunity for facile control of porous structure and surface functionality (L. Liu et al., 2015). For instance,

the discovery of graphene's remarkable properties (Geim and Novoselov, 2007) quickly led to its widespread investigation as a promising, cost effective and environmentally-friendly photocatalyst promoter (Xin Li et al., 2016b). Carbon nanotubes, mesoporous carbons, graphitic carbon nitrides, activated carbon and hydrochar also offer interesting catalytic behaviour as the defects present on the surface and edges of the carbon materials may act as active sites for chemical reactions to occur (L. Liu et al., 2015).

It follows then, that carbon-ZnO hybridised nanomaterials would demonstrate improved photocatalytic activity compared to pristine ZnO; the incorporation of carbon-based promoters often acts as electron transfer agent and enhances charge separation. **Thus, an investigation on the effects of synthesis parameters on the photocatalytic activity of hybridised, carbon-promoted ZnO is crucial to identify optimized synthesis conditions for maximum photocatalytic activity.** The following sections summarise the consideration and efforts taken to increase the photocatalytic activity of ZnO through hybridisation with carbon-based promoters.

2.3.1 Control photocatalytic properties of ZnO

The fabrication of affordable ZnO thin films with high STH conversion efficiency is an active area of research. As with any other semiconductor material, the utilisation of ZnO as photoanode material depends on its cost of production and quality of the finished product. The conventional methods of producing ZnO i.e. the French Process, the American Process (also known as the Direct Process), co-precipitation from zinc hydrosulphite and thermal decomposition of zinc carbonate (Moezzi et al., 2012) are inadequate for the production of ZnO nanostructures. Nanowire structures are particularly favoured due to its high aspect ratio which can facilitate charge transport along metal oxide materials with nanometre resolution across micrometre-scale

distances (Warren et al., 2013). ZnO nanorods with higher aspect ratio have demonstrated significantly higher photocatalytic performances (X. Zhang et al., 2014). The increase of photocurrent as a function of length was also observed in TiO_2 nanowire arrays with a maximum photocurrent of 0.73 mA cm^{-2} at +1.5 V vs RHE in 1 M NaOH electrolyte solution (Hwang et al., 2012).

Therefore, innovative synthesis techniques are being developed to produce high quality, vertically-aligned nanowire/nanorod ZnO thin films. Based on the literature, two main approaches exist for the preparation of ZnO thin films. The first strategy is a two-step process involving the synthesis of ZnO nanoparticles followed by fixing them onto a solid conductive substrate. This preparation method allows for the precise control of ZnO nanostructures using simple synthesis methods but poor electrical contact between the ZnO nanoparticles and conductive substrate remain the major drawback of this approach. The second strategy involves the one-step, direct growth of ZnO nanoparticles onto a solid conductive substrate. This synthesis technique is preferred for its convenience and improved physical stability.

Direct growth methods to prepare vertically-aligned ZnO thin films include physical vapour deposition, chemical vapour deposition, chemical bath deposition, thermal evaporation, arc deposition, pulse laser deposition, sputtering, sol-gel spin-coating and electrochemical deposition (R. Kumar et al., 2015b; Natsume and Sakata, 2000; Znaidi, 2010). Among the available methods to prepare ZnO thin films, electrochemical deposition stands out as a cost effective, rapid and convenient method to produce high quality ZnO thin films (Dharmadasa and Haigh, 2006).

Electrochemical deposition is a process by which a thin and tightly adherent desired coating of metal, oxide, or salt can be deposited onto the surface of a conductor substrate by simple electrolysis of a solution containing the desired metal ion or its

chemical complex (Rodriguez and Tremiliosi-Filho, 2013). The three-electrode electrochemical cell setup is most commonly used to perform electrochemical deposition. The electrode to be coated is the cathode of the circuit (working electrode) whereas an inert counter electrode such as Pt is used to complete the circuit. The working and counter electrodes are immersed in an electrolyte comprising an aqueous salt solution and oxygen precursor (Sanchez et al., 2012). Zinc(II) nitrate, $Zn(NO_3)_2$, zinc(II) acetate, $Zn(COOCH_3)_2$, and zinc(II) chloride, $ZnCl_2$ are the commonly used zinc salt precursors. Molecular oxygen is conventionally used as oxygen precursor, however, hydrogen peroxide or nitrates can also be used. An electric potential is applied between the working and counter electrode to drive the electrochemical deposition reaction, thus forming the desired coating on the surface of the working electrode. The chemical reactions in a typical cathodic electrodeposition of ZnO from $Zn(NO_3)_2$ was proposed as follows (Illy et al., 2011):

$$NO_3^- + H_2O + 2e^- \rightarrow NO_2^- + 2OH^- \qquad \text{(Eq. 2.2)}$$

$$\underline{Zn^{2+} + 2OH^- \rightarrow Zn(OH)_2 + H_2O} \qquad \text{(Eq. 2.3)}$$

Overall equation: $Zn^{2+} + NO_3^- + 2e^- \rightarrow Zn(OH)_2 + NO_2^-$ (Eq. 2.4)

$Zn(OH)_2$ undergoes further decomposition to ZnO:

$$Zn(OH)_2 \rightarrow ZnO \qquad \text{(Eq. 2.5)}$$

The as-prepared electrodeposited thin film consists of a polycrystalline mixture of $Zn(OH)_2$ and ZnO, as a result of incomplete conversion of $Zn(OH)_2$ to ZnO during electrochemical deposition (Khajavi et al., 2012). Thus, an annealing step is often required following the electrodeposition step in order to increase the crystallinity and grain size of the ZnO nanorods.

The electrochemical deposition method is able to provide fine control over the properties of the ZnO thin film product, yet maintaining cost effectiveness by conducting the process at atmospheric conditions and mild temperatures. The optimisation of electrode potential, electrolyte concentration, and temperature are able to offer precise and direct control over the electrochemical deposition of vertically-aligned ZnO nanorod arrays.

The photocurrent density of ZnO thin films was found to be directly related to the annealing temperature and atmosphere of annealing. As demonstrated in a previous experiment involving ZnO thin films prepared by sol-gel spin coating method, the as-prepared thin films were subjected to increasing annealing temperatures of 400, 500 and 600 °C to investigate the effect of temperature on the photocurrent response of the thin films. The photocurrent density (PCD) was measured at an applied bias of +0.5 V vs Ag/AgCl in 0.1 M NaOH electrolyte solution. The sample annealed at 400 °C produced PCD of 0.2 mA cm^{-2} whereas the PCD increased to 1.6 mA cm^{-2} when the ZnO thin film was sintered at 600 °C (M. Gupta et al., 2009). The enhanced photocurrent was attributed to the decrease in electrical resistivity as a result of increasing sintering temperature, from 15.6 kΩ cm (400 °C) reduced to 9.3 kΩ cm when annealed at 600 °C. The annealing atmosphere plays an important role on the physicochemical characteristics of the resulting nanostructures. In an experiment comparing the surface properties of ZnO thin films annealed under air and nitrogen atmosphere, XPS analysis showed that samples annealed under nitrogen atmosphere resulted in a high V_O concentration compared to the sample annealed in air (Hernández et al., 2014).

The photocatalytic properties of ZnO has been attributed to the presence of oxygen defects at the surface (T.-T. Chen et al., 2013a). A previous study reporting the synthesis of graphene-hybridised ZnO triangles attributed its increased output

photocurrent density of 1.26 mA cm^{-2} (compared to 0.321 mA cm^{-2}) to an increase of oxygen defects in the ZnO triangle nanostructure (Chandrasekaran et al., 2016). Other studies have indicated that the presence of V_o narrows the band gap of ZnO (Ansari et al., 2013; Junpeng Wang et al., 2012b), leading to reduced overpotential for photoexcitation of electrons. Thus, the light absorption properties of ZnO can be tuned to the visible spectral region by controlling the intrinsic defect states (Kavitha et al., 2015): more V_o at the photoanode surface increases the photocurrent.

2.3.2 Control properties of carbon-based promoters

2.3.2.1 Graphene

Graphene is an allotrope of carbon, consisting of a single sheet of sp^2 hybridised carbon atoms interconnected in a hexagonal lattice. The ability to tune the properties of graphene between a semiconductor and semimetal makes this material such an attractive subject of investigation as a non-metal promoter for electro- and photocatalytic applications.

The unique band structure and sp^2–hybridised structure of pristine graphene allows the material to display high conductivity and electron mobility, making it a good electron transfer agent and co-catalyst. A similar sp^2-hybridised nanostructured carbon, i.e. multi-walled carbon nanotubes (MWCNTs) were composited with zinc oxide nanowires on a p-GaN layer which demonstrated good activity for ultraviolet photodetector (Shao et al., 2013). The good performance of this heterojunction photodetector is attributed to improved carrier transport and collection efficiency through the MWCNTs network deposited on top of the ZnO nanowires. The co-catalyst is typically a noble metal or metal oxide or a combination of them, loaded onto the surface of photocatalyst to suppress recombination, enhance charge separation, increase

the number of reactive sites and reduce activation energy for gas evolution. High quality, pristine graphene possesses a high work function of 4.89-5.16 eV (Song et al., 2012; X. Wang et al., 2008), which allows it to behave as a semimetal.

On the other hand, when graphene is tuned to behave like a semiconductor, it was proposed that it could exhibit photocatalytic or photosensitiser properties (Xie et al., 2013). One study studied the role that rGO played to enhance the photocatalytic abilities of TiO_2 (Minella et al., 2017). Their research suggested that charge separation in rGO-TiO_2 hybrids occur via electron transfer from rGO to TiO_2, and transfer of holes from TiO_2 to rGO. The authors also reported that rGO enhanced the photocatalytic activity of TiO_2 by significantly supporting dye adsorption and electron transfer processes rather than as a visible sensitiser.

Combining semiconductors with graphene also has the potential to avoid photocorrosion because the electron acceptor and transporter role of graphene is beneficial for extracting the photoinduced charge from semiconductors rapidly (Zhang Chen et al., 2013c; Fu et al., 2008; Yanhui Zhang et al., 2013c).

The electrochemical reduction of graphene oxide (GO) to reduced graphene oxide (rGO) is a straightforward, economic, and fast technique to restore the delocalised π-network and produce graphene-like compounds with improved electrical conductivity on the large scale. Compared to thermal, chemical or photo-reduction methods, the electrochemical reduction of GO does not involve high temperature, hazardous reducing agents or photoactive chemicals to remove the oxygen functional groups (Toh et al., 2014). For instance, chemical exfoliation of graphite is currently the most effective, top-down method of preparing graphene (S. Wu and Zhang, 2014; Zhao et al., 2012). The major drawback of producing graphene using the Hummers, Staudenmaier and/or Hofmann's method is the use of harsh chemical conditions (concentrated acid at

elevated temperatures) in the preparation process (Moo et al., 2014; Poh et al., 2012). Bottom-up approaches also exist such as chemical vapour deposition (CVD), whereby volatile carbon precursors, e.g. ethene are deposited on a substrate surface under high temperature conditions – making it an energy-intensive process (Addou et al., 2012; Batzill, 2012; Xuesong Li et al., 2016a). Additionally, the options for carbon precursor are limited to volatile carbon precursors, ideally at room temperature.

The electrochemical reduction (deoxygenation) of GO can be accomplished using a one-step or two-step method. In the one-step electrochemical approach, an applied potential is applied directly into an aqueous colloidal suspension in the presence of an electrolyte solution, producing a thin film of electrochemically-reduced GO on the surface of the working electrode. The electrical potential may be applied via cyclic voltammetry (CV) (S. Li et al., 2017), linear sweep voltammetry (LSV) (Ping et al., 2011) or at a constant potential (Dong et al., 2016; Toh et al., 2016), in a standard three-electrode electrochemical system at room temperature. In the two-step electrochemical approach, an electric potential is applied to a thin film of GO pre-deposited onto the surface of an electrode (Toh et al., 2014).

2.3.2.2 HTC-biocarbon

The development of sustainable techniques to prepare nanostructured carbon promoters for PEC water-splitting from renewable carbon precursors is an attractive approach to reduce the environmental impact of synthesis. Graphene and GO are being developed using chemical vapour deposition (CVD) and HTC routes, respectively, as a means of avoiding harsh chemical methods to prepare graphene from graphite. In the CVD method, biomass is being investigated as an alternative, renewable carbon source for ethylene gas, which is commonly employed as a gaseous carbon precursor in the

CVD process (Yi Zhang et al., 2013d). The synthesis of GO involves bottom-up growth from saccharide precursors such as glucose or sucrose (Tang et al., 2012). Alternatively, HTC-biocarbon, also known as hydrochar, may be produced via the HTC of renewable precursors such as cellulose. The HTC-biocarbon product is essentially a disordered carbon, possessing sp^2 and sp^3 moieties due to the uncontrolled repolymerisation of basic structural units formed in the depolymerisation phase. The functional groups and defects present on the carbon surface contribute to its catalytic properties for reaction such as methane dehydrogenation (Serrano et al., 2010; Shen and Lua, 2016).

The HTC of renewable carbon precursors, e.g. glucose, cellulose and lignocellulosic biomass has gained significant attention in recent years (Titirici et al., 2007) due to its potential for CO_2 sequestration (Sevilla et al., 2011), as well as its green approach to produce hydrochar (low processing temperature, non-toxic solvent, renewable carbon precursor). The sustainable HTC system uses renewable lignocellulosic bio-resources and requires a relatively mild temperature to produce carbon nanomaterials with specific functionalities (Libra et al., 2011). The use of heated, pressurized H_2O as solvent allows carbonisation reactions to proceed at mild temperature conditions ranging from 180 to 250 °C (Titirici and Antonietti, 2010). The HTC process is a promising route to synthesise functional biocarbon with the desirable functional group (aldehyde, hydroxyl, carbonyl, carboxylic, *etc*.) for specific applications such as electrodes, supercapacitors, and gas storage media.

The properties of hydrochar obtained from biomass (eucalyptus sawdust) 80 g sawdust in 50 mL distilled H_2O, 250 °C, 4 °C min^{-1}, 2 h include: (1) Brown colour, (2) 50-60 % carbon, (3) Contains a high degree of aromatics, (4) Contains large amount of oxygen-containing groups (carbonyl, carboxylic, hydroxyl, quinone ester etc.) – hydrophilic properties. (5) Small surface area and low porosity (4 m^2 g^{-1}), (6) High

concentration of oxygen at the surface of the particle (based on XPS analysis). HTC-biocarbon obtained from the HTC of glucose, starch and sucrose (Sevilla and Fuertes, 2009a) possessed the following properties: (1) BET surface area less than 3 m^2 g^{-1}, (2) The increase in temperature was reported to increase the product yield, (3) FTIR analysis suggested that dehydration and aromatisation reactions took place, evidenced by the reduction of peak intensity from hydroxyl and carboxyl groups (3000–3700 and 1000–1450 cm^{-1}) in the hydrochars, compared to its corresponding saccharide.

Previous work on the synthesis of hydrochar from lignocellulosic and polysaccharidic carbon sources by Sevilla (Sevilla and Fuertes, 2009a) and Funke (Funke and Ziegler, 2010) have led to the proposal of a mechanism of hydrochar formation, which may be summarised as follows: (1) the hydrolysis of complex polysaccharides to monosaccharides, (2) dehydration, fragmentation and decarboxylation to form reactive monomers and (3) tandem repolymerisation and aromatisation reactions (4) burst nucleation and growth of hydrochar particles. A brief description for each process is described below.

The hydrolysis of polysaccharides yields the corresponding monosaccharides (i.e. starch from glucose, and glucose and fructose from the hydrolysis of sucrose). In the hydrolysis step, the disaccharides (e.g. sucrose) and polysaccharides (e.g. starch) undergo cleavage of ester and ether bonds in biomacromolecules (Negahdar et al., 2016). Dehydration is the process whereby hydroxyl groups in the biopolymer structure are eliminated as H_2O molecules. For instance, glucose undergoes dehydration to 1,6-anhydroglucose. Thus, monosaccharides produced from the hydrolysis reaction undergo dehydration and fragmentation processes (i.e., ring-opening and C-C bond breaking) processes to yield soluble organic molecules such as furfural-like compounds (e.g. 5-hydroxymethylfurfural, furfural, 5-methylfurfural), acids (e.g., acetic, lactic, propenoic,

levulinic and formic acid) and aldehydes (e.g. acetaldehyde, acetonylacetone) (Vasudevan and Mushrif, 2015). The reactive, unsaturated organic molecules produced from the hydrolysis, dehydration and fragmentation reactions subsequently react with each other via polymerisation or condensation reactions. The polymerisation reactions were proposed to be induced by intermolecular dehydration or aldol condensation. It was suggested that HTC is mainly characterized by condensation polymerisation, specifically aldol condensation (Elaigwu and Greenway, 2016). At the same time, the aromatisation of the polymers takes place. The aromatisation of the polymers also occurs simultaneously with the formation of C=C linkages, which was previously attributed to keto-enol tautomerism of the dehydrated species or intermolecular dehydration of the aromatized molecules formed during the decomposition or dehydration of the glucose (Sevilla and Fuertes, 2009a; Sevilla and Fuertes, 2009b).

The growth mechanism of HTC-biocarbon particles was proposed to take place following the La Mer model (Sevilla and Fuertes, 2009a; Q. Wu et al., 2015). As the reaction progresses, the concentration of aromatic clusters increase and reaches a critical supersaturation point, upon which burst nucleation occurs and hydrochar nuclei are formed. The formed nuclei then grow into hydrochar particles through diffusion to the surface of the chemical species that are present in solution, according to the surface properties of the nuclei and to minimize the energy of the interfaces (Guiotoku et al., 2009). Once the growth process is stopped, the superficial functionalities of the hydrochar microspheres were observed to consist of reactive oxygen groups. At the end of the reaction, two types of products were found in the reaction medium: 1) an insoluble residue consisting of carbonaceous spherical micro-particles with a core–shell chemical structure (hydrochar microspheres), and 2) aqueous soluble organic compounds (i.e., furfural-like compounds, acid, and aldehydes). As the concentration of the aqueous saccharide solution, the reaction temperature, or the reaction time rise, the

processes of aromatisation and polymerisation will be favoured and, in consequence, the diameter of the microspheres and the HTC-biocarbon yield increases.

The advantage of using HTC to produce nanostructured carbon is its high product yield – this is due to the suppression of the decarboxylation reaction that is dominant in the pyrolysis process. H_2O helps to suppress pyrolysis by acting as a good heat transfer and storage medium that avoids local temperature peaks that might result from exothermal reactions. Hot H_2O has been recognized as a reactant, solvent and catalyst for facilitating hydrolysis, ionic condensation and cleavage. Free radical polymerisation is also suppressed due to the aqueous conditions which favour ion chemistry (Funke and Ziegler, 2010), i.e. H^+ ions saturate organic compounds and suppress radical polymerisation. This enhances bond cleavage of H_2 bonds primarily in hydrolysis reaction.

Nevertheless, the disordered structure in HTC-biocarbon results in the material to be a poor conductor, which limits the use of HTC-biocarbon as catalyst support in non-electrochemical applications. In order for HTC-biocarbon to be applied as electrocatalytic applications, a significant amount of sp^2 moiety needs to be incorporated into the HTC-biocarbon structure. Therefore, efforts to increase the diffusion distance and sp^2 functionality in HTC-biocarbon to mimic structures like glassy carbon may be beneficial to increase its electrical conductivity.

2.3.3 Improve heterogeneous interface between ZnO and carbon-based promoter

Hybridising ZnO with nanostructured carbon such as graphene and carbon nanotubes have been proposed as an effective strategy for suppressing recombination and

photocorrosion. There is a substantial number of research articles on the synthesis of rGO/ZnO nanocomposites for photocatalytic degradation applications (Zhang Chen et al., 2013c; Feng et al., 2014; Jo and Clament Sagaya Selvam, 2015; J.-X. Sun et al., 2012; Jinfeng Wang et al., 2012a). However, studies investigating the enhancement of PEC water-splitting by nanostructured carbon are greatly lacking. For this reason, the exploration of NC-ZnO composites will be able to provide greater insight into the mode of enhancement. Compared to other modes of modification, hybridisation with nanostructured carbon was able to tune the properties of the ZnO photoanode by means of tuning the properties of the nanostructured carbon, opening up a wide range of possibilities for specific design of photocatalysts.

Among the limited literature available on the specific application of NC-ZnO hybrids as PEC water-splitting material, four approaches to prepare NC-ZnO hybrids can be identified, i.e. (1) synthesis of nanocomposites (nanostructured carbon-hybridised ZnO nanoparticles), followed by thin film deposition (2-step approach), (2) growth of ZnO on nanostructured-carbon coated electrode (2 step-approach), (3) simultaneous deposition of nanostructured carbon and ZnO (1-step approach), and (4) coating ZnO with nanostructured carbon. Each method is summarised in Table 2.2.

The first strategy involves the synthesis of NC-ZnO hybrid nanomaterials and then fixing it onto a solid conductive substrate. In one study, graphene-ZnO quasi shell-core composite materials were prepared by solvothermal method, using ZnO grown from zinc acetate dissolved in dimethylformamide (DMF) solution for 5 hours at 95 °C (Bu et al., 2013). The nanomaterials were then dispersed in acetone and doctor bladed on to fluorine-doped tin oxide (FTO) glass. The J_{SC} of this photoanode was measured at 0.0 V bias potential in a 0.1 M Na_2SO_4 solution. Beginning with an observed J_{SC} of approximately 0.45 mA cm^{-2}, the J_{SC} dropped to 0.20 mA cm^{-2} within three cycles of

on-off switching. The authors attributed the decrease in J_{SC} to the photocorrosion of ZnO. Since the graphene-ZnO nanoparticles were adhered on to the FTO glass surface using physisorption method, it is also very likely that the graphene-ZnO photoanode suffered physical stability issues which resulted in reduced J_{SC}.

The second strategy involves the growth of ZnO on NC-coated solid substrate. This type of composite was achieved in one study by electrochemical deposition of rGO on the surface of ITO glass, followed by a second electrochemical deposition step to grow ZnO nanocrystals on the rGO-coated surface (Upadhyay et al., 2014). The photoanode yielded a PCD of 0.54 mA cm^{-2} at +0.8 V vs Ag/AgCl in an electrolyte solution of 0.1 M NaOH. In another study, ZnO nanowires were grown on multi-walled carbon nanotubes (MWCNTs) arrays using a hydrothermal process (W.-D. Zhang et al., 2009c). The authors reported PCD values of 0.42 and 0.10 mA cm^{-2} for these photoanodes when illuminated with UV and sunlight irradiation, respectively. The light response of the photoanode was stable, as indicated by the consistent PCD observed after repeated on-off switching of light. This indicated that the formation of chemical bonding between MWCNTs (or any other NCs) and ZnO allows for improved stability of the photoanode.

A third approach to prepare NC-ZnO hybrid photoanodes featured the simultaneous deposition of NC and ZnO onto the solid substrate. GO/ZnO triangles were previously prepared on copper foil as conductive substrate, using a sonochemical method to simultaneously reduce GO and stimulate the growth of ZnO from zinc(II) acetate solution (Chandrasekaran et al., 2016). Based on linear sweep voltammetry (LSV) analysis, the authors reported a PCD of 1.29 mA cm^{-2} at +1.23 V vs reversible hydrogen electrode (RHE) as well as IPCE of 10.41 % at 360 nm.

A final strategy to incorporate ZnO with nanostructured carbon is to coat a thin film of NC onto a pre-grown ZnO thin film. MWCNTs, rGO and graphene quantum dots have been coated on ZnO thin films using hydrothermal (Y. Wei et al., 2014), electrophoresis (Y.-G. Lin et al., 2012), dip-coating (Bai et al., 2015) and covalent immobilisation methods (Guo et al., 2013). The authors attribute the enhancement of ZnO photoresponse as a result of the NCs participating either as charge transfer agent or photosensitiser.

Table 2.2 Preparation of NC-ZnO photoanodes with specific application towards PEC water-splitting

No.	Material	Preparation method	Mode of enhancement (method)	Efficiency parameter	Electrolyte	Maximum output	Reference
Strategy #1: preparation of NC-ZnO nanoparticles + physical deposition							
1	Graphene–ZnO Quasi-Shell–Core Composite	Solvothermal	Morphology + heterojunction	- PCD	0.1M Na_2SO_4		(Bu et al., 2013)
Strategy #2: growth of ZnO on NC-coated electrode							
1	rGO-Ag/ZnO	Electrodeposition	Doping + heterojunction	- PCD	1M NaOH	- 2.48 mA cm^{-2} at 0.8 V	(Upadhyay et al., 2014)
2	MWCNT/ZnO	CVD+ hydrothermal	Heterojunction, promote electron transfer	- PCD	0.1M Na_2SO_4	- 0.87 mA cm^{-2} (1 V) - 0.15 mA cm-2 (0 V)	(W.-D. Zhang et al., 2009c)
Strategy #3: Simultaneous deposition of NC and ZnO							
1	GO/ZnO triangles	Solution processing	Morphology + surface modifications	- PCD - IPCE	1M NaOH	- 1.29 mA/cm^{-2} at +1.23 V - 10.41% at 360 nm	(Chandrasekaran et al., 2016)
Strategy #4: coating ZnO with NC							
1	CNT-ZnO	Hydrothermal	Charge carrier transfer	- PCE		- 0.646	(Y. Wei et al., 2014)
2	rGO/ZnO	Electrophoresis	Photosensitiser	- Photocurrent response - IPCE	0.1M Na_2SO_4	- 0.35 mA cm^{-2} - 80% at 350 nm	(Y.-G. Lin et al., 2012)
3	ZnO/rGO	Hydrothermal + dip-coating	heterojunction	- PCD	1.0M Na_2SO_4	0.8 mA cm^{-2} (at +0.5 V vs Ag/AgCl)	(Bai et al., 2015)
4	ZnO/graphene QD	Hydrothermal + covalent immobilisation	Photosensitiser	- IPCE - H_2 production rate	0.5M Na_2SO_4	- 4 % at +0.8 V vs Ag/AgCl - 2.4 µmol h^{-1} at +0.8 V vs Ag/AgCl	(Guo et al., 2013)

2.4 Research opportunities

Although cheaper than noble metals, the production of graphene incurs a substantial environmental cost. Therefore, graphene must be used in an optimal amount and configuration so as not to waste resources. The optimal usage of graphene is a field of research that remains to be further explored. So far, the proposed strategies for harnessing the structure and electronic conductivity of graphene are *via* strengthening the interfacial contact, optimizing the electronic conductivity of graphene, and spatially optimizing the interfacial charge carrier transfer efficiency (M.-Q. Yang et al., 2014). While it is generally acknowledged that the properties of rGO vary widely according to the individual parameters in the thermal-, chemical-, and photo-reduction technique (e.g. chemical identity of the reducing agent, time, temperature, property of GO), to the best of the author's knowledge, no comparison has been made on the effect of electrochemical reduction techniques on the properties of rGO.

Secondly, efforts to modify the properties of HTC-biocarbon to mimic glassy carbon will enhance its potential application as promoter for PEC water-splitting. HTC-biocarbon shows interesting catalytic activity but its poor electroconductivity limits its application in PEC water-splitting. The properties of HTC-biocarbon may be enhanced by increasing sp^2 content using Lewis acids such as metal salts, *e.g.* $ZnCl_2$ (Fechler et al., 2013), copper(II) acetate, $Cu(CH_3COO)_2$ (S.-H. Yu et al., 2004), and ammonium iron(II) sulphate $[Fe(NH_4)_2(SO_4)_2]\cdot 6H_2O$ (Cui et al., 2006). Metal salts have been considered as an alternative to mineral acids due to the greater ease in recovery of the metal salts, making the catalysed carbonisation process more environmentally friendly. Alternatively, the diffusion distance of HTC-biocarbon may be increased by adding a soft template such as PVA to form a carbon-carbon hybrid structure.

As such, the present thesis sought to investigate the optimal conditions for preparing electrochemically-reduced GO for the synthesis of rGO-hybridised ZnO photoanodes. Also, HTC-biocarbons were produced using $ZnCl_2$/NaCl and PVA in the HTC of renewable carbon precursors for the purpose of modifying the sp^2 content and morphology of the HTC-biocarbon product, respectively.

CHAPTER 3: SYNTHESIS AND CHARACTERISATION OF HTC-BIOCARBON

3.1 Introduction

Carbon-based PEC water-splitting promoters offer an economic pathway to improve charge transfer and photostability of PEC water-splitting photocatalyst materials. For instance, g-C_3N_4, carbon nanotubes, rGO and activated carbon have demonstrated enhancement of photocatalytic activity of various semiconductors, e.g. ZnO and TiO_2 (K. Li et al., 2015a; Y. Li et al., 2015b; Liwu Zhang et al., 2009a; Long Zhang et al., 2013b; W.-D. Zhang et al., 2009c). The enhancement of photocatalytic activity was attributed to the ability of the carbon-based promoter to improve the semiconductor's charge transfer properties (Nagaraju et al., 2015) and resistance against photocorrosion (Tong et al., 2014; Zhonghai Zhang et al., 2013e).

The development of methods to prepare active and efficient organic (carbon-based) PEC water-splitting promoters is an active field of research with the goal of increasing the efficiency and durability of PEC water-splitting electrodes, while increasing the ROI in the technology used to prepare the carbon-based promoters. High-temperature preparation techniques such as arc discharge or laser ablation were first used to produce CNTs but have been replaced by low temperature chemical vapour deposition (CVD) techniques, all of which require supporting gases and vacuum (Prasek et al., 2011). g-C_3N_4 was traditionally synthesised by thermal condensation of N-rich precursors, such as urea, dicyandiamide, melamine, but has since developed to include alternative techniques such as supramolecular pre-assembly, rapid microwave-assisted production, molten salt strategy, and ionic liquid strategy (Ye et al., 2015). rGO is commonly prepared on a large scale by the chemical reduction of GO, which involves the chemical-intensive exfoliation process of graphite to GO (either *via* Staudenmaier or

Hummer's method), followed by a chemical reduction process using hydrazine, N_2H_4, sodium borohydride, $NaBH_4$, or sodium hydrosulfite, $Na_2O_4S_2$ (Y. Zhu et al., 2010). Electrochemically active, nitrogen-enriched nanostructured carbon was also prepared through the pyrolysis of polyacrylonitrile (PAN) (Zhong et al., 2012). Alternatively, the HTC process offers an economic and sustainable synthesis alternative for the formation of nanostructured carbon for potential application as PEC water-splitting promoters.

The HTC process converts organic precursors to a carbon-rich product by applying moderate temperatures and pressures over an aqueous solution of lignocellulosic biomass for several hours (Hao et al., 2013; Ryu et al., 2010). The product, referred to as HTC-biocarbon in this thesis, is an amorphous and highly-functionalised nanostructured carbon material. Amorphous carbon has high thermal and chemical stability, as well as nontoxic properties (Sha et al., 2016).

However, one technical barrier to the implementation of HTC-biocarbon as PEC water-splitting promoter is its limited conductive properties: the HTC-biocarbon, similar to activated carbon, exhibits capacitive behaviour. Previous studies have indicated that the charge transfer of activated carbon can be increased by increasing the sp^2 content within the activated carbon structure. Using similar reasoning, the suitability of HTC-biocarbon as PEC water-splitting is expected to increase as a result of enhancing the sp^2 content within the HTC-biocarbon, thereby increasing the conductivity and active sites available in the HTC-biocarbon material.

To the best of our knowledge, the literature relating to enhancing the preparation of HTC-biocarbon is largely limited to the use of mineral acids and metal salts as catalysts, and investigation of HTC-biocarbon prepared from a variety of renewable carbon sources. HTC is accelerated in the presence of mineral acids as the dehydration process is favoured in acidic conditions. Recently, Yu and co-workers have reported that HTC

of starch can be effectively accelerated by the presence of metal ions which also directs the synthesis towards various metal–carbon nanoarchitectures, such as Ag@carbon nanocables (S.-H. Yu et al., 2004) and Ag@carbon-rich composite micro-cables (L.-B. Luo et al., 2006). In addition, the presence of $[Fe(NH_4)_2(SO_4)_2]$ can effectively catalyse the carbonisation of raw rice grains in the HTC process (Cui et al., 2006). A variety of renewable carbon precursors were used to prepare HTC-biocarbons, e.g. starch (Cui et al., 2006), cellulose (Sevilla and Fuertes, 2009b), lignocellulosic biomass (B. Hu et al., 2010a; Jamari and Howse, 2012; Kang et al., 2012; Libra et al., 2011; Xiao et al., 2012; Lei Zhang et al., 2015b).

In view of the past studies preparing nanostructured carbon from renewable carbon precursors, the use of activating agents and soft templates have been applied in the preparation of nanostructured carbon *via* pyrolysis, but has not been widely applied in the HTC process. Chemical activation using agents such as KOH, $ZnCl_2$ and H_3PO_4 were found to produce activated carbon with increased surface area and adsorptive properties (Baquero et al., 2003). $ZnCl_2$ was found to enhance the yield and surface area of the activated carbon products by inhibiting the formation of tar, which blocks the pores formed during the activation process (Kalderis et al., 2008). A simple approach for fabrication of interconnected graphitized macroporous carbon foam with uniform mesopore walls by using hydrothermal method (Karthik et al., 2015).

Therefore, an opportunity presents itself for the modification of the HTC process using activating agent and soft template. This study aims to investigate the physical and chemical properties of HTC-biocarbon prepared using the modified HTC process in order to enhance the properties of HTC-biocarbon for potential application as PEC water-splitting promoter material. The objectives of this section were as follows:

1. To investigate the effect of activating agent on the physical and chemical properties of HTC-biocarbon obtained from carbon precursors with increasing complexity.
2. To investigate the effect of soft template on the physical and chemical properties of HTC-biocarbon

3.2 Materials and methods

To test the influence of activating agent and soft template on the physical and chemical properties of HTC-biocarbon, $ZnCl_2$ and polyvinyl alcohol (PVA) were selected as activating agent and soft template, respectively. Metal salts such as zinc chloride, $ZnCl_2$ have been used as an activating agent for the creation of porosity in activated carbons (Q. Li et al., 2012). Porosity in activated carbons were previously attributed to the role of $ZnCl_2$ in the gasification of the carbon precursor to CO_2 (Caturla et al., 1991). $ZnCl_2$ also possesses chemical properties of a Lewis acid, which have been found to accelerate the hydrolysis of cellulosic materials by attacking the glycosidic bond (Zehui Zhang and Zhao, 2010). PVA is a commercial H_2O-soluble, polymeric material that is the precursor to the formation of porous, 3D network through the formation of foams. PVA serves a dual purpose in this study, i.e. as soft structural template and carbon precursor. A soft template was chosen in order to simplify the post-treatment processing requirement, e.g. to eliminate the need for an acid wash step to remove catalysts after HTC treatment.

The experiments in this chapter investigated the effects of temperature, time, and additive:precursor mass ratio on the morphology and surface functionality of the final HTC-biocarbon products. The experiment involving $ZnCl_2$/NaCl as activating agent compared the effect of the precursor materials' structural complexity on the physical

and chemical properties of the HTC-biocarbon product. The second experiment in this chapter examined the effect of $FeCl_2$ catalyst on the properties of HTC-biocarbon prepared from PVA+cellulose foams.

$ZnCl_2$, NaCl, ethanol and HCl were purchased from R&M Chemicals (Malaysia). Glucose was obtained from Alfa Aesar (USA). Oil palm shell fibre (OPSF) was obtained from a local palm estate, and was washed with 10% nitric acid, HNO_3 and dried at 100 °C overnight, to remove organic impurities such as wax, sand and mud which may be present on the surface of the fibres (Moshiul Alam et al., 2012). The fibres were then ground to a fine powder and used in this state. PVA, sodium dodecyl sulfate (SDS), α-cellulose and boric acid were purchased from Merck (USA).

3.2.1 $ZnCl_2$/NaCl-activated HTC of glucose and oil palm shell fibre (OPSF)

The preparation of HTC-biocarbon using $ZnCl_2$/NaCl as activating agent was carried out following modifications to a previously published method (Fechler et al., 2013). In the present experiment, OPSF was selected as the lignocellulosic renewable carbon precursor whereas glucose was included in this study for comparison, as a model compound of cellulose.

Following the procedure reported by (Fechler et al., 2013), 6 g of OPSF was mixed with a $ZnCl_2$/NaCl slurry prepared by dissolving 10.2 g $ZnCl_2$ and 3.2 g NaCl in 3 mL H_2O. A eutectic salt mixture of 58 mol% $ZnCl_2$ and 42 mol% NaCl was selected to minimize the risk of potential crystallisation under cooling, which would potentially destroy the as-formed carbon structure. This mixture was sealed in a Teflon-lined 80 mL autoclave reaction vessel and subjected to hydrothermal conditions for 12 hours, at temperatures of 180 or 220 °C. The resultant solid samples were washed with 10%

hydrochloric acid solution, ethanol and deionized H_2O to remove H_2O-soluble organic molecules and the $ZnCl_2$/NaCl catalyst mixture. The above procedure was repeated using glucose in the place of OPSF. Blank samples were prepared by adding 6 g of precursor with 3 mL H_2O, and no catalyst was added. The samples prepared in this experiment are summarised in Table 3.1.

Table 3.1 Reaction conditions for the preparation of HTC-biocarbons using salt-templated HTC

Sample name	Precursor	$M_{precursor}$ (g)	$M_{ZnCl2/NaCl}$ (g)	Temperature (°C)	Reaction time (hours)
G1	Glucose	6	0.0	220	12
G2	Glucose	6	13.4	180	12
G3	Glucose	6	13.4	220	12
B1	Biomass	6	0.0	220	12
B2	Biomass	6	13.4	180	12
B3	Biomass	6	13.4	220	12

3.2.2 PVA-templated HTC of cellulose

A PVA+cellulose foam was prepared following a patented method (Rosenblatt, 1996). 4 wt. % PVA solution was prepared by dissolving 1 g PVA per 25 mL deionized H_2O, with heating and stirring. The following compounds were added to 25 mL of the PVA solution in succession: 0.5 g sodium dodecyl sulfate (SDS), 3 g cellulose, 5 mL formaldehyde solution, 4.5 mL 2 M boric acid solution. 2 g of $FeCl_2$ was incorporated into the PVA+cellulose mixture for the purpose of catalyzing the graphitisation process. Air was incorporated into the mixture using a mechanical stirrer for 10 minutes, to form a foam. This foam was poured into autoclave vessels and sealed before being subjected to a 2-step heat treatment. The PVA+celullose mixture was kept at 50 °C for 4 hours for the crosslinking step, forming a stable PVA+cellulose foam. Then the temperature was increased to 220 °C for 6 hours for the HTC process. The heating rate was 1 °C min^{-1}. After HTC, the samples were dried at 200 °C under atmospheric conditions for 6 hours.

The oxygen-containing functional groups were reduced by annealing the samples at 800 °C for 2 hours with heating rate of 2 °C min^{-1}, under N_2 gas flow.

3.2.3 Materials characterisation

Several characterisation techniques were used to identify the resulting carbon products *via* $ZnCl_2$/NaCl-activated and PVA-templated methods The morphology of the samples were investigated using a SUPRA^{TM} 35 VP Field Emission Scanning Electron Microscope (Carl Zeiss, Germany) and transmission electron microscopy (TEM) using a HT7701 3D Tomography Transmission Electron Microscope 120kV with Energy Dispersive X-Ray Spectrometer (Hitachi, Japan). The presence of functional groups in the final samples was investigated using Fourier transform infrared spectroscopy (Bruker IFS 66V/S, USA) and Raman spectroscopy (Renishaw in*Via* Raman microscope, UK), with ranges of 400 to 4000 cm^{-1} and 200 to 3200 cm^{-1}, respectively. The structure of the HTC-biocarbons was investigated by X-ray diffraction (Bruker S4 Explorer, USA), with a powder diffractometer using Cu Kα radiation sources of 40 kV. The chemical composition of the carbon products was characterized using a CHNOS (carbon, hydrogen, nitrogen, oxygen, sulphur) elemental analyser (LECO TruSpec Micro CHNS, USA). The BET surface area, pore volume and pore size distribution of the samples were analysed with a TriStar II Surface Area and Porosity Analyser. The samples were outgassed under vacuum at 200 °C for 5 hours to remove moisture content before conducting the nitrogen gas adsorption method. Surface area and pore diameter was calculated by Brunauer-Emmett-Teller (BET) method, whereas micropore volume was obtained by the t-plot method.

3.3 Research findings

3.3.1 Physical properties of HTC-biocarbons

The CHN elemental analysis allows for the determination of carbon, hydrogen and nitrogen in a sample. In a typical analysis, the sample is passed through a combustion chamber where the sample reacts with oxygen and is broken down into its elemental components: CO_2, H_2O and N_2. The gases are separated while passing through the gas chromatographic column and detected sequentially *via* infrared absorption for CO_2 and H_2O, whereas N_2 was detected using a thermal conductivity detector. The percentage composition of each element can be used to calculate the H/C ratio, which is an indicator of the saturation of the C atoms within the molecule (Frimmel et al., 2008). Suggestions can then be made regarding the aromaticity of the sample.

In the experiment involving $ZnCl_2$/NaCl as activating agent in the HTC of glucose and OPSF, the effect of $ZnCl_2$/NaCl activating agent towards increasing the carbon content of the HTC-biocarbon was greater in the HTC of OPSF compared to glucose. The results of the CHNS analysis are summarised in Table 3.2. The carbon content of HTC-biocarbon derived from glucose did not differ significantly, exhibiting a C weight% of 62.76 % and 63.75 % when glucose was subjected to HTC at 220 °C in the absence and presence of $ZnCl_2$/NaCl, respectively. On the other hand, the $ZnCl_2$/NaCl activating agent was able to increase the C weight% in HTC-biocarbon derived from OPSF, which increased from 51.61 % (without $ZnCl_2$/NaCl) to 63.20 % (with $ZnCl_2$/NaCl) at the reaction temperature of 220 °C.

Table 3.2 Reaction conditions and chemical elemental analysis for HTC-biocarbons prepared using $ZnCl_2$/NaCl as activating agent

Exp. No.	Precursor	$M_{precursor}$, [g]	$M_{catalyst}$, [g]	T, [°C]	Time, [h]	Weight %				H/C
						C	H	N	S	
G1	Glucose	6	0.0	220	12	62.76	4.66	0.12	0.63	0.88
G2	Glucose	6	13.4	180	12	58.93	2.95	0.37	0.53	0.59
G3	Glucose	6	13.4	220	12	63.75	2.55	0.42	0.48	0.47
B1	Biomass	6	0.0	220	12	51.61	8.16	9.84	1.34	1.88
B2	Biomass	6	13.4	180	12	55.68	4.19	1.51	0.63	0.89
B3	Biomass	6	13.4	220	12	63.20	3.89	0.54	0.60	0.73

Electron microscopy techniques such as scanning electron microscopy (SEM) and transmission electron microscopy (TEM) allow for the determination of morphological and crystalline properties of the HTC-biocarbons as a result of the various HTC treatments. The SEM and TEM instruments operate on the same basic principles as the light microscope but uses electrons instead of light. Because the wavelength of electrons is much smaller than that of light, the optimal resolution attainable for SEM and TEM images is many orders of magnitude better than that from a light microscope. Depending on the energy of the electron beam, different insights about the sample can be obtained. For instance, SEM images are obtained by applying an electron beam with up to an accelerating voltage of 30 kV. The electrons which are reflected off the sample surface are recorded to produce an image which contains information on the topographic nature of the specimen. TEM images are obtained when a higher accelerating voltage is applied, i.e. up to 300 kV. When an electron beam passes through a thin-section specimen of a material, electrons are scattered. A sophisticated system of electromagnetic lenses focuses the scattered electrons into an image or a diffraction pattern, or a nano-analytical spectrum, depending on the mode of operation. Images obtained from electrons which such high energy contain information on the inner morphology and crystallinity of the specimen. Thus, SEM was used to determine the surface structure, whereas TEM allowed for the determination of interior structure and crystallinity of the HTC-biocarbon prepared in this study.

Figure 3.1(a) shows the surface structure of HTC-biocarbons obtained by hydrothermal treatment of glucose for 12 h at 220 °C (sample G3). From the SEM images, the $ZnCl_2$/NaCl activation of glucose revealed agglomerated particles with an irregular and rough surface. The surface structure of HTC-biocarbons obtained by hydrothermal treatment of OPSF for 12 h at 220 °C (sample B3) is shown in Figure 3.1(b). At lower magnification, t-he FESEM images showed that the HTC-biocarbon retained the bulk fibre structure of OPSF. However, further inspection of the surface of sample B3 at higher magnification revealed a rough surface which was similar to that of sample G3, which may be attributed to the transformation of cellulose into spherical, carbon-rich structures (B. Hu et al., 2010a; Yong Wang et al., 2015c).

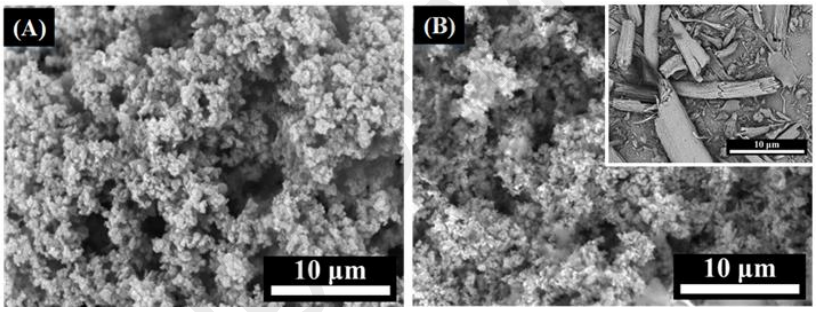

Figure 3.1 SEM image of HTC carbon obtained from (A) glucose and (B) OPSF prepared by $ZnCl_2$/NaCl-activated HTC method.

Sample B3 was selected as the sample with the highest graphitic content (based on Raman and elemental analysis) for further annealing and TEM analysis. Sample B3 was annealed under N_2 gas flow for 2 hours at 700 °C, with a heating rate of 2 °C min^{-1}. Through TEM analysis, it was observed that the rough surface observed in the SEM images can be attributed to the agglomeration of carbon nanoparticles with diameters of 100-200 nm. The TEM micrograph of annealed B3 revealed graphitic carbon nanoparticles with size between 4-5 nm decorating the surface of amorphous carbon nanoparticles (Figure 3.2).

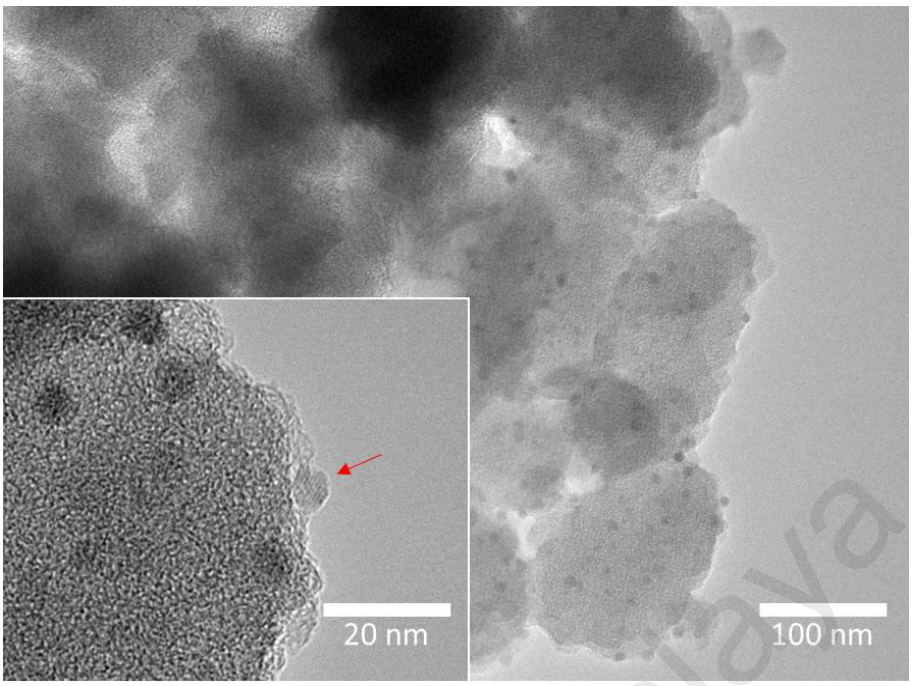

Figure 3.2 HRTEM image of HTC-treated OPSF, annealed at 700 °C under N_2 gas flow. Spherical carbon nanodots were observed to decorate the surface of the amorphous carbon bulk structure. The red arrow (inset) indicated development of graphitic nanostructures with particle size between 4-5nm.

In the experiment involving the HTC of PVA+cellulose foams, TEM analysis revealed that the HTC-biocarbon comprised of graphene-like, carbonaceous sheets interspersed with uniform carbon spheres (Figure 3.3). It may be suggested that the graphene-like, carbonaceous sheets were the product of PVA carbonisation, as the foaming and curing process produced stable thin walls arranged in a porous structure. When the PVA foam was carbonized under hydrothermal conditions, the porous structure was maintained and did not degrade under hydrothermal conditions. The formation of carbon spheres was due to the depolymerisation of cellulose followed by dehydration into soluble organic molecules such as furfural and 5-(Hydroxymethyl)furfural. Subsequently, repolymerisation of the molecules are observed and reformed into the carbonaceous spheres distinctive of HTC (Baccile et al., 2009).

When $FeCl_2$ was added to the PVA-cellulose foam before crosslinking, this resulted in $FeCl_2$ dispersed throughout the foam. The $FeCl_2$-catalysed HTC bio-carbon yielded

carbonaceous spheres with a wide size distribution and graphene-like sheets attached to the carbonaceous spheres. Additionally, highly crystalline nanorods with diameters up to 50 nm was observed in the $FeCl_2$-catalysed HTC-biocarbon sample. XRD analysis showed that the crystal structure belonged to metallic Fe. The formation Fe nanorods may be suggested to take place as follows (Llavona et al., 2013): Fe^{2+} was oxidized to Fe^{3+} under aqueous, hydrothermal conditions. Fe^{3+} could then be hydrolysed to form iron (oxy)hydroxide, FeOOH. Cl^- can be adsorbed on the [011] face of the FeOOH nanorods, thus directing the growth of FeOOH in the *c* axis direction (He et al., 2009). The conversion of FeOOH to Fe nanorods were most likely due to the reducing environment provided during the annealing step (J. Fan et al., 2015).

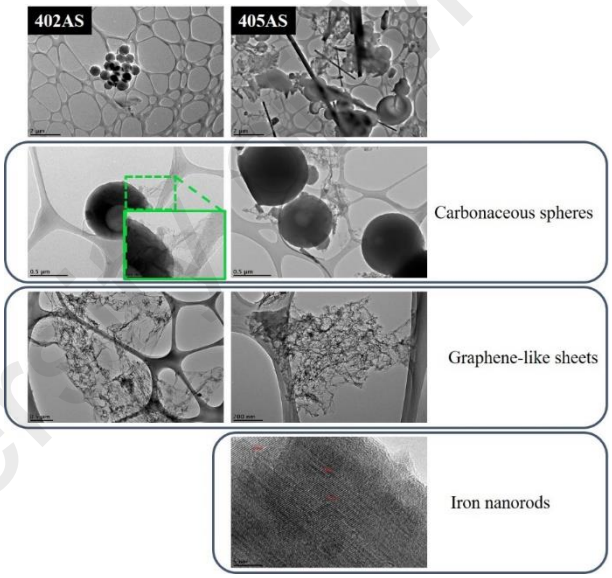

Figure 3.3 TEM images of annealed HTC biocarbon. Sample 402AS refers to uncatalysed sample whereas sample 405AS contained $FeCl_2$ catalyst.

XRD is a common technique for the study of crystal structures and atomic spacing, and is able to indicate the degree of crystallinity of the HTC-biocarbons prepared in this study. The interaction of X-rays with the sample produces constructive interference (and a diffracted ray) when conditions satisfy Bragg's Law ($n\lambda=2d \sin\theta$). This law relates the wavelength, λ of Cu radiation (λ = 1.54 Å) to the diffraction angle and the lattice

spacing in a crystalline sample. These diffracted X-rays are then detected, processed and counted. By scanning the sample through a range of *2θ* angles, all possible diffraction directions of the lattice should be attained due to the random orientation of the powdered material.

Figure 3.4 summarises the XRD patterns of the HTC-biocarbons obtained *via* $ZnCl_2$/NaCl activated HTC of glucose and OPSF. Samples G1, G2 and G3 displayed broad peaks at 2θ = 10 ° and 20 ° which indicated that the HTC-biocarbons were mainly amorphous, or nanographitic in nature (Shang et al., 2015). The XRD spectrum of sample B1, which was obtained by HTC of OPSF at 220 °C without $ZnCl_2$/NaCl activating agent (Figure 3.4b) revealed characteristic peaks of crystalline cellulose at diffraction angles of 2θ = 14.8, 16.3 and 22.6°, which are assigned to the [101], [$10\bar{1}$] and [200] diffraction planes, respectively (Egusa et al., 2009; Pang et al., 2014). This again indicated that the cellulosic structure was not fully degraded in the absence of $ZnCl_2$/NaCl activating agent. The addition of activating agent resulted in the complete transformation of cellulose to HTC-biocarbon product at a lowered temperature requirement of 180 °C (sample B2), whereas an increase in temperature from 180 °C to 220 °C resulted in a slight increase in [200] peak intensity (sample B3).

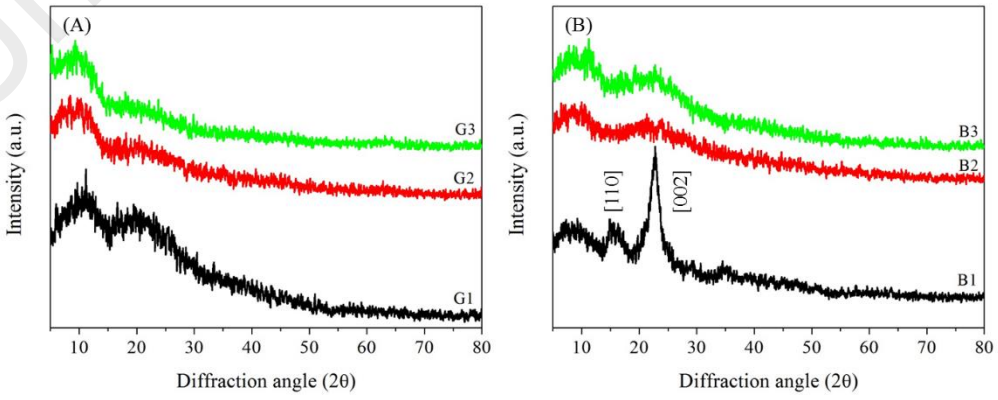

Figure 3.4 XRD diffractograms of HTC-biocarbon obtained from (A) glucose and (B) OPSF.

The XRD patterns of HTC-biocarbon samples prepared by the PVA soft templating method is presented in Figure 3.5. The HTC-biocarbons prepared from PVA-cellulose foam (C402 and C405) did not show sharp, crystalline peaks, indicating the amorphous nature of the HTC-biocarbon products. Upon annealing, broad peaks at 2θ = 23.2 °, 43.2 ° and 55.8 ° were observed in samples C402AS and C405AS, and this indicated the formation of polycrystalline graphite. The XRD pattern of the C405AS sample showed additional peaks at 2θ = 44.5 °, 65.2 °, 82.6 ° which corresponded to the [011], [002] and [112] phases of metallic iron (COD reference pattern: 96-901-3415), supporting the observation of crystalline nanorods in the corresponding TEM image.

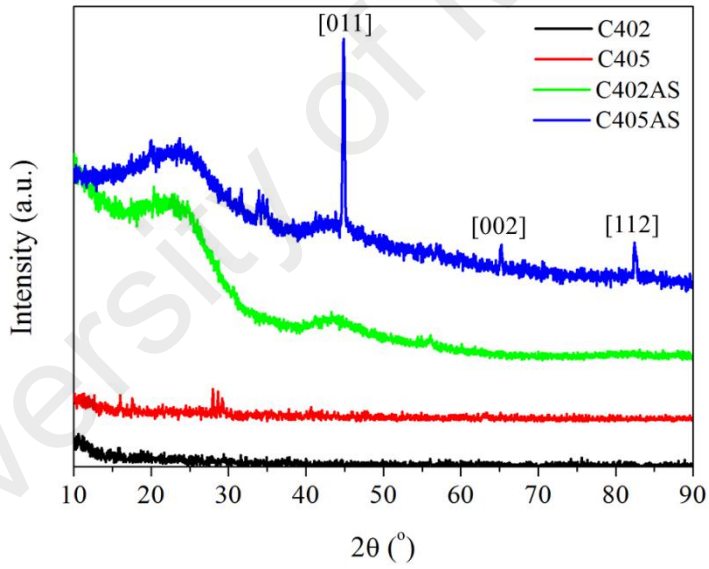

Figure 3.5 XRD difraction patterns of PVA-templated HTC-biocarbons with (C402) and without (C405) catalyst. C402AS and C405AS refers to the XRD patterns of the annealed C402 ans C405 samples, respectively.

The determination of surface area of a material depends on the BET theory on multi-layer adsorption of gases on the surface of solid materials. The specific surface area of a powder is determined by allowing an inert gas such as N_2 to adsorb physically on the

surface of the solid and by calculating the amount of adsorbate gas corresponding to a monomolecular layer on the surface.

Using the $ZnCl_2$/NaCl hydrothermal treatment method on OPSF, BET surface area analysis showed the formation of a large surface area up to 597.6 m^2 g^{-1} (Sample B3), compared with 347.6 m^2 g^{-1} for the uncatalysed sample (Sample B1) (Figure 3.6). The micropore volume was increased from 0.148 (Sample B1) to 0.243 (Sample B3) cm^3 g^{-1} as a result of adding $ZnCl_2$/NaCl as activating agent. HTC-biocarbon obtained from OPSF precursor at 220 °C indicated Type II adsorption (Sample B1). With the addition of $ZnCl_2$/NaCl catalyst at 220 °C, Type I isotherm behaviour was observed for sample B3, indicating the formation of well-defined microporous structure (Lowell and Shields, 1991).

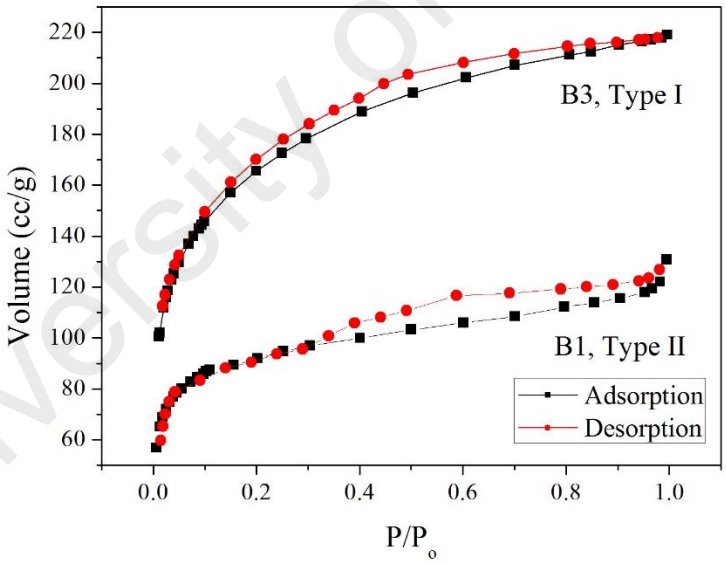

Figure 3.6 BET adsorption isotherm reveals Type II adsorption when OPSF was subjected to uncatalysed HTC at 180°C. With the addition of $ZnCl_2$/NaCl catalyst at 220°C, Type I adsorption-desorption was observed for sample B3, indicating the formation of well-defined microporous structure.

3.3.2 Chemical properties of HTC-biocarbons

To understand the chemical nature of the HTC-biocarbons, Fourier transform infrared (FTIR) spectroscopy is a useful analytical technique to identify the types of bonding present within the sample. FTIR spectroscopy involves the transmission of infrared (IR) radiation through the sample, whereby frequencies which are resonant to the chemical bond within the sample will be absorbed. The intensity of absorption in the IR spectrum is related to the change in the dipole moment, depending on the vibration mode in the molecule. Any radiation that is not absorbed by the sample passes through and is recorded by a detector, therefore the FTIR spectrum represents the molecular transmission of the sample. Thus, FTIR spectroscopy can be used to determine the aliphatic and/or aromatic nature of the prepared HTC-biocarbons.

From Figure 3.7, C-H stretching peaks were observed in HTC-biocarbons prepared using $ZnCl_2$/NaCl activating agent. The intensity of the peaks between 2800 to 3000 cm^{-1} reduced slightly as a result of adding $ZnCl_2$/NaCl activating agent (sample B2) and increasing the HTC reaction temperature (sample B3). Weak peaks observed between 1200 to 1000 cm^{-1} are a result of C-O stretching in the alcohol functional group (Balahmar et al., 2015). These peaks were most apparent in the uncatalysed glucose sample, but has diminished in the other samples. This is in agreement with previous work that the C-O bond breaking occurs due to presence of acid catalyst, and indicates that $ZnCl_2$/NaCl activating agent assisted in the gasification of C-O bonds to CO_2 (Watanabe et al., 2005). The presence of aromatic rings in the HTC-biocarbon is indicated by the peaks in the 1400 to 1600 cm^{-1} region, which corresponds to aromatic C=C stretching.

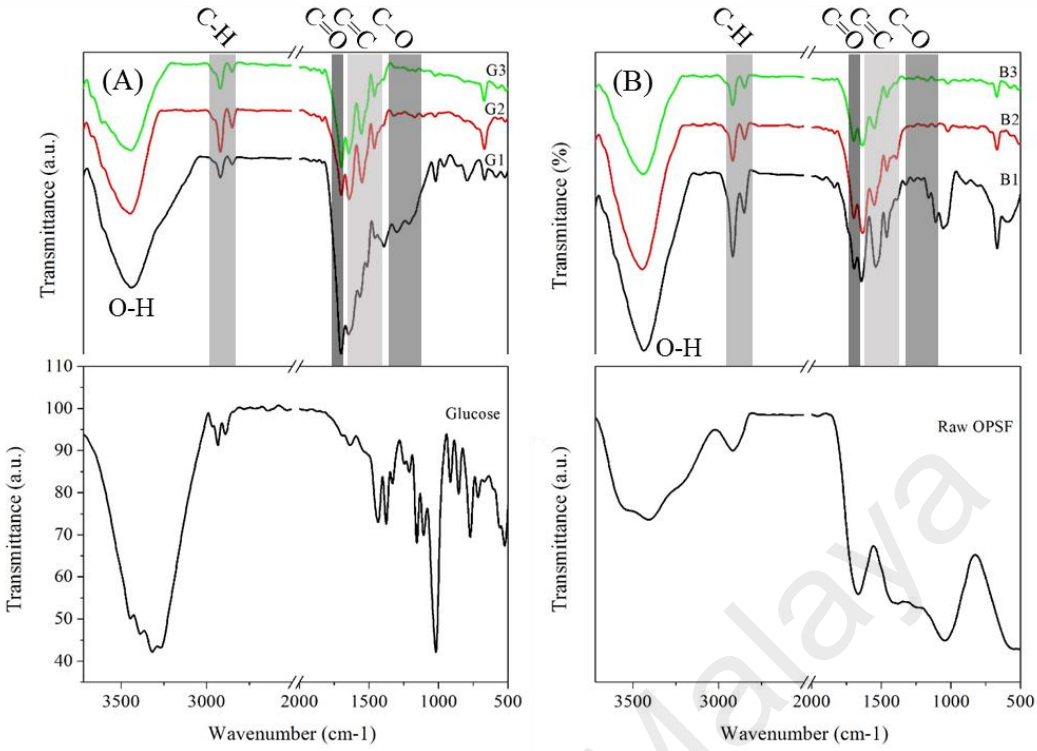

Figure 3.7 FTIR spectra of (a) HTC-treated glucose and (b) HTC-treated OPSF.

FTIR spectrum of HTC-biocarbons prepared by PVA-templating method without any catalyst (sample C402, Figure 3.8) showed a strong C-O peak at 1000 to 1200 cm^{-1} region, indicating that the HTC-biocarbon contained substantial alcohol functional groups. The addition of $FeCl_2$ catalyst accelerated the C-O bond breaking, corresponding with the diminishing of the C-O peak in sample C405. The intensity of the peak at 1700 cm^{-1}, corresponding to the vibration of C=O bonds, indicated that the annealing step provided an inert environment for the thermal oxidation of C=O functional groups to CO_2.

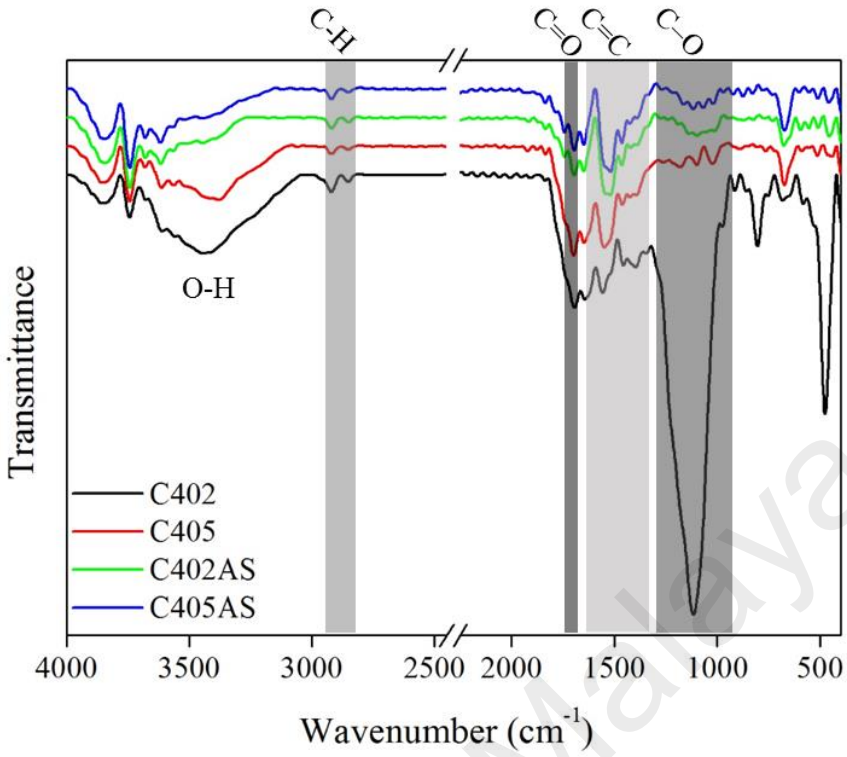

Figure 3.8 FTIR spectra of PVA-templated HTC of cellulose, whereby C402 – uncatalysed sample, C405 – $FeCl_2$ catalysed sample. Samples C402AS and C405AS represent the FTIR spectra of the respective annealed HTC-biocarbons.

Raman spectroscopy is an analytical technique that detects changes in polarizability, and it is a complementary technique to FTIR. Raman scattering is a phenomenon in which inelastic light scatters due to symmetrical bond vibration. Usually, Raman spectroscopy of amorphous carbon materials indicates characteristic peaks of 1300 cm^{-1} and 1590 cm^{-1}, referring to D band and G band, respectively (Dresselhaus et al., 2010). Raman analysis is able to check for the presence of aromatic structures in the samples by analysing the intensity of the G band. The G band of the samples indicate the E_{2g2} mode of graphite, sp^2 C=C stretching ability, or a combination of both (Schwan et al., 1996).

The Raman spectra of the HTC-biocarbon samples prepared by $ZnCl_2$/NaCl activation show G peaks around 1580-1600 cm^{-1} and D peaks around 1350 cm^{-1} (Figure 3.9). Raman spectroscopy indicated the presence of nanocrystalline graphite indicated

by G peak position at 1600 cm^{-1} (A. C. Ferrari and Robertson, 2000). The I_D/I_G ratio decreased with the temperature and in the presence of catalyst, which corresponded to an increase in sp^2 ring structure (Schwan et al., 1996). When the temperature of the hydrothermal reaction was increased, the free energy in the system increases also to allow for faster reaction rates to produce a carbon product of higher carbon density (e.g. fragmentation, dehydration, decarboxylation, dehydrogenation). Previous studies have reported decreasing I_D/I_G ratio, as the result of chemical reactions and crystal rearrangement at higher temperatures (Sevilla and Fuertes, 2009b; X. Zhu et al., 2015). An observed increase in the number of defects may be possible when the sample is exposed to oxidative conditions i.e. presence of O_2, allowing for accelerated oxidation reaction (C. S. S. R. Kumar, 2012). However, the amount of O_2 present under hydrothermal conditions is limited, thereby limiting the oxidation of HTC-biocarbon.

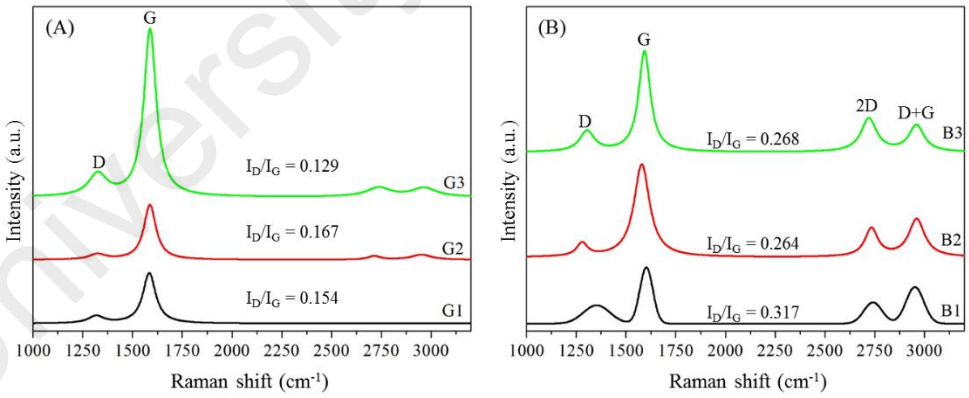

Figure 3.9 Raman spectra of HTC-biocarbons prepared using $ZnCl_2$/NaCl-activated HTC method on (a) glucose and (b) OPSF as renewable carbon precursors.

For PVA-templated HTC of cellulose, the I_D/I_G ratio increased slightly from 0.15 (C402) to 0.18 (C405) with the addition of $FeCl_2$ catalyst, which suggested that the

$FeCl_2$ catalyst only mildly increased the sp^2 content of the HTC-biocarbon (Figure 3.10). The absence of 2D and D+G peaks suggest that an amorphous, glassy carbon structure was formed as a result of the annealing step. The annealed samples (C402A and C405A) demonstrated lower G peak intensity compared to the pre-annealed samples (C402 and C405), which may suggest the formation of disordered, sp^2 bonded HTC-biocarbon products during the annealing step (Andrea C. Ferrari, 2007). The intense D and G bands of sample C402 and C405 may be attributed to the presence of aromatic molecules containing sp^2 bonded carbons formed during the HTC process. These sp^2 containing compounds may be low-molecular weight compounds and are easily decomposed at elevated temperatures. Thus, the Raman spectra of C402AS and C405AS corresponds with the loss of sp^2 content as a result of removing the aromatic molecules with low molecular weight, also observed in TGA analysis.

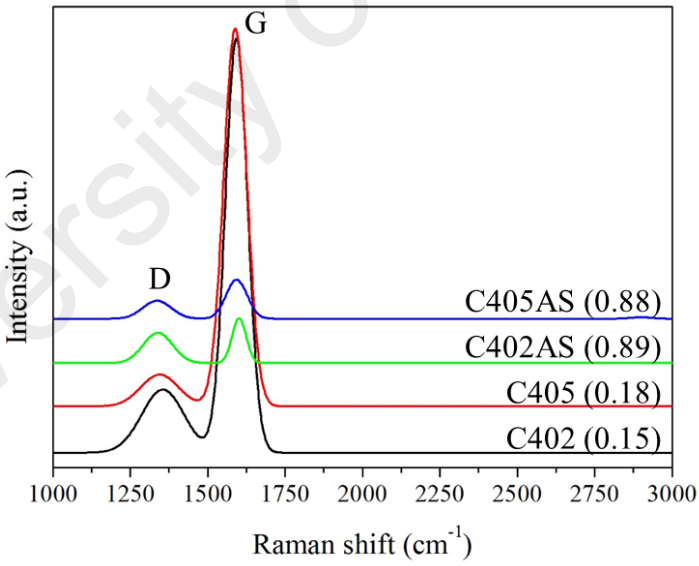

Figure 3.10 Raman spectra and I_D/I_G ratio of PVA-templated HTC-biocarbons in the absence (C402) and presence (C405) of $FeCl_2$ catalyst. Samples C402AS and C405AS represent the Raman spectra of the respective annealed HTC-biocarbons.

Thermogravimetric analysis (TGA) was performed on the HTC-biocarbons to investigate the thermal properties of the HTC-biocarbons prepared *via* the $ZnCl_2$/NaCl-activated and PVA-templated HTC methods. For all HTC-biocarbon samples, three regions of mass loss were observed, i.e. (1) 30-300 °C, (2) 300-500 °C and (2) 500-850 °C. The first region of mass loss is usually attributed to the evaporation of adsorbed H_2O and volatile organic compounds (VOC) (Nizamuddin et al., 2015). Thus, the TGA curve for the HTC-biocarbon prepared by $ZnCl_2$/NaCl activated HTC of glucose and OPSF (Figure 3.11) revealed a H_2O content of up to 10 %. In contrast, the HTC-biocarbon obtained from the HTC of PVA-cellulose foams showed a moisture content of ~5 % (Figure 3.12). The maximum mass loss rate observed at approximately 400 °C corresponds with the pyrolytic decomposition of cellulose to form gaseous products i.e. CO_2, CO and CH_4 (H. Yang et al., 2007). The authors reported that the pyrolysis of cellulose is an endothermic process, releasing CO_2, CO and CH_4 as the main gas products. TGA results estimate that the product yield of annealing the HTC biocarbons were 40% and 50% for the $ZnCl_2$/NaCl-activated and PVA-templated HTC methods, respectively.

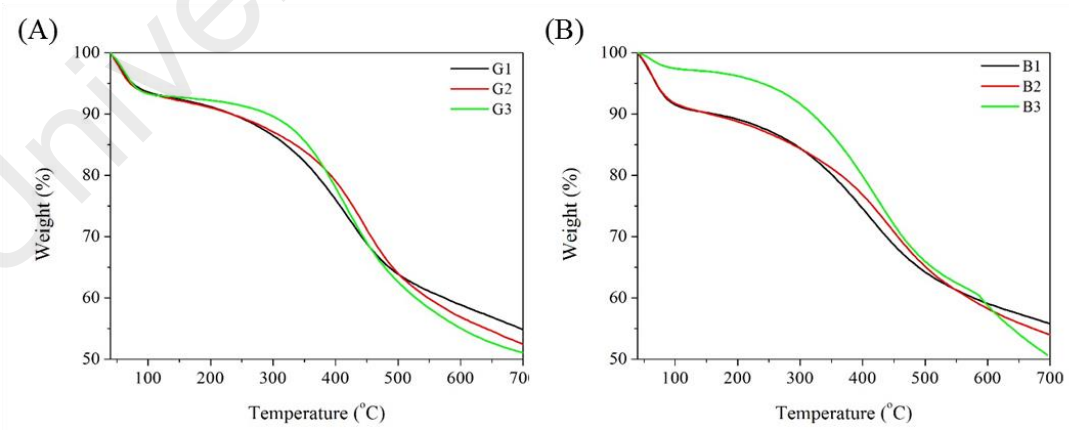

Figure 3.11 TGA curves of $ZnCl_2$/NaCl-activated HTC-biocarbon obtained from HTC of (A) glucose and (B) OPSF.

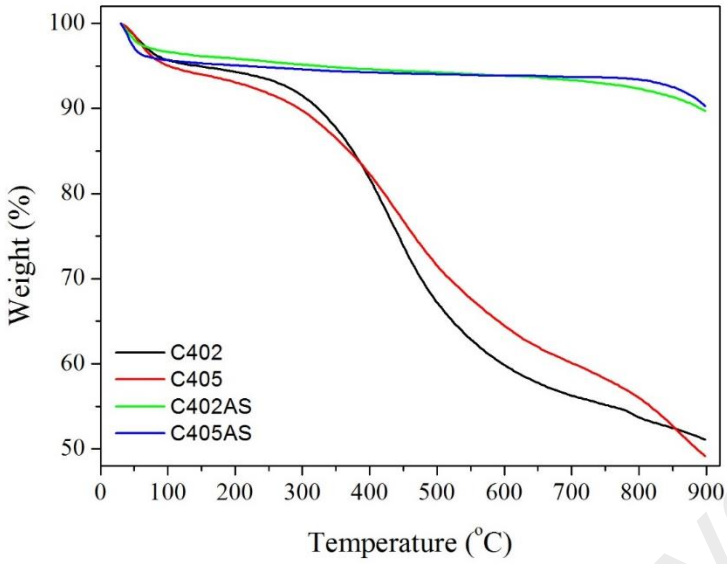

Figure 3.12 TGA curves of PVA-templated HTC-biocarbons in the absence (C402) and presence (C405) of $FeCl_2$ catalyst. Samples C402AS and C405AS represent the TGA curves of the respective annealed HTC-biocarbons.

3.4 Discussion

In this section of the study, the effect of $ZnCl_2$/NaCl and PVA as activating agents and soft template, respectively, were investigated with regards to the physical and chemical properties of the HTC-biocarbon products. The search to identify appropriate catalysts contributes towards the carbonisation of increasingly complex organic polymers such as cellulose and OPSF at lower temperatures. Innovations to the HTC process may also increase the yield and surface area of the HTC-biocarbon product, as well as to reduce post-treatment of the product.

The research findings from this study agrees with published literature that the addition of an activating agent ($ZnCl_2$/NaCl) was able to reduce the temperature requirement for carbonizing complex raw carbon precursors, possibly by promoting the dehydration process. The $ZnCl_2$/NaCl-activated HTC was able to completely carbonize OPSF at 180 °C, and the surface area up to 597.6 m^2 g^{-1} was achieved when OPSF was used as raw carbon precursor. The chemical activation step resulted in the conversion of

the adsorption properties from Type II to Type I, which indicated the formation of mesoporosity in the HTC-biocarbon.

Due to the complexity of the carbonisation process, it was a challenge to pinpoint the exact role of catalyst in the carbonisation process. It was proposed previously that the mechanism of carbonisation includes a hydrolysis phase to break the cellulose chains into oligosaccharides (Sevilla and Fuertes, 2009b), followed by dehydration to form furan compounds (Xiao et al., 2012). In the presence of acid, simple sugars are reduced to furfural (Sevilla and Fuertes, 2009b). The oligosaccharides, phenolic, and furan compounds then become repolymerized to form soluble chains. Subsequently, C=C bonds are produced *via* keto-enol tautomerisation and intramolecular dehydration. When threshold conditions are achieved, carbon nuclei particles are formed and further crosslinking between these compounds lead to the growth in the carbon particles (Ryu et al., 2010). As $ZnCl_2$ is also a Lewis acid, it is probable that the incorporation of $ZnCl_2$ into the HTC process accelerated the carbonisation process by breaking bonds in the lignocellulosic structure *via* electrophilic attack i.e. Zn^{2+} ions activate the C-H, C-O, or C-C bonds (Molina-Sabio and Rodrıguez-Reinoso, 2004). Lewis acid catalysts were also previously reported to promote polymer crosslinking, graphitisation, and hydrochar yield (Yibing Cai et al., 2007).

The $ZnCl_2$/NaCl and PVA techniques both resulted in the preparation of HTC-biocarbon with expanded physical structures, whereby the $ZnCl_2$/NaCl activation technique increased the surface area *via* chemical means and the PVA-templating resulted in an expanded physical structure by introducing an expanded physical structure. When a soft template was incorporated into the HTC process, a carbon foam was successfully synthesised from the HTC of PVA+cellulose foam at 220 °C. A carbon hybrid composite comprising carbonaceous spheres and multi-layer graphene sheets

was formed through the two step carbonisation of PVA-cellulose foam as observed through SEM & TEM. The addition of $FeCl_2$ accelerated the HTC process and when incorporated into the thermal activation step at 800 °C, resulted in the formation of iron nanorods which conferred magnetic properties to the HTC-biocarbon.

CHAPTER 4: NANOSTRUCTURED CARBON AS PHOTOCATALYTIC PROMOTER AT THE COLLECTOR-SEMICONDUCTOR INTERFACE

4.1 Introduction

An efficient PEC water-splitting system is one that is able to convert photons to H_2 fuel with minimal energy loss due to heat. The conversion of photons to H_2 fuel is a two-part process involving (1) the generation of photoexcited charge carriers at the photoanode (photo-conversion efficiency) and (2) reaction of the charge carriers in water-splitting redox reactions at the cathode (Faradaic efficiency). The photo-conversion efficiency of a material is expressed using the Applied Bias Photon-to-Current Efficiency (ABPE) formula (Hisatomi et al., 2014):

$$ABPE(\%) = \left(\frac{\left[J_p \times [1.23V - V_b]\right]}{P_{tot}}\right) \times 100\% \qquad \text{(Eq. 4.1)}$$

Whereby J_P = photocurrent density at applied bias V_b (mA cm^{-2}), V_b = applied bias (V), and P_{tot} = power density of the incident light (mW cm^{-2}). A material's ability to produce a photocurrent, J_P is dependent on its charge transfer properties which in turn affects charge separation efficiency and recombination rate. Efficient charge separation is achieved when electrons are able to diffuse away from its photogeneration site *via* electron pathways with low resistance. An increase in charge separation efficiency suppresses the recombination of photogenerated electron-hole pairs and at the same time, increases the probability of the electron-hole pairs to participate in water-splitting redox reactions (Zhebo Chen et al., 2013b). Therefore, the modification of ZnO to improve its charge transfer properties will be able to improve its solar conversion efficiency as a PEC water-splitting photoanode.

Doping ZnO with impurity atoms is a widely-used strategy to improve the charge transfer within the bulk semiconductor material. ZnO in itself has a large dispersion, conferring the semiconductor with higher electron mobility compared to TiO_2. The electron mobility of ZnO can be further increased by increasing the material's minority carrier density. A change in the carrier density of ZnO enables it to behave as n-type in an excess of donor impurities, or to behave as a p-type in the excess of acceptor impurities. Cu is a d^9 transition element and behaves as an electron acceptor. Previous studies involving the doping of Cu into ZnO has resulted in the claims of formation of p-type ZnO with enhanced photocatalytic activity for dye degradation. Additionally, doping introduces energy levels into the CB of the semiconductor and narrows the band gap – enhances light absorption. Cu-doping might be able to improve the photo-conversion efficiency of ZnO as a photocathode by forming a p-type semiconductor and improving electron transport across the bulk.

The hybridisation of ZnO with electron transfer agents are able to improve the charge transfer at the solid-solid interface. Charge transfer at the solid-solid interface is able to improve charge-separation efficiency by offering a conductive electron pathway for transporting photogenerated electrons away from the site of photoexcitation. Semiconductors display temperature-dependent properties with regards to electron mobility at the interface. At low temperatures, interfacial charge transfer occurs *via* thermally-activated hopping whereas metal-like thermal resistance is observed at higher temperatures (Sewell, 1963). rGO is an electroconductive material due to its sp^2 properties, which has been discussed in detail in Chapter 2. The hybridisation of semiconductors with semiconductors such as ZnO involves the formation of intermolecular bonding such that electron transfer is possible between the two materials. Therefore, hybridising ZnO with rGO is an attractive non-metal strategy to improve the

charge separation efficiency in ZnO, leading to the improvement in photo-conversion efficiency.

This chapter explores the modification of ZnO to improve its charge transfer properties using two approaches (1) combining doping + hybridisation and (2) modifying the electrochemical reduction parameters (potentiostatic/potentiodynamic and electrolyte solution) Section 4.1 reports the preparation of rGO/Cu-ZnO photoanode as a preliminary exploration on the effect of combining Cu-doping and rGO-hybridisation. Section 4.2 presents a study on the effect of rGO prepared by potentiostatic and potentiodynamic reduction methods towards the photo-conversion efficiency of the rGO/ZnO photoanode.

4.2 rGO/Cu-ZnO photoanodes for PEC water-splitting: a preliminary study

The control of both charge transfer processes i.e. transfer within the bulk nanostructure and at the solid-solid interface is necessary for optimal solar conversion of the device. For this reason, the improvement of ZnO charge transfer properties may benefit using a combined doping + hybridisation approach. Therefore, a preliminary study on improving the photo-conversion efficiency of ZnO using a combination of Cu-doping and rGO-hybridisation was explored and presented in this section.

4.2.1 Materials and methods

GO was prepared using a modified Hummer's method. Zinc(II) nitrate hexahydrate, $Zn(NO_3)_2 \cdot 6H_2O$ and ethylenediamine (EDA), $C_2H_4(NH_2)_2$ were obtained from R&M Chemicals (Malaysia), whereas phosphate buffer solution (pH 7), potassium hydroxide, KOH and potassium chloride, KCl were purchased from Merck (USA). Indium-doped

tin oxide (ITO)-coated glass with sheet resistance of < 7 Ω sq^{-1} purchased from Magna Value Sdn. Bhd. (Malaysia) was used as the conductive substrate for the electrodeposition of rGO and ZnO films.

4.2.1.1 Electrochemical deposition of rGO/Cu-ZnO films

Prior to the electrochemical deposition of rGO and ZnO on ITO substrate, the ITO substrate in 1 cm x 2 cm dimensions were cleaned by immersion and sonication in 10% HNO_3, deionised H_2O, ethanol and acetone (R&M Chemicals, Malaysia) successively before drying at 50 °C.

The electrochemical reduction of GO to rGO was performed following a published method (Upadhyay et al., 2014) and is summarised in Figure 4.1. The electrochemical reduction process was carried out in a three-electrode electrochemical cell consisting of cleaned ITO glass as the working electrode, a platinum wire counter electrode and an Ag/AgCl (3 M) as the reference electrode. The electrodes were immersed in an electrolyte solution containing a 7 mg L^{-1} solution of GO dispersed in 0.1M KOH solution (pH 12, Merck). The electrochemical reduction of GO to rGO was performed under cyclic voltammetry mode between 0.0 to -1.5 V, with a scan rate of 10 mV s^{-1} for four cycles.

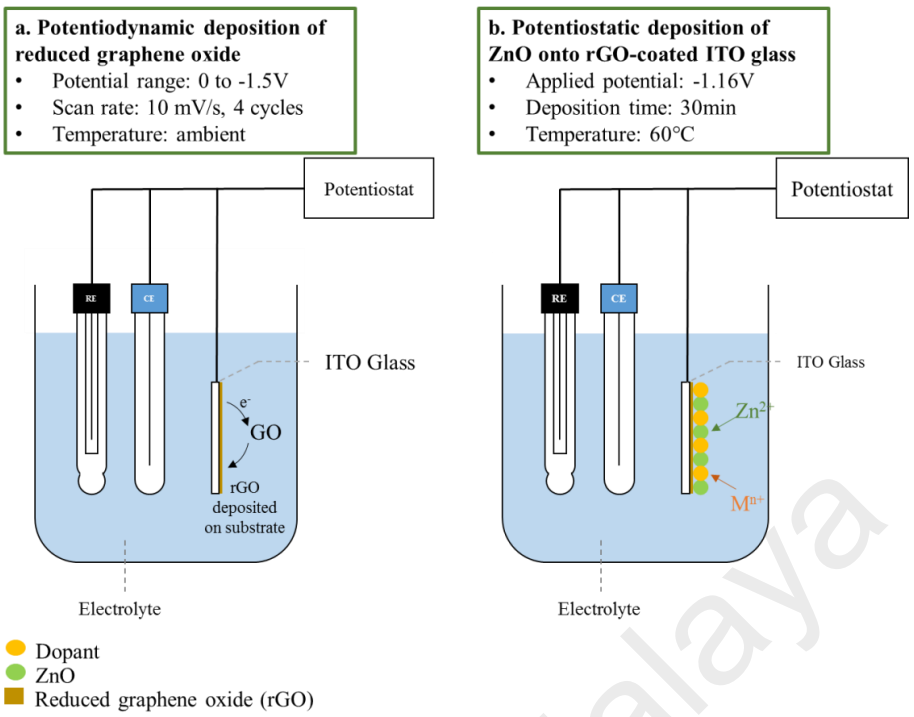

Figure 4.1 Schematic diagram depicting experimental methods of (a) electrodeposition of rGO and (b) electrodeposition of ZnO thin films.

The rGO-hybridised, Cu-doped ZnO (rGO/Cu-ZnO) film was prepared by electrochemical deposition of Cu-doped ZnO film on rGO-coated ITO substrate. $Zn(NO_3)_2 \cdot 6H_2O$, $Cu(NO_3)_2 \cdot 6H_2O$, KCl and EDA were used as zinc precursor, dopant, supporting electrolyte and structure directing agent, respectively. The electrolyte solution was prepared by dissolving 1.487 g of $Zn(NO_3)_2 \cdot 6H_2O$, 0.372 g of KCl, 5 mL of 0.1 M EDA and 0.012 g $Cu(NO_3)_2 \cdot 6H_2O$ solution to 50 ml with deionized H_2O. Thus, a cloudy solution was produced with a concentration of 0.1 M $Zn(NO_3)_2 \cdot 6H_2O$, 0.1 M KCl, 0.01 M EDA and 0.001 M $Cu(NO_3)_2 \cdot 6H_2O$. A fresh, unused solution was prepared for the deposition of each thin film. The Cu-ZnO film was deposited on rGO-coated ITO substrate by applying a constant voltage of -1.16 V for 30 minutes and using the three-electrode electrochemical cell setup in Figure 4.1. The electrolyte solution was maintained at 60 °C during the electrochemical deposition process. The as-prepared film was gently rinsed with deionized H_2O so as not to damage the thin film coating by

mechanical abrasion and allowed to air-dry in a desiccator before annealing. The crystallinity of the films was improved by thermal annealing at 300 °C for 2 hours, at a heating rate of 1 °C in argon gas flow.

Control films of ZnO, Cu-doped ZnO (Cu-ZnO) and rGO-hybridised ZnO (rGO/ZnO) were prepared as well, to investigate the individual effects of Cu-doping and rGO towards ZnO photo-conversion efficiency.

4.2.1.2 Material characterisation

The materials characterisation of the thin films was as follows. The morphology of the samples was investigated by FESEM, using a SUPRA^{TM} 35 VP Field Emission Scanning Electron Microscope (Carl Zeiss, Germany) equipped with an energy-dispersive analysis system (EDS), which was employed to obtain an insight into the bulk element composition of the sample. The crystallinity of the thin films were characterized with X-ray diffraction (XRD) using a model D8 ADVANCE X-ray diffractometer (Bruker, Germany) equipped with Cu Kα radiation (λ = 1.5418 Å) at 40 kV and 30 mA. All the patterns were recorded in the 5–90 ° range, with a step size of 0.02 °. The phase identification of the samples were performed with HighScore Plus software and using reference patterns from the Crystallography Open Database (COD) (Gražulis et al., 2012). Raman scattering measurements were made with an in*Via* Raman spectrometer (Renishaw, UK) using a 514 nm wavelength incident laser light and a 100× objective. Photoluminescence properties of the samples were recorded using the same Renishaw In*Via* system but using 325 nm wavelength incident laser light. The UV–Vis diffuse reflectance spectra were recorded on a UV-2600 spectrophotometer (Shimadzu, Japan) equipped with an integrating sphere (ISR-2600). X-ray photoelectron spectroscopy (XPS) measurement were done using a high pressure XPS setup at the

Fritz Haber Institute (Berlin, Germany) with a base pressure of 2 x 10^{-9} mbar, using a non-monochromatic Al Kα X-Ray source (hν = 1486.6 eV) and a hemispherical electron analyser. The spectrometer was calibrated to yield the standard 932.7 eV for Cu2p(3/2) binding energy and 84.0 eV for Au4f(7/2) on an Ar^+ sputtered Cu and Au foil, respectively. For the ultraviolet photoelectron spectroscopy (UPS) measurements a VUV He I (21.22 eV) source was used. The base pressure during the UPS measurements reached 1 x 10^{-8} mbar due to the He gas. A bias of -15.0 V was applied to the samples during the UPS measurements. The spectra were taken using an E_{pass} = 1 eV. All spectra were referenced to the Fermi edge measured for an Ar^+ sputtered Cu foil measured in the same conditions as the samples.

The electrochemical characterisation of the thin films were carried out in a three-electrode PEC water-splitting cell, consisting of the thin film sample as the working electrode, a platinum wire counter electrode and an Ag/AgCl (3 M) as the reference electrode (Autolab PGSTAT302N potentiostat/galvanostat, Metrohm, Netherlands). Simulated solar light comprising a spectrum range of 200-2500 nm was irradiated on the samples using a 150 W Xe lamp (Model LSP-X150, Zolix, China). The intensity of the light was maintained at 100 mW cm^{-2} by maintaining a constant input current of 8.34 A, as well as maintaining a constant distance between the light source and the PEC water-splitting cell. The electrochemical measurements were conducted using an aqueous 0.1 M KOH electrolyte solution (pH 11).

Linear scan voltammetry (LSV) analysis was performed in the dark and under simulated solar light irradiation. The linear scan voltammetry was recorded in the anodic direction, in the range of -1.0 V to +1.0 V. Chronoamperometry (*I–t*) measurements was performed at open circuit potential, V_{OC} vs. Ag/AgCl over

continuous light on–off cycles. EIS measurements were conducted in the 100 mHz to 1 MHz frequency range, with an amplitude of 10 mV at 0 V.

4.2.2 Data analysis

The physical, optical and electrochemical properties of the prepared ZnO, rGO/ZnO, Cu-ZnO and rGO/Cu-ZnO films were analysed in order to understand the effect of Cu-doping and rGO hybridisation on the photo-conversion efficiency of ZnO. The physical properties were characterized using FESEM, XRD and Raman techniques (Section 4.1.2.1), whereas the optical properties were characterized using PL, UV-Vis and UPS techniques (Section 4.1.2.2). Chronoamperometry, LSV and EIS techniques were used to determine the electrochemical properties of the films (Section 4.1.2.3).

4.2.2.1 Physical properties

The top-view FESEM images shown in Figure 4.2 for ZnO films grown *via* electrochemical deposition on ITO substrate reveal that the films consist of dense arrays of vertically-aligned ZnO nanorods. The vertical growth of ZnO nanorods was due to the presence of EDA as structure directing agent (Fragalà et al., 2010). EDA is a bidentate ligand and forms a complex with Zn^{2+} ions, thus controlling the manner Zn^{2+} ions approach the nucleation site (F. Xu et al., 2009b). EDA also binds to the non-polar [101] and [110] surfaces of the ZnO crystal, thus directing the addition of Zn^{2+} ions in the [002] direction (X. Gao et al., 2005; B. Liu and Zeng, 2004). However, in this preliminary study, the electrodeposition parameters were not well-controlled, giving rise to a two-phase hybrid film structure. Generally, the bottom phase of the thin film consists of ordered, vertically-aligned ZnO nanorods whereas the top phase consisted of

randomly-structured nanoparticles. For example, the unmodified ZnO film consisted of vertically-aligned nanorods with a consistent diameter of approximately 300 nm and terminated in a flat-top manner i.e. exposed [002] facet in the bottom phase of the thin film (Figure 4.2a), whereas the top phase of the ZnO film consisted of micro-sized ZnO flakes. The rGO/ZnO film (i.e. ZnO grown on rGO coated ITO glass) featured non-uniformed rod diameters ranging between 100 to 600 nm in the bottom phase (Figure 4.2c), whereas nanoflowers and micro-sized flakes were observed on the top layer. When Cu was incorporated into the electrolyte solution, ZnO nanorods with tapered ends were formed in the bottom phase, both for Cu-ZnO (Figure 4.2b) and rGO/Cu-ZnO samples (Figure 4.2d). Cu-doping also appeared to control the structure of the thin film's top phase, whereby Cu-doped films featured nanospikes (Figure 4.2f,h), whereas micro-sized flakes are distributed on the surface of undoped ZnO and rGO/ZnO films (Figure 4.2e,g). It is most likely that the electrodeposition time of 30 minutes allowed for a runaway nucleation and crystal growth reaction to occur, leading to the formation of the second, randomly structured phase. Therefore, the duration of the electrodeposition time needs to be reduced in order to prevent runaway crystal growth.

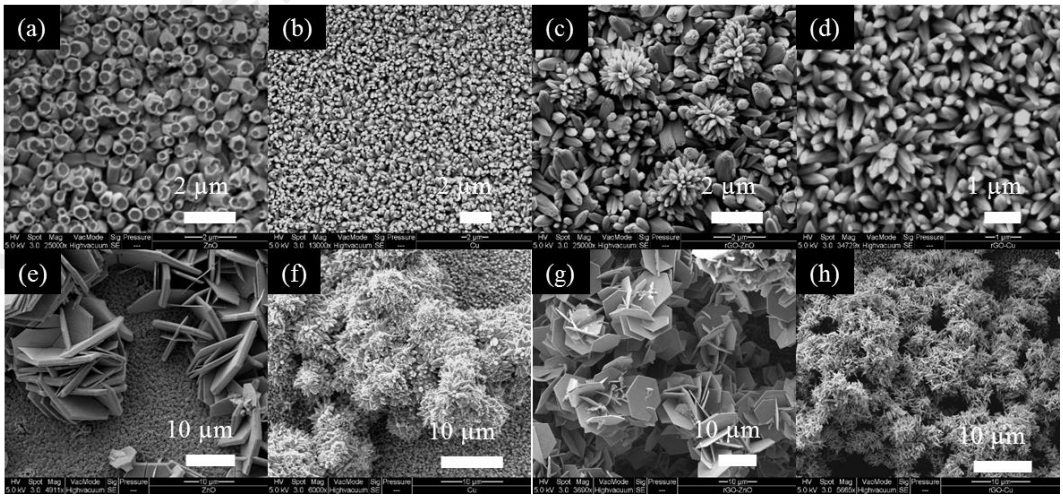

Figure 4.2 FESEM images of vertically-aligned ZnO nanorods (a) ZnO (b) Cu-ZnO, (c) rGO/ZnO and (d) rGO/Cu-ZnO. (e-f) Low magnification mages of runaway crystal growth for each corresponding film

XRD analyses the light-diffracting properties of a sample and, in so doing, provide information regarding the phase and crystal structure of a sample. Each crystal lattice will diffract light in a unique manner according to the interatomic spacing (d-spacing) between atomic planes within a 3-dimensional structure. An XRD instrument operates by directing a beam of X-rays with known wavelength, λ on to the sample and measuring the angle, θ of the diffracted X-rays coming out of the sample (Suryanarayana and Norton, 2013). With this information (λ and θ), the interatomic spacing between atomic planes can be solved using Bragg's equation: $n\lambda=2d\sin\theta$, where n = a positive integer, λ = wavelength (in Å), d = interatomic spacing (in Å) and θ = diffraction angle in degrees.

Figure 4.3 reports the XRD diffractograms for ZnO, rGO/ZnO, Cu-ZnO and rGO/Cu-ZnO thin films. Peaks were observed at 2θ = 32.1 °, 34.9 °, 36.5 °, 47.8 °, 57.1 °, 63.1 °, 67.1 °, 68.5 ° and 72.7 °, which corresponds to the [010], [002] [011], [012], [110], [013], [020], [112] and [004] plane orientations, respectively. The peaks indicated by stars correspond to the ITO supporting substrate. The diffraction patterns of the samples indicated the formation of ZnO in the wurtzite phase (COD Reference Pattern: 96-101-1259), which is agreeable with previous work (Zi et al., 2014). The [002] peak at 2θ = 34.9 ° was the most intense peak for all samples, corresponding with the observation of vertically-aligned ZnO nanorods in the FESEM images (Farhat et al., 2015; Reddy et al., 2014). The rGO-hybridisation and Cu-doping methods reduced the relative intensities of the [010] and [011] peaks, which was consistent with the narrowing of the ZnO nanorod diameter observed in FESEM. As there were no significant shifts in peak position, and no peaks related to metallic Cu or its oxides were

observed, this indicated Cu was present as ions in the ZnO crystal lattice, instead of the formation of metallic Cu, Cu_2O or CuO.

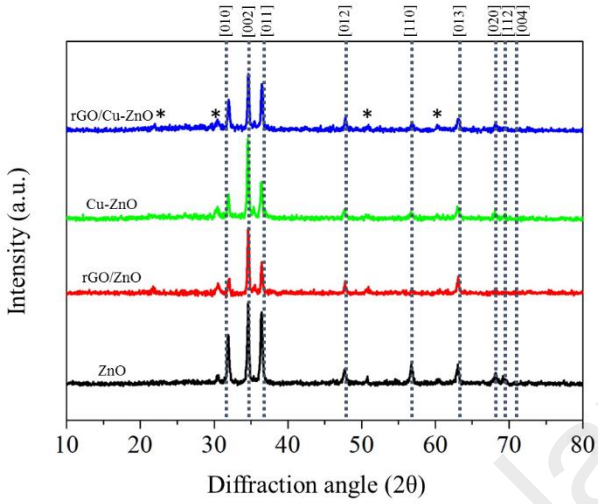

Figure 4.3 XRD diffractograms of the ZnO, rGO/ZnO, Cu-ZnO and rGO/Cu-ZnO thin films.

Raman spectroscopy revealed the structure of the crystal lattice by measuring the changes in frequency of light as a result of interacting with the sample. The Raman spectrum of the unmodified ZnO sample (Figure 4.4a) consisted of peaks at 328, 380, 439, 558 and 1100 cm^{-1} which corresponded to Raman-active phonon modes of wurtzite ZnO nanowires with C_{6v} symmetry (Gaikwad et al., 2014; R. Zhang et al., 2009b). The dominant line at 439 cm^{-1} corresponded to the E_{2H} vibration mode which is a characteristic band of wurtzite-phase ZnO. Other studies on pure ZnO nanomaterials reported peak positions of 432 (Kuriakose et al., 2015) and 433 cm^{-1} (J. Das et al., 2010). The redshift in E_{2H} peak position indicated that the present preparation method introduced tensile strain in the ZnO lattice, which was previously attributed to crystal defects (e.g. zinc interstitials and oxygen defects) (Iqbal et al., 2014).

Figure 4.4b shows the changes in crystal strain in the ZnO crystal structure as a result of Cu-doping and rGO-hybridisation. Cu-doping blueshifted the E_{2H} peak from 439 cm^{-1}

in the ZnO sample to 437 cm^{-1} in Cu-ZnO and rGO/Cu-ZnO samples. rGO-hybridisation resulted in a blueshift to 435 cm^{-1} in the rGO/ZnO sample. Cu has an atomic radius of 1.28 Å whereas Zn has an atomic radius of 1.38 Å, thus Cu is able to be incorporated into the ZnO lattice by substitutional or interstitial doping (Mian Liu et al., 2010b). The compression of the ZnO lattices through Cu-doping causes an increase in phonon interaction, which is the probable reason for the blueshift in E_{2H} peak position (Iqbal et al., 2014).

Carbon-based materials which are rich in sp^2 structure exhibit G, D and 2D peaks, of which the G band is a result of the 6-carbon ring breathing mode. The D band represents a ring breathing mode in the sp^2 carbon rings, but is activated in the presence of defects. The 2D band is the second order of the D band, sometimes referred to as an overtone of the D band (Berciaud et al., 2009). In graphene, the D, G and 2D bands are typically formed at 1350, 1580, and 2700 cm^{-1}. In rGO/ZnO sample, the D peak was observed to blueshift to 1320 cm^{-1}, which indicates an increase in electron doping in the rGO structure. On the other hand, Cu-doping caused the D peak in the rGO/Cu-ZnO sample to redshift to 1405 cm^{-1}. The 2D band was absent in both samples, which suggested that the rGO was highly disordered such that the 2D vibrational transition does not occur. The I_D/I_G ratio of rGO increased from 0.79 to 0.88 in the rGO/ZnO and rGO/Cu-ZnO samples, respectively.

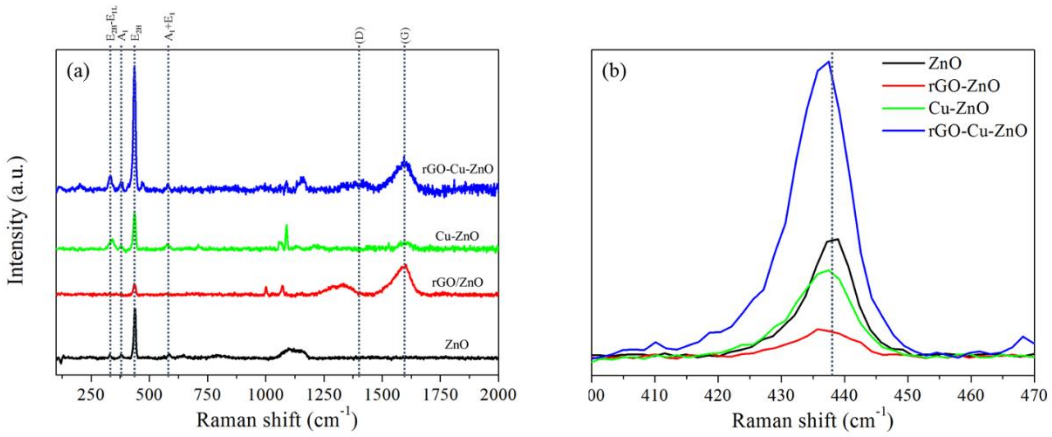

Figure 4.4 (a) Raman spectra of ZnO, rGO/ZnO, Cu-ZnO and rGO/Cu-ZnO, showing rGO (in parenthesis) and ZnO peaks (b) Magnification of E_{2H} peaks

X-ray photoelectron spectroscopy (XPS) was employed to investigate the changes in surface chemistry of ZnO thin films due to the addition of Cu dopant and rGO hybridisation. The XPS spectra of the Zn2p3 orbital for the pure ZnO, Cu-doped ZnO and rGO are demonstrated in Figure 4.5. It can be observed that the Zn2p3 peak in pure ZnO exhibited a characteristic peak position at 1021.7 eV. With the addition of Cu dopant, the peak shifted slightly to a higher binding energy of 1022.0 eV. This indicated that the incorporation of Cu dopant into the thin film structure perturbed the crystal structure, thus resulting in a higher binding energy. The hybridisation of Cu-doped ZnO thin films with rGO appeared to stabilize the wurtzite crystal structure, as observed through the shifting of peak position back to 1021.7 eV, which is the same peak position as pure ZnO prepared *via* the present method.

Several notable observations can be made from the O 1s region of the XPS spectra, regarding the surface composition of the ZnO thin films as a result of Cu doping and rGO hybridisation. The O 1s region of ZnO nanorods can be fitted into two (2) Gaussian peaks as shown in Figure 4.6a, 4.6b and 4.6c for pure ZnO, Cu-ZnO and rGO/Cu-ZnO, respectively. The peak located at 530.2 eV belonged to the Zn–O bonding in ZnO in

nanorod form (Djurišić and Leung, 2006). The peak located at 532.3 eV can be ascribed to Zn-OH bonds (Jeon et al., 2011). In the pure ZnO thin film, the Zn-O bond was observed alongside Zn-OH bond. With the addition of Cu dopant, the peak intensity corresponding to the Zn-OH bond increased, indicating subtle changes in the crystal structure of the thin film's surface. When hybridised with rGO, this improved the chemical composition of the rGO/Cu-ZnO thin film, indicated by the increase in Zn-O peak intensity and reduction in Zn-OH peak intensity.

The Cu 2p peak indicated that the Cu dopant was incorporated into the crystal structure of Cu-ZnO and rGO/Cu-ZnO in the form of Cu_2O (Figure 4.6d). The absence of satellite peaks between 940 to 945 eV and at 963 eV indicated that CuO was not formed in the rGO/Cu-ZnO thin film.

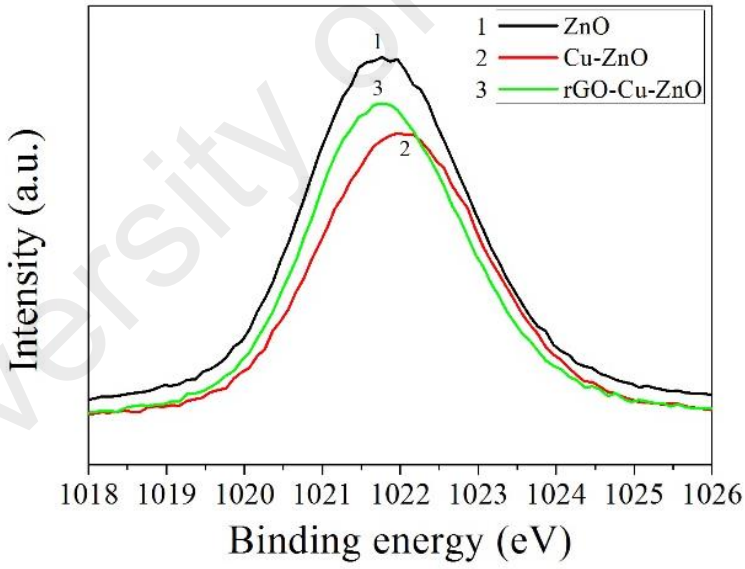

Figure 4.5 XPS spectra of Zn2p3 binding energies from ZnO, Cu-doped ZnO and rGO/Cu-ZnO thin films

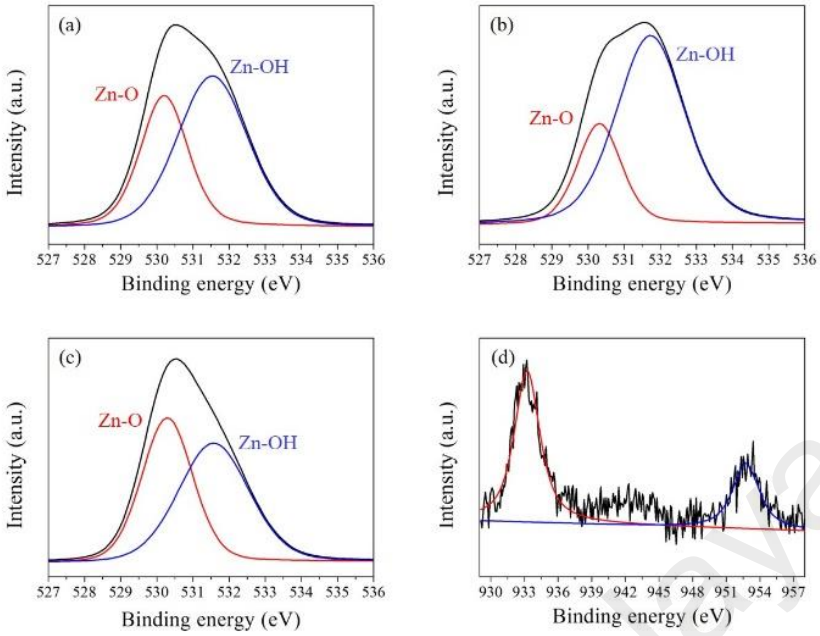

Figure 4.6 XPS spectra of O1s core level emissions for (a) ZnO, (b) Cu-ZnO and (c) rGO/Cu-ZnO. (d) XPS Cu2p spectrum indicating the incorporation of Cu as Cu_2O into the crystal lattice.

4.2.2.2 Optical properties

PL spectroscopy was able to provide information on the type of recombination processes occurring in the ZnO sample, as well as the effect of Cu-doping and rGO-hybridisation towards the rate of recombination in ZnO (Figure 4.7). The PL spectra of ZnO typically consists of two major peaks (Hsieh et al., 2006; G. J. Lee et al., 2010): the band centred at approximately 382 nm is due to photoemissions caused by a band-to-band radiative recombination. The broad band in the visible region is due to defects in the crystal lattice which causes deep-level photoemissions. The type of defect determines the position of the peak in the visible region – for instance, the green PL emission at 525 nm is typically attributed to the electron transition from a singly ionized V_O to a photoexcited hole (Janotti and Van de Walle, 2009; C. Li et al., 2006).

The ZnO film prepared in this study contained a high amount of V_O, evidenced by the intense peak at 525 nm. This indicates that recombination predominantly occurs *via* Shockley-Read-Hall recombination in the ZnO film. In the rGO/ZnO sample, the peak in the visible region diminished but the peak at 382 nm was enhanced, indicating that the predominant recombination pathway was *via* band-to-band radiative recombination. The intense peak at 382 nm for rGO/ZnO may be attributed to an increase in surface area, which is agreeable with a previous study which also reported that increasing recombination is observed with increasing surface area (K. Zhu et al., 2006). In the present study, the morphology of ZnO changed from a vertically-aligned nanorods with consistent diameter of approximately 300 nm and terminated in a flat-top manner, to the formation of non-uniformed rod diameters ranging between 100 to 600 nm, indicating an increase in surface area and hence corresponds with the increase in surface active sites and recombination sites. The doping of ZnO with Cu largely suppresses both the UV-range and green PL emission, The strong depression of the peak intensity at 382 nm indicated that electron-hole recombination *via* radiative emission is largely inhibited, which may be due to quenching processes such as electron transfer or complex formation. A substituting Cu atom in ZnO forming a Cu^{2+} lattice $3d^9$ state creates a deep acceptor level (H. Zhu et al., 2008), and accounts for the redshift of the emission peak in the visible region from 525 to 600 nm. When the Cu-ZnO film was hybridised with rGO, the peak at 382 nm increased. This indicates that the rGO-hybridisation enhanced the band-to-band recombination process.

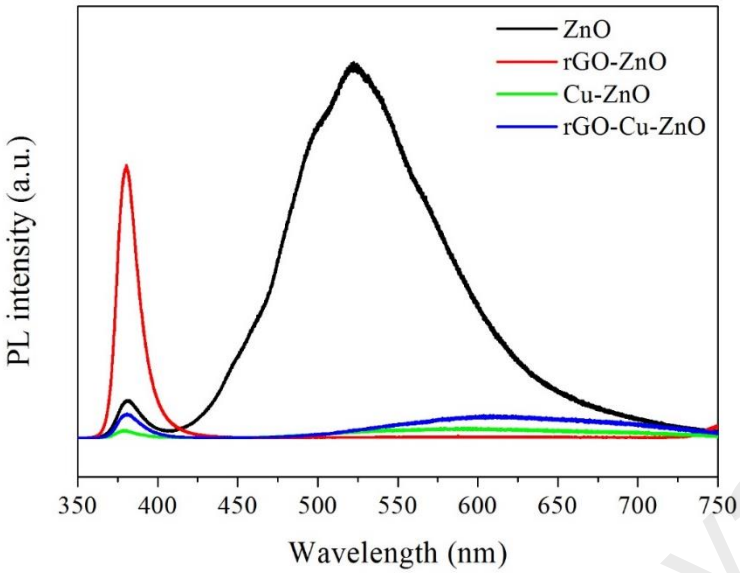

Figure 4.7 PL spectra of ZnO modified with Cu-doping and rGO-hybridisation

The optical properties of the thin films were determined from diffuse reflectance UV-Visible (DR-UV-Vis) spectroscopy in reflectance mode. The reflectance values were then converted to absorbance values using the Kubelka-Munk (K-M) conversion (Figure 4.8). The optical band gap was estimated as the value where the extrapolated slope of the graph intersects the x-axis. In the present method, the pure ZnO thin film possessed an absorption edge beginning at 386 nm. The doping of Cu into ZnO thin films slightly increased the absorption edge to 388 nm, corresponding with the formation of Cu impurity levels (Cu^{2+} lattice $3d^9$ state) below the CB of ZnO (H. Zhu et al., 2008). rGO-hybridisation resulted in greater light absorption compared to Cu-doping, as the absorption edge for rGO/ZnO sample began at 396 nm. However, the combination of Cu-doping and rGO-hybridisation slightly reduced the absorption range, with the absorption edge beginning at 391 nm.

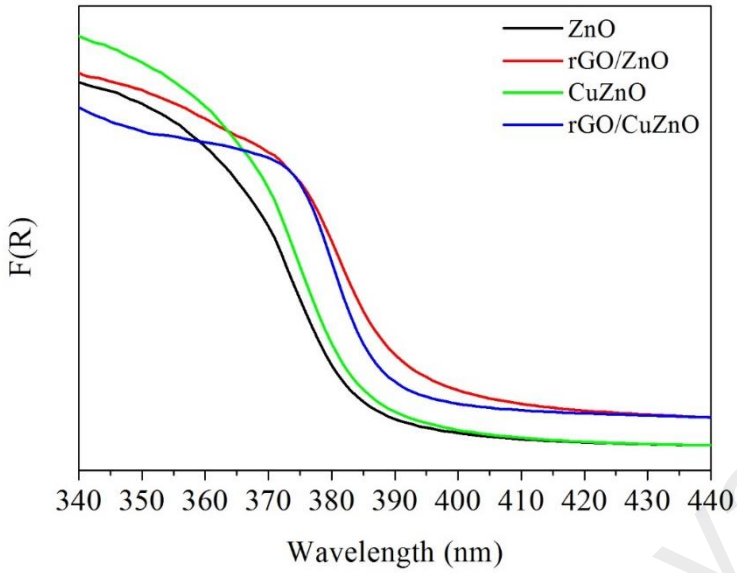

Figure 4.8 K-M absorption of unmodified, Cu-doped and rGO-hybridised ZnO films

UPS was conducted to determine the changes in band gap due to Cu-doping and rGO-hybridisation. The band gap of ZnO was measured at 3.56 eV (Figure 4.9). The film thickness using this method is usually between the range of 1.0 – 1.5 μm, thus it may be unlikely that the band gap broadening was due to quantum confinement effect (Thankalekshmi et al., 2013). Alternatively, the broadening of the band gap may have been due to the Burstein-Moss effect, i.e. this preparation method may have caused the electron carrier concentration to exceed the CB edge density of states. Subsequently, the Fermi level is pushed to a higher energy within the CB and causing the observed band gap broadening (G. H. Lee et al., 2001). rGO-hybridisation resulted in a broadening of the band gap to 3.63 eV for the rGO/ZnO sample. On the contrary, Cu-doping of ZnO reduced the band gap to 3.48 eV which corresponds to the formation of impurity levels within the band gap of ZnO due to Cu doping. The incorporation of rGO resulted in a slight band gap increase to 3.50 eV, although the band gap is still smaller than ZnO.

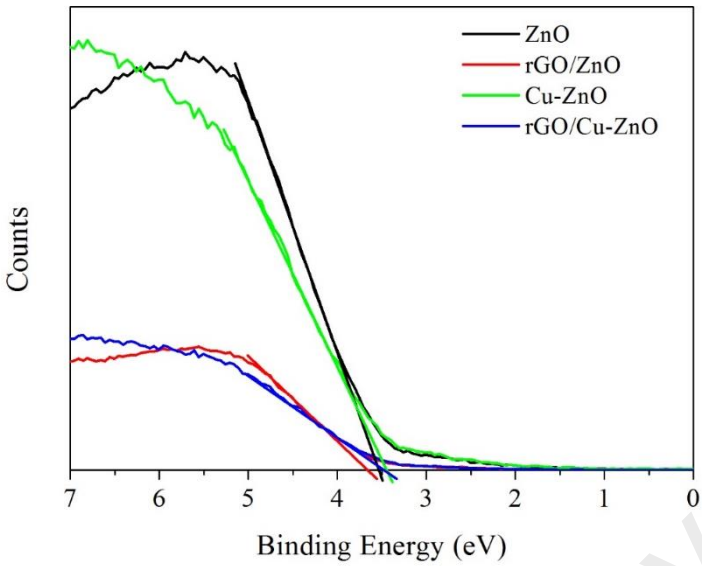

Figure 4.9 UPS spectra of unmodified, Cu-doped and rGO-hybridised ZnO films

4.2.2.3 Electrochemical properties of Cu-doped and rGO-hybridised ZnO films

To evaluate the photo-response of the prepared thin films, the J_p was measured at V_{OC} with chopped illumination (Figure 4.10). At V_{OC}, no current flows through the electrochemical cell. Each sample exhibited rapid photoresponse as indicated by the sharp rise and drop of current in the presence and absence of illumination, respectively. Under dark conditions, all samples exhibited non-significant J_p of less than 1 µA cm^{-2}. However, the J_p increased under illumination. For the unmodified ZnO thin film, a J_p of 0.1 mA cm^{-2} was observed. The rGO/ZnO thin film showed an initial J_p of 0.3 mA cm^{-2} which then increased to 0.45 mA cm^{-2} with prolonged exposure to simulated solar illumination. The increase in J_p when the rGO/ZnO sample was irradiated with simulated solar irradiation corresponds with the photoreduction of rGO in the presence of ZnO. This similar phenomenon was previously attributed to the electron transfer from the photo-excited ZnO nanoparticles into the graphene oxide platelets, thus resulting in the photoreduction of rGO in the presence of ZnO (Akhavan, 2011). The

photoreduction of rGO thus further enhanced the interfacial charge transfer between the ZnO nanorods and the current collector (ITO substrate), with a low back rate of electron transfer and thus a significant improvement of the photocurrent density. ZnO doped with Cu (Cu-ZnO) experienced a decrease of J_p to about 0.05 mA cm^{-2}, which is most likely due to overdoping of Cu in the ZnO lattice. However, rGO-hybridisation was able to enhance the J_p output of the rGO/Cu-ZnO to about 0.27 mA cm^{-2}. The enhanced J_p for samples which received rGO-hybridisation treatment (rGO/ZnO, rGO/Cu-ZnO) could be attributed to the improvement of interfacial charge transfer between the ZnO nanorods and the current collector. Additionally, the photocurrent density of rGO/ZnO sample increased with consecutive on-off cycles.

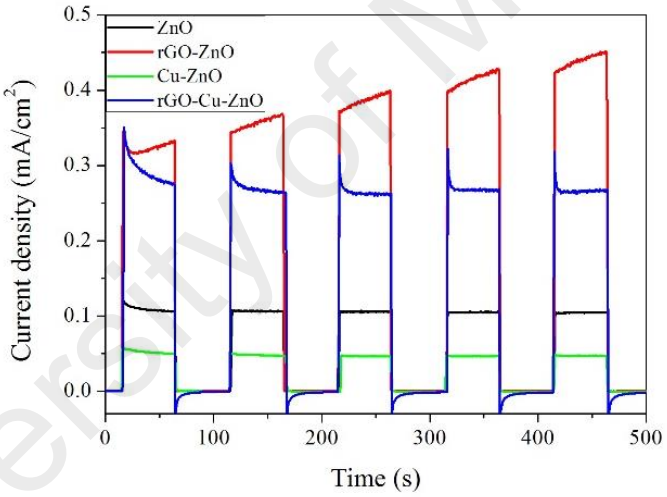

Figure 4.10 Chronoamperometry graphs of ZnO, rGO/ZnO, Cu-ZnO and rGO/Cu-ZnO using chopped illumination in 0.1 M KOH electrolyte

The effect of Cu-doping and rGO-hybridisation on the PEC behaviour of ZnO films was also studied by LSV in the presence or absence of illumination of the samples (Figure 4.11). The J_p of the thin films demonstrated photoresponsivity by an increase in J_p due to simulated solar light irradiation. Dark scan voltammograms between -1.0 to +1.0 V showed a small current in the range of 10^{-7} mA cm^{-2}. Upon illumination with

1.5AM xenon lamp source, the pure ZnO thin film showed a nearly linear increase in the PCD from an onset value of around -0.4 V, in agreement with literature for analogous materials (Hsu et al., 2011; Jeon et al., 2011). The increase of photocurrent discloses the effective charge separation because the recombination of photoinduced electron-hole pairs is inhibited by the increase of positive potential. The rGO/ZnO thin film showed enhanced PCD due to the incorporation of rGO, confirming the efficient charge separation evidenced by reduced emission intensity in PL spectra (Figure 4.7). Cu-ZnO and rGO/Cu-ZnO shows quite a unique behaviour. First, a peak is observed around -0.3 to -0.4 V, related to H_2 desorption, indicating a change in the surface characteristics of ZnO by doping with Cu. The photocurrent steadily rises between -0.3 to +0.7 V. Beyond +0.7 V, voltage breakdown of the thin films are observed i.e. the minimum voltage at which the semiconductor electrodes become electrically conductive. The formation of a hybrid rGO/Cu-ZnO thin film significantly enhanced the photoresponse with a J_p of 1.27 mA cm^{-2} at +0.7 V, compared to 0.23 mA cm^{-2} for Cu-ZnO sample.

The photo-conversion efficiency of the film films were calculated using the ABPE equation using two voltage values i.e. V_{OC} and +0.7 V, as summarised in Table 4.1. The ABPE was calculated at V_{OC} to determine the photo-conversion efficiency of the samples without any external bias. An applied bias of +0.7 V was selected to determine the maximum photo-conversion efficiency of the samples before the samples undergo voltage breakdown. Based on the results in Table 4.1, it can be observed that the rGO/Cu-ZnO sample demonstrated the highest ABPE at 0.31 %. At an applied potential of +0.7 V, the highest ABPE of 0.95 % was observed in rGO/ZnO sample.

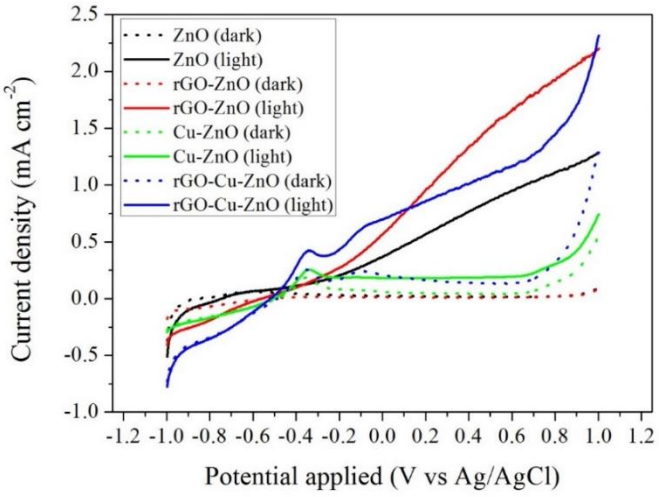

Figure 4.11 Linear sweep voltammograms of ZnO, rGO/ZnO, Cu-ZnO and rGO/Cu-ZnO between -1.0 to +1.0 V under dark and light conditions, at scan rate of 100mV s^{-1} in 0.1 M KOH electrolyte

Table 4.1 Summary of ABPE values for ZnO, rGO/ZnO, Cu-ZnO and rGO/Cu-ZnO at V_{OC} and +0.7 V (P_{tot} = 100 mW cm^{-2})

Sample	Applied potential (V)	J_p (mA cm^{-2})	ABPE (%)	Applied potential (V)	J_p (mA cm^{-2})	ABPE (%)
ZnO	-0.75	0.104	**0.04**	0.7	1.04	**0.55**
rGO/ZnO	-0.56	0.265	**0.17**	0.7	1.8	**0.95**
Cu-ZnO	-0.51	0.049	**0.03**	0.7	0.23	**0.12**
rGO/Cu-ZnO	-0.52	0.449	**0.31**	0.7	1.27	**0.67**

4.2.3 Discussion

In this experiment, the effect of combining Cu-doping and rGO-hybridisation strategies to enhance the photo-conversion efficiency of ZnO were investigated. It was found that the preparation of ZnO *via* electrochemical deposition and annealing under argon gas flow introduces V_O into the crystal lattice as shown by the redshift in Raman spectroscopy analysis i.e. increase in tensile strain in the ZnO lattice. The band gap of ZnO (3.56 eV) prepared in this experiment was larger than the theoretical value of 3.37 eV. The observed band gap broadening was not due to the surface confinement effect,

as no blueshift was observed in the Raman or PL spectrum (K.-F. Lin et al., 2005). Additionally, the XRD analysis indicated the absence of amorphous ZnO which may cause band gap broadening (Tan et al., 2005). Alternatively, the values of band gap are associated with strain in the ZnO crystal lattice. Two types of strain can occur within a ZnO lattice: uniaxial and hydrostatic strain. In a previous study, it was found that the band gap of ZnO increased with increasing compressive uniaxial strain (Yaqin Wang et al., 2015b), as compressive uniaxial strain results in change from direct to indirect band gap behaviour for ZnO. On the other hand, an increasing tensile hydrostatic strain weakens the interactions between Zn and O atoms at either [110] or [001] planes, leading to the broadening of the band gap. As such, the band gap broadening in the ZnO sample was due to tensile, hydrostatic strain.

The Cu-doping technique employed in this experiment did not enhance the photo-conversion efficiency of ZnO, as demonstrated by the poor ABPE values for Cu-ZnO sample. The Raman E_{2H} peak of Cu-ZnO sample experienced blueshift, which indicated an increase in compression in the crystal lattice. Compression can be due to interstitial doping or substitutional doping at Zn sites. A previous study reported that substitutional doping of Cu into the ZnO lattice resulted in a decrease in hole concentration as Cu played the role of electron donor. Whereas, if Cu atoms were incorporated into the ZnO lattice interstitially, they act as acceptor resulting in the increase in hole concentration (Mian Liu et al., 2010b). Based on this information, it is most likely that Cu was incorporated substitutionally into the ZnO crystal lattice as a decrease in hole concentration led to the reduced photoresponse of ZnO. Another issue affecting the photo-conversion efficiency of Cu-ZnO is the possibility of overdoping which can introduce deep-level traps, leading to recombination of photogenerated electron-hole pairs *via* Shockley-Read-Hall recombination mechanism (Shockley and Read, 1952).

The hybridisation of ZnO with rGO was able to enhance the properties of ZnO by decreasing the nanorod diameter (FESEM), reducing hydrostatic strain in ZnO lattice (Raman) as well as reducing contact and charge transfer resistance (chronoamperometry). The improved charge transfer properties as a result of hybridising rGO and ZnO was previously attributed to the formation of C-O-Zn bonds at the rGO-ZnO interface (Lv et al., 2015; Son et al., 2012). Zn^{2+} ions bind with C=O functional groups present in rGO to form a covalent bond. Due to the C-O-Zn bonds, photoexcited electrons are transferred from the CB in ZnO to the π-π molecular orbitals in rGO. The excited state of ZnO is quickly deactivated, thus making it available for new photoelectric events to occur (Son et al., 2012).

Finally, the combination of Cu-doping and rGO-hybridisation resulted in an intermediate ABPE performance of 0.67 %. The hybridisation of Cu-doped ZnO with rGO was able to improve interfacial charge transfer, which effectively competes with the non-radiative decay, and thereby promoting effectively the photoelectrochemical performance of Cu-doped ZnO, as demonstrated by an increase in J output for rGO/Cu-ZnO compared to Cu-ZnO sample.

Therefore, this study highlighted the potential of rGO to further enhance the PEC properties of ZnO. This finding contributes towards reducing our dependence on limited noble metal dopants to improve the semiconductor behaviour of ZnO thin films. Future studies would be important to identify factors to fine-tune the PEC behaviour of rGO-hybridised ZnO, with the aim of enhancing its conductivity and photoanodic performance.

4.3 Effect of electrochemical reduction method on the photo-conversion efficiency of rGO/ZnO photoanode

The development of ZnO hybridised with non-metal promoters such as rGO is a promising, cost-effective strategy to enhance the photo-conversion efficiency of ZnO. The enhancement of ZnO by hybridisation with rGO has been attributed to the formation of heterojunctions (R. Sharma et al., 2014) and a reduction of contact resistance between ZnO and the current collector. In Section 4.1, the photo-conversion efficiency of ZnO was enhanced by hybridisation with rGO. The findings from the study also showed that the amount of oxygen defects within the ZnO crystal lattice were reduced when ZnO was grown on rGO.

The preparation of rGO/ZnO films using the electrochemical deposition method is a two-step process, involving the preparation of electrochemically-reduced GO (ERGO) followed by the electrochemical deposition of ZnO. As GO is an electrically-insulating material (due to its disrupted sp^2 bonding networks), its electrical conductivity can be recovered through the reduction of the oxygen-containing defects on the GO surface, thus restoring the delocalised π-network. GO can be reduced to rGO through thermal, chemical and electrochemical methods. However, the electrochemical reduction method offers a rapid and environmentally-friendly method of restoring the sp^2 network in the GO structure.

The electrochemical reduction of GO is believed to occur when the GO sheets adjacent to a working electrode accept electrons, yielding the insoluble ERGO that attach to the electrode surface (Toh et al., 2014). In a study comparing the properties of rGO prepared using hydrazine vapour reduction vs electrochemical reduction, Wang and co-workers reported that ERGO possessed lower oxygen-containing functional groups (Zhijuan Wang et al., 2012c). In turn, the quality of the ERGO was better

compared to rGO prepared by hydrazine vapour reduction, as indicated by the enhanced dopamine sensing ability.

The electrochemical techniques to prepare ERGO can be classified into two main categories i.e. potentiostatic and potentiodynamic techniques. The potentiostatic technique provides a constant electric field and electrons for the reduction of GO to rGO. The potentiodynamic technique involves the change of potential at a constant rate. In the potentiostatic technique a constant voltage is applied to the working electrode for a fixed duration. The current signal produced during the electrochemical reduction process was measured as a function of time. The potentiodynamic technique is similar to the CV technique, whereby the working electrode potential is ramped linearly beginning with an initial potential up to the final set potential. After the set potential is reached in a CV experiment, the working electrode's potential is ramped in the opposite direction to return to the initial potential. These cycles of ramps in potential may be repeated as many times as desired. The current signal is measured as a function of applied voltage. The independent variables in the potentiodynamic technique are the scan rate and number of cycles. The scan rate refers to the rate at which the potential is ramped, in units of millivolts per second ($mV\ s^{-1}$). Similar to the conversion of GO to rGO *via* chemical reduction whereby the application of various chemicals and processing conditions are able to change the structure of the rGO, it might be expected that the extent of oxygen-containing functional groups reduced in the ERGO structure is dependent on the electrochemical reduction technique.

To the best of my understanding, the effect of electrochemical technique on the quality of the ERGO film has not yet been explored. A deeper understanding on the effect of an electric field towards the conversion of GO to ERGO will allow us to improve the preparation of ERGO. Therefore, the aim of the experiment was to identify

the best electrochemical technique for preparing ERGO films in order to promote the photo-conversion efficiency of ZnO.

4.3.1 Materials and methods

GO was prepared using a modified Hummer's method. $Zn(NO_3)_2 \cdot 6H_2O$ and EDA were obtained from R&M Chemicals (Malaysia), whereas, HNO_3 and ammonium nitrate, NH_4NO_3 was purchased from Merck (USA). Indium-doped tin oxide (ITO)-coated glass with sheet resistance of < 7 Ω sq^{-1} purchased from Magna Value (Malaysia) was used as the conductive substrate for the electrodeposition of rGO-hybridised ZnO thin films.

4.3.1.1 Preparation of electrochemically-reduced GO thin films

The ERGO films were prepared using three variations to the potentiodynamic technique and one potentiostatic technique, as described in Figure 4.12. The three-electrode electrochemical cell used to prepare the ERGO films comprised of a pre-cleaned ITO glass (2 cm x 2.5 cm), platinum wire and Ag/AgCl which functioned as working electrode, counter electrode and reference electrode, respectively. The electrolyte solution consisted of a 7 mg L^{-1} solution of GO dispersed by ultrasonication in HNO_3 (pH 3) solution. An acidic pH of 3 was selected as it was previously reported that ERGO films are strongly soluble in basic electrolyte solutions, whereby the solubility of the ERGO was ascribed to the residual phenolic hydroxyl, carboxylic groups and epoxy groups that exist on the graphene plane (C. Liu et al., 2011). Additionally, an acidic electrolyte was found to facilitate the protonation of GO in the electrochemical reduction process (Zhou et al., 2009). A fresh 30 mL of the electrolyte

solution was used for the preparation of each ERGO film. The electrochemical reduction was carried out at room-temperature (25 °C).

In this experiment, scan rates of 1 mV s^{-1} and 10 mV s^{-1} were selected in order to compare the effects of scan rate (1 mV s^{-1} = slow, 10 mV s^{-1} = fast) towards the reduction of GO. The four samples were assigned labels according to the method of electrochemical reduction, scan rate and number of scan cycles. The first sample involved the electrochemical reduction of GO using potentiodynamic technique by cycling between 0 to -1.1 V at a slow scan rate of 1 mV s^{-1}, for one cycle (Sample CV(1,1), Figure 4.12a). The second ERGO sample was prepared using potentiodynamic technique by cycling between 0 to -1.1 V at a slow scan rate of 1 mV s^{-1}, for five cycles (Sample CV(1,5), Figure 4.12b). Thirdly, ERGO was prepared *via* potentiodynamic technique by cycling between 0 to -1.1 V at a fast scan rate of 10 mV s^{-1}, for fifty cycles (Sample CV(10,50), Figure 4.12c). Finally, a constant potential of -0.9 V was applied for 2 hours to yield the ERGO film prepared by potentiostatic technique (Sample CP, Figure 4.12d). Upon completing the electrochemical reduction, the samples were rinsed with deionized H_2O and allowed to air-dry. The dried samples were kept in a petri dish sealed with Parafilm M® film until further use.

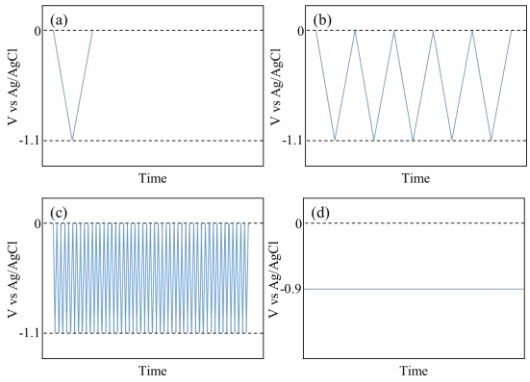

Figure 4.12 Voltage-time graphs illustrating the electrochemical technique used for preparing ERGO samples CV(1,1) (a), CV(1,5) (b), CV(10,50) (c) and CP (d)

4.3.1.2 Preparation of rGO/ZnO thin films

The ZnO film was then grown on the ERGO films using the three-electrode electrochemical cell setup described in Section 4.2.1.1. 50 mL electrolyte solutions containing 0.1 M $Zn(NO_3)_2 \cdot 6H_2O$, 0.1 M NH_4NO_3 and 0.01 EDA were used as zinc precursor, supporting electrolyte and structure directing agent, respectively. This was achieved by dissolving 1.487 g of $Zn(NO_3)_2 \cdot 6H_2O$, 0.400 g of NH_4NO_3 and 5.0 mL of 0.5 M EDA solution to 50 ml with deionized H_2O to produce a cloudy solution. This solution was immediately used, and a fresh solution was prepared for the deposition of each rGO/ZnO film. The rGO/ZnO thin films were prepared using ERGO-coated ITO glass as the working electrode, and immersed into the electrolyte solution. A constant voltage of -0.9 V was applied for 15 minutes. The temperature of the electrodeposition cell was maintained at 60 °C using a H_2O bath. All thin film samples were carefully rinsed with deionized H_2O so as not to damage the thin film coating by mechanical abrasion and allowed to air-dry in a desiccator before annealing. A calcination step was performed at 300 °C for 2 hours in argon gas flow, in order to improve the crystallinity of the ZnO film by converting $Zn(OH)_2$ to ZnO (Noack and Eychmüller, 2002).

4.3.1.3 Materials characterisation

FESEM analysis was carried out using a SUPRA^{TM} 35 VP Field Emission Scanning Electron Microscope (Carl Zeiss, Germany) at an accelerating voltage of 5 kV under high-vacuum conditions. The crystal phase of the rGO/ZnO films were characterized using a model D8 ADVANCE X-ray diffractometer (Bruker, Germany) equipped with Cu Kα radiation (λ = 1.5418 Å) at 40 kV and 30 mA. All the patterns were recorded in the 5–90° range, with a step size of 0.02°. The phase identification of the samples were

performed with HighScore Plus software and using reference patterns from the Crystallography Open Database (COD) (Gražulis et al., 2012).

The PEC characterisation of the rGO/ZnO films were carried out in an aqueous 0.1 M KOH electrolyte solution (pH 11), employing a three-electrode electrochemical cell connected to a potentiostat/galvanostat (Autolab PGSTAT302N potentiostat/ galvanostat, Metrohm, Netherlands). The rGO/ZnO film, a platinum wire and an Ag/AgCl (3 M) were used as the working electrode, counter electrode and reference electrode, respectively. Simulated solar light comprising a spectrum range of 200-2500 nm was irradiated on the samples using a 150 W Xe lamp (Model LSP-X150, Zolix, China). The intensity of the light was maintained at 100 mW cm^{-2} by maintaining a constant input current of 8.34 A, as well as maintaining a constant distance between the light source and the PEC water-splitting cell.

LSV analysis was performed in the dark and under simulated solar light irradiation, and was recorded in the anodic direction, in the range of -1.0 V to +1.0 V. Chronoamperometry (*I–t*) measurements were performed in two modes, the first at 0.0 V vs. Ag/AgCl over continuous light on–off cycles. The second chronoamperometry measurement was carried out at +1.23 V vs. Ag/AgCl under constant light illumination. EIS measurements were conducted in the 100 mHz to 1 MHz frequency range, with an amplitude of 10 mV at 0.0 V.

4.3.2 Data analysis

Section 4.2.2.1 presents data on the effects of charge carrier dynamics on the electrochemical reduction of GO. The physical and electrochemical properties of the rGO/ZnO thin films are analysed in Section 4.2.2.2 and Section 4.2.2.3, respectively.

4.3.2.1 Effect of potentiometric method on electrochemical reduction of GO

The diffusion layer in an electrochemical system is defined as "the region in the vicinity of an electrode where the concentrations are different from their value in the bulk solution." (IUPAC, 1997a). "Energy flux density" is defined as the energy traversing in a time interval over a small area perpendicular to the direction of the energy flow, divided by that time interval and by that area – flux is a function of time and area (IUPAC, 1997b).

For the preparation of CV(1,1) sample, a large diffusion layer is formed as the potential was increased from 0.0 V to -1.1 V, as a slow scan rate allowed more time for equilibration between increments in applied bias (Figure 4.13a). The maximum flux created was low and correlated with low current flowing through the electrochemical system. A broad shoulder between -0.6V to -0.9 V was observed on the cathodic sweep, indicating the reduction of GO to ERGO. As the potential cycles back towards 0 V, the electric field in the electrolyte dissipates and allows for mass transport to occur, restoring GO concentrations within the electrolyte. As the potential sweeps back from -1.1 V to 0.0 V (anodic sweep), a peak at -0.85 V is observed. The structure of the anodic peak suggested that the ERGO formed possesses capacitive properties, that the electrochemical reduction is a partially reversible reaction but favourable in the cathodic direction. During the preparation of sample CV(1,5), the maximum current decreased with successive scan cycles, indicating that the supporting electrolyte was being consumed during each cycle (Figure 4.13b).

In the potentiodynamic method of preparing ERGO utilizing a fast scan rate (Sample CV(10,50)), a broad shoulder between -0.6V to -1.0 V was observed on the cathodic sweep, indicating the reduction of GO to ERGO. Figure 4.13c indicated that the

cathodic reduction peak became increasingly developed from 10, 20, 30, 40 to 50 cycles. Anodic peaks were not observed in the complete CV cycle, as shown in the inset of Figure 4.13c. The absence of anodic peaks suggests that the anodic reaction is suppressed when a fast scan rate is employed.

In an electrochemical reduction setup using potentiostatic technique, a constant flux and electric field is set up throughout the process. The chronoamperometric curve recording the change in current as a function of time is shown in Figure 4.13d. In the initial phase, there is a sharp decrease in current, from -0.21 to -0.14 mA cm^{-2} which corresponds to the formation of a diffusion layer within the electrolyte solution. The current steadily increased within the first 30 minutes, followed by a steady-current state whereby a current range of -0.16 to -0.18 mA cm^{-2} was maintained from 30 minutes onwards. Nonetheless, the observed current was lower compared to the observed current in CV mode. As the surface of GO contains oxygen-containing functional groups, the GO particles are generally negatively-charged at its surface (Park and Ruoff, 2009). Thus a prolonged exposure of the constant electric field resulted in reduced flux of reactants towards the working electrode, as GO gradually diffused towards the positively-charged counter electrode.

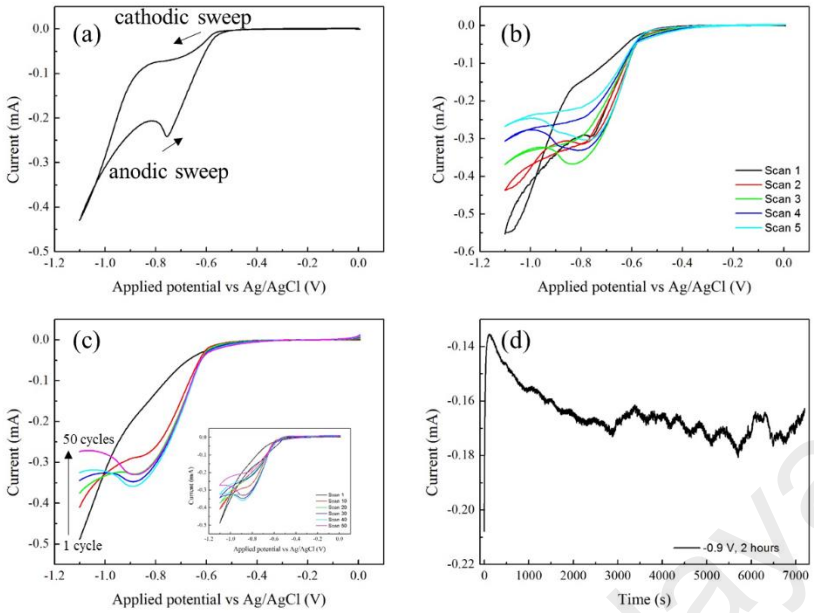

Figure 4.13 Cyclic voltammograms of rGO deposited under scan rates of (a) 1 mV s^{-1}, 1 cycle (b) 1 mV s^{-1}, 5 cycles and (c) 10 mV s^{-1}, 50 cycles. (d) Chronoamperometry curve of the electrochemical reduction of rGO using constant potential technique, using HNO_3 (pH 3) solution

4.3.2.2 Physical properties of rGO/ZnO films

The ERGO films were dark brown colour in appearance and nearly transparent, which indicated that ERGO was successfully deposited on ITO substrate. Photographs of the rGO-coated ITO glass and corresponding rGO/ZnO thin films are presented in Figure 4.14.

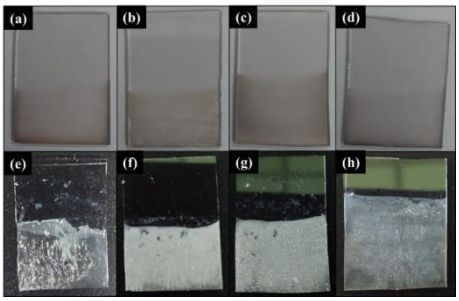

Figure 4.14 Photographs of ERGO films deposited under acidic conditions (a) CV(1,1), (b) CV(1,5), (c) CV(10,50) and (d) CP ERGO films. Images (e) to (h) represent the corresponding rGO/ZnO thin film.

Figure 4.15 shows the morphology of the ZnO nanorods grown on ERGO-coated ITO conductive substrate. The FESEM images show that the method of rGO reduction and deposition affected the coverage and morphology of ZnO films grown on ERGO film. Additionally, the ZnO nanorods featured a porous structure, compared to the formation of a dense structure in the previous experiment (Figure 4.2). The change in morphology can be attributed to the change in the supporting electrolyte used in the electrolyte solution i.e. KCl was used in section 4.2 whereas NH_4NH_3 was used in the present section. The change in supporting electrolyte was made due to concerns of the Cl^- ion acting as hole-scavenger on the photocatalytic activity of ZnO. The formation of porous structures is proposed to occur similar to the Dynamic H_2 Bubble Template method, which was recently reported by Plowman and co-workers (Plowman et al., 2015) to produce porous Cu thin films *via* electrochemical deposition. Briefly, the presence of ammonium ions in the electrolyte induce the formation of H_2 at the surface of the working electrode. Bubbles are insulating and so their presence will reduce the effective surface area through a surface blocking effect and affect the area available for crystal growth. The FESEM images suggests that the method of rGO deposition affects the porosity of the grown ZnO nanorods which increased from samples CV(10,50) < CV(1,5) < CV(1,1) < CP.

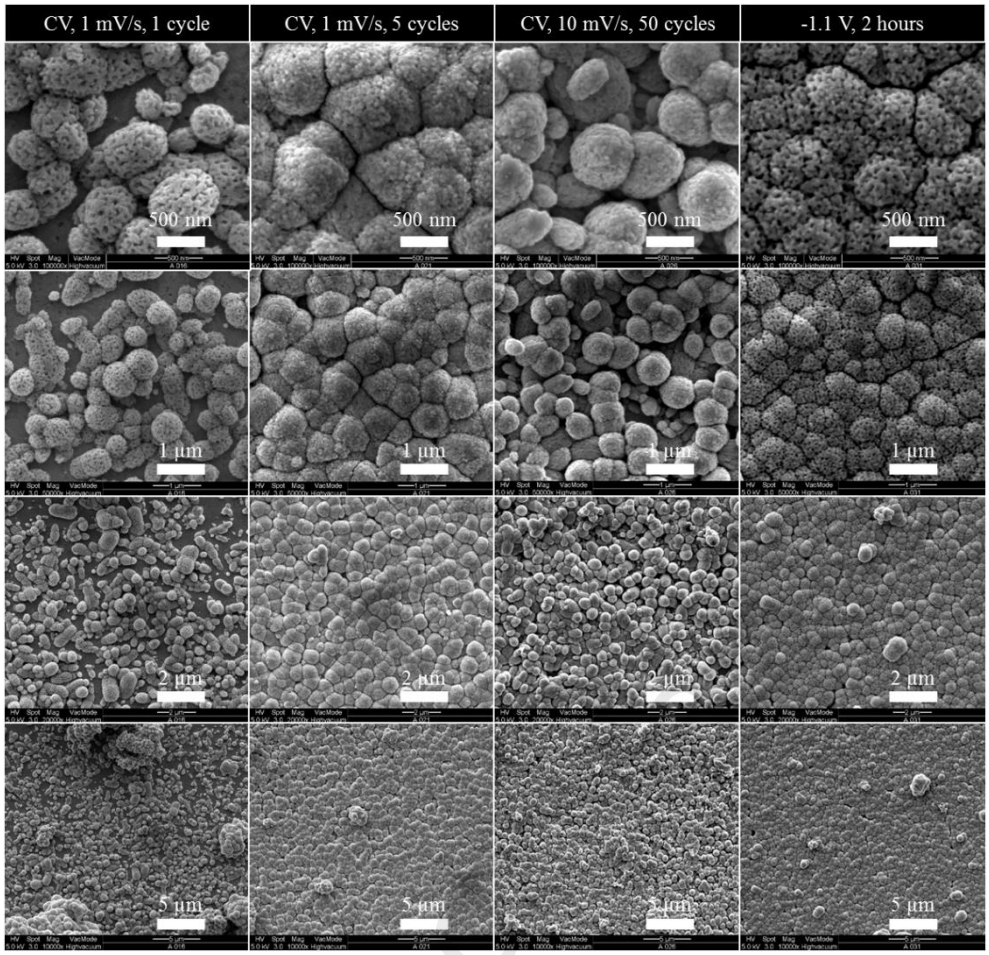

Figure 4.15 FESEM images of ZnO deposited on ERGO films

To illustrate the effect of EDA concentration towards the electrodeposition of ZnO, CV curves were obtained using electrolyte with concentration of 0.1 M $Zn(NO_3)_2 \cdot 6H_2O$ and 0.1 M NH_4NO_3, and varying the concentration of EDA at 0.01 and 0.05 M (Figure 4.16). An oxidation peak at -0.9 V was observed in both solutions containing 0.01 M and 0.05 M EDA. No reduction peak was observed in the cathodic sweep of the CV curve, indicating that the formation of $Zn(OH)_2$ *via* electrochemical deposition was an irreversible process.

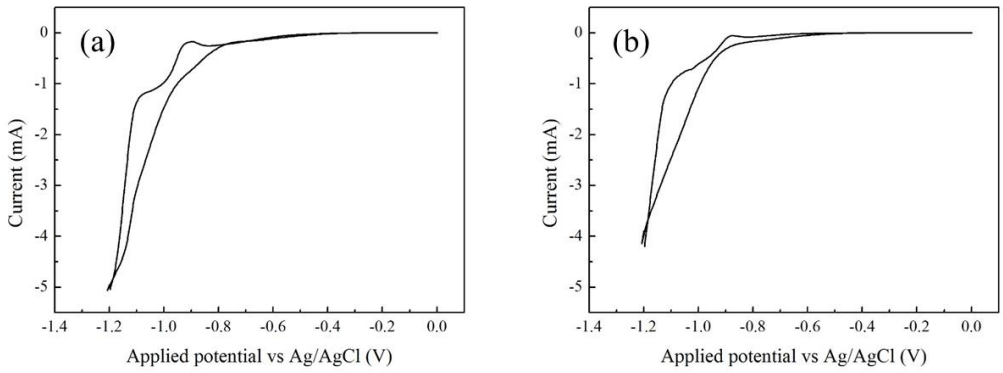

Figure 4.16 CV curve of ZnO electrodeposition using (a) 0.01 M EDA (pH 6.3) and (b) 0.05 M EDA (pH 6.8). An oxidation peak is observed between -0.90 to -0.95 V, which corresponds to the formation of zinc hydroxide, $Zn(OH)_2$.

Chronoamperometry curves were also recorded by applying a potential of -1.0 V for 1800 seconds, at a temperature of 50 °C in order to investigate the effect of EDA concentration on the growth of ZnO films. A temperature above 34 °C is necessary to increase the rate of dehydrating $Zn(OH)_2$ to ZnO, as hydroxide formation is kinetically favoured at low temperature (Marrani et al., 2014). The formation of ZnO at temperatures between 34 and 60 °C could be due to the initial formation of a hydroxide layer, which would slowly dehydrate and forms a seed layer which in turn accelerates the growth of the ZnO film (Goux et al., 2005). For the electrochemical deposition of ZnO using 0.01 M EDA (black line, Figure 4.17), a steady increase in current was observed between 0 to approximately 1200 seconds (20 minutes). The steady increase in current corresponds to the nucleation and formation of $Zn(OH)_2$ seed layer. $Zn(OH)_2$ is slowly dehydrated in-situ to form polycrystalline ZnO islands on the ITO glass surface (Pullini et al., 2011; Skompska and Zarębska, 2014). However, a dramatic increase in the current from 1200 to 1800 seconds indicates a runaway reaction which corresponded to the formation of an overgrowth layer as a result of electrochemical deposition for 30 minutes in the previous experiment (Figure 4.2).

On the other hand, the electrochemical reduction of ZnO using 0.05 M EDA was able to control the growth of ZnO, without any appearance of runaway reaction during the electrochemical deposition process (red line, Figure 4.17). A gradual increase in current was observed between 0 to 700 seconds corresponding to the nucleation and formation of $Zn(OH)_2$ layer. From 700 seconds onwards, the current levels off and a steady current was maintained until the end of the experiment (1800 seconds). The observed plateau in current indicated that nucleation and formation of seed layer was complete, and that the growth of ZnO nanorods proceeded in a consistent manner.

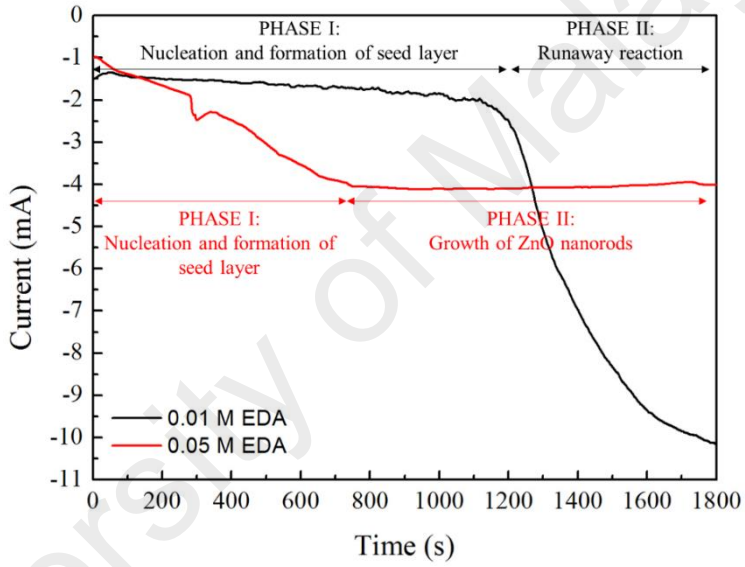

Figure 4.17 Chronoamperometric curves of ZnO electrodeposition at -1.0 V, 50 °C using 0.01 M EDA (pH 6.3) and 0.05 M EDA (pH 6.8) as structure directing agents.

The chronoamperometry curves obtained during the electrochemical deposition of ZnO on the ERGO films revealed changes in nucleation and ZnO crystal growth rate as a result of different ERGO preparation methods. Samples CV(1,1) and CP featured a prolonged nucleation phase as shown by the gradual increase in current between 0 to 800 seconds (Figure 4.18). On the other hand, samples CV(1,5) and CV(10,50) demonstrated an accelerated nucleation phase i.e. within 200 seconds from beginning of

the electrodeposition process. This suggests that the samples CV(1,5) and CV(10,50) were reduced to a greater extent compared to CV(1,1) and CP, hence less time was required for nucleation and the ERGO's conductivity contributed towards the increased current density during the electrochemical reduction process.

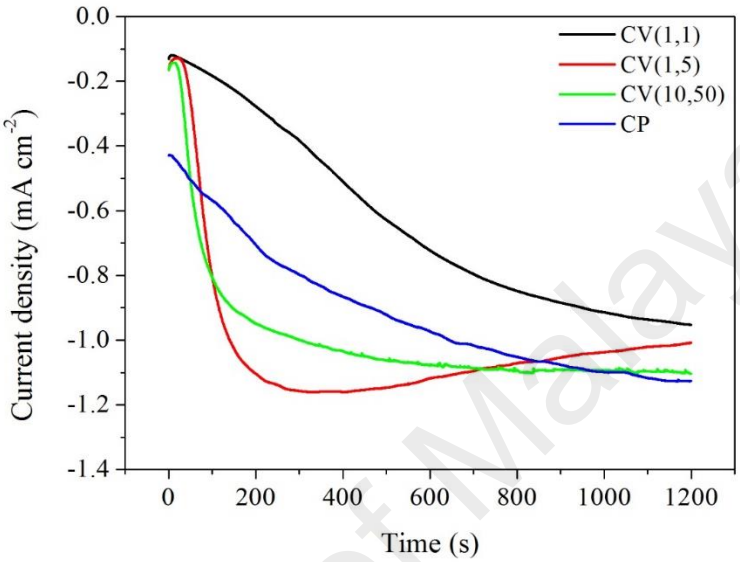

Figure 4.18 Chronoamperometry curves of ZnO electrodeposition

The effect of the ERGO preparation methods towards the growth of ZnO films can be observed from XRD analysis. All samples showed the characteristic peaks of wurtzite ZnO crystal (COD Reference Pattern: 96-101-1259), as shown in Figure 4.19. There were distinct differences in the ZnO growth orientation when grown on ERGO prepared *via* potentiostatic and potentiodynamic method. The [002] peak was dominant in the ZnO film grown on the CP ERGO film sample, which indicated that vertically-aligned nanorods were formed in this sample. On the other hand, ZnO grown on ERGO films prepared by the potentiodynamic method revealed preferential growth in the [101] direction. Specifically, the [101] peak was the most intense in the diffraction patterns of ZnO grown on CV(1,1) and CV(1,5) ERGO films. On the other hand, the ZnO film

grown on CV-deposited ERGO using fast scan rate (sample CV(10,50)) showed an increasingly dominant [002] peak. Based on the XRD results, it can be observed that the preparation of rGO coating by potentiodynamic and potentiostatic methods was able to change the growth orientation of ZnO thin film.

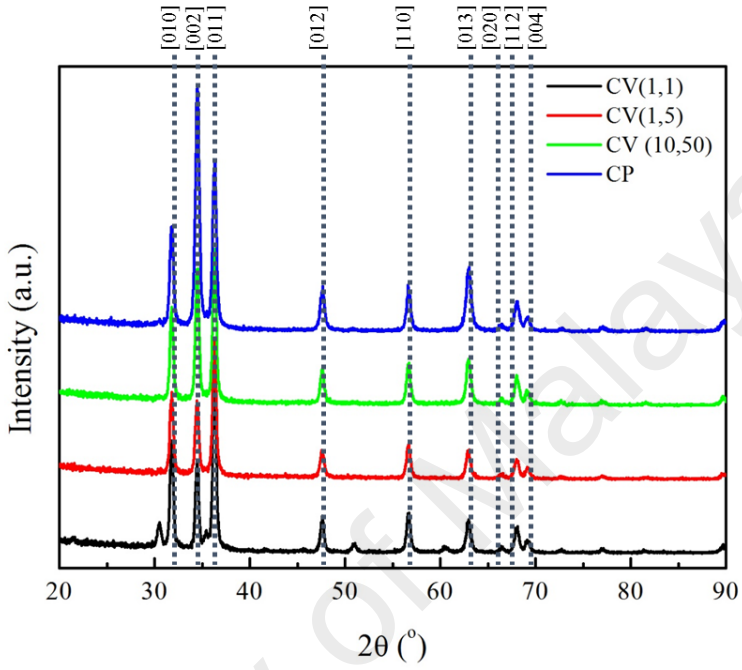

Figure 4.19 XRD peaks of ZnO grown on ERGO thin films prepared using (a) CV, 1 mV s^{-1}, 1 cycle, (b) CV, 1 mV s^{-1}, 5 cycles, (c) CV, 10 mV s^{-1}, 50 cycles, and (d) constant potential, -0.9 V, 2 hours.

4.3.2.3 Electrochemical properties of rGO/ZnO films

EIS is able to provide information on the charge transfer properties of an electrode material by measuring the dielectric properties of a material as a function of frequency (Lopes et al., 2010). From Figure 4.20, it can be observed that the hybridisation of ZnO with ERGO reduced the intrinsic charge transfer resistance of ZnO. The charge transfer resistance decreased from rGO/ZnO samples prepared using CV(1,5) > CP > CV(1,1) > CV(10,50) films. The rGO/ZnO sample prepared with CV(10,50) ERGO film was observed to possess the lowest charge transfer resistance, which is agreeable with the

observation that the enhanced conductivity of ERGO accelerated the rate of nucleation during the electrochemical deposition of ZnO (Figure 4.18). The reduction of charge transfer resistance due to rGO-hybridisation is often reported (L. Sun et al., 2016), and is attributed to the improved contact between ZnO nanoparticles and conductive substrate. The present observation further indicated that the ERGO film prepared using a fast scan rate+multiple cycles technique resulted in greater reduction of the oxygen-containing functional groups on the surface of GO.

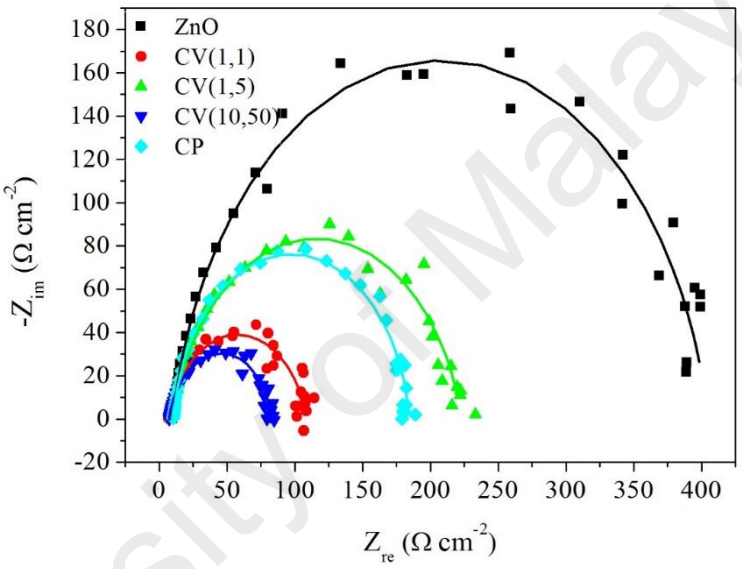

Figure 4.20 Nyquist plots of rGO/ZnO samples prepared using CV(1,1), CV(1,5), CV(10,50) and CP ERGO films, indicating the variance in charge transfer resistance due to the conductive property of ERGO.

The LSV analytical technique is able to provide information on the PEC behaviour of the rGO/ZnO films, as a result of varying the technique of preparing ERGO films. Based on Figure 4.21, no appreciable current was observed in dark conditions i.e. no electrolysis reactions were observed at potentials below +0.8 V vs Ag/AgCl. As expected, ZnO demonstrated photocatalytic activity as shown by the increase in current density when illuminated with simulated solar irradiation. The hybridisation of ZnO with ERGO was able to increase the polarizability of the electrode films, as indicated by

the increase of current density of the rGO/ZnO films in comparison with ZnO. The current density of rGO/ZnO films measured at +1.0 V was observed to increase from ZnO < CV(1,5) < CP < CV(1,1) < CV(10,50) with values of 0.456, 0.561, 0.709, 0.899 and 1.042 mA cm^{-2}, respectively.

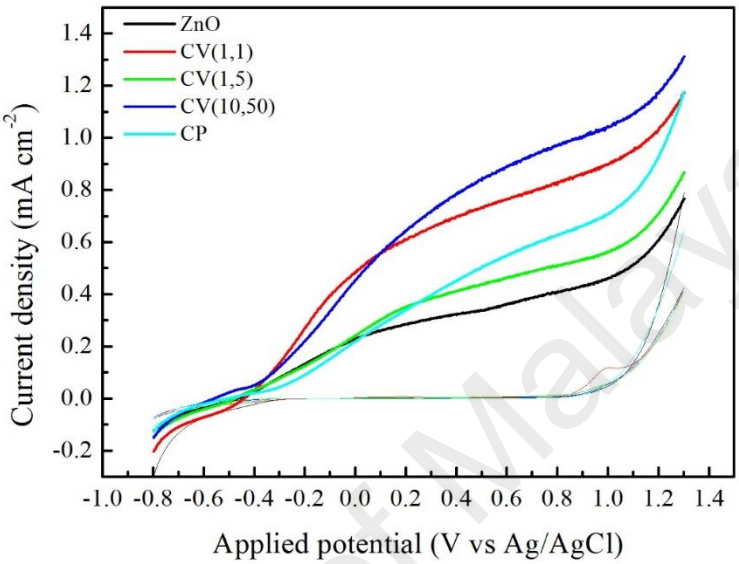

Figure 4.21 LSV curves of rGO/ZnO films prepared using potentiodynamic and potentiostatic techniques. The fine lines indicate current density under dark conditions, whereas the thick lines represent the current response as a result of exposure to 1.5 AM simulated solar irradiation.

The photocurrent response of ZnO and rGO/ZnO films were observed by measuring the current density flowing through the electrochemical cell at 0.0 V (J_{sc}), during which the photoanode was exposed to on/off cycles of simulated solar irradiation. The current measured at 0.0 V represents the current generated due to the collection of electrons generated from the photoexcitation process. The short-circuit current is also an indicator of the maximum photocurrent which may be drawn from the photoanode. Based on the chronoamperometry results shown in Figure 4.22, the J_{sc} of ZnO was 0.244 mA cm^{-2}, and increased from CP < CV(1,5) < CV(10,50) < CV(1,1) with J_{sc} values of 0.321, 0.436, 0.687 and 0.728 mA cm^{-2}, respectively.

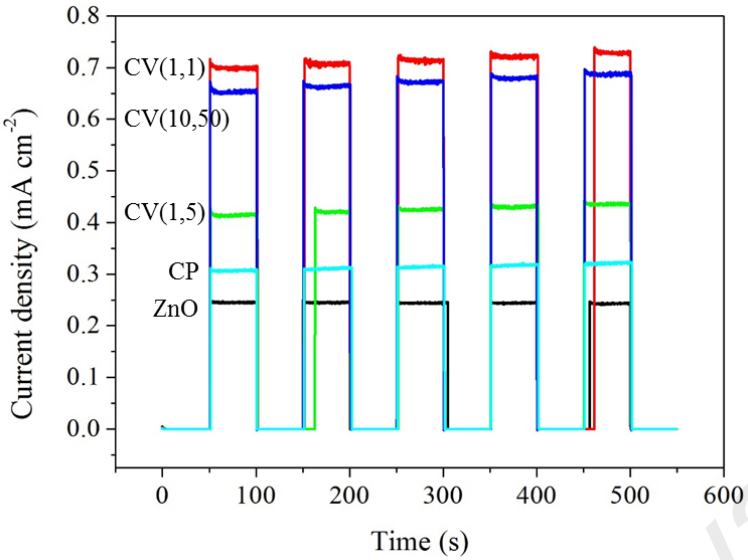

Figure 4.22 Photocurrent response, J_{SC} of ZnO and rGO/ZnO films at short-circuit potential (0 V)

The ABPE values of rGO/ZnO samples are summarised in Table 4.2, whereby it can be observed that rGO/ZnO prepared using CP and CV(1,5) films produced comparable ABPE performance to ZnO modified with Ag co-catalyst (0.40 %) (Y. Wei et al., 2012), Au photosensitiser (0.34 %) (T. Wang et al., 2015a) and formation of TiO_2 heterojunction (0.49 %) (Mingzhao Liu et al., 2013a). Remarkably, the rGO/ZnO films prepared with CV(10,50) and CV(1,1) films exhibited an unprecedented ABPE of 0.84 and 0.89 %, respectively, comparable with Ag-doped $BaTiO_3$ (0.91 %) (Solanki et al., 2013) and SnO_2/TiO_2 films (1.02 %) (Xiaodong Li et al., 2014).

Table 4.2 Summary of electrochemical properties of rGO/ZnO thin films

Sample	V_{oc} (dark)	V_{oc} (light)	J_{sc} (mA cm^{-2})	J_{1V}, LSV (mA cm^{-2})	ABPE (%)
ZnO	-0.11	-0.46	0.24	0.45	0.30
CV(1,1)	-0.08	-0.44	0.73	0.90	0.89
CV(1,5)	-0.11	-0.47	0.44	0.56	0.53
CV(10,50)	-0.24	-0.56	0.69	1.04	0.84
CP	-0.23	-0.50	0.32	0.71	0.39

4.3.3 Discussion

In this experiment, the effect of ERGO preparation technique towards the photocurrent efficiency of rGO/ZnO hybrid films was investigated. Potentiodynamic and potentiostatic techniques were applied in the preparation of ERGO films in order to control between diffusion-limited and rate-limited reaction conditions. The application of diffusion-limited and rate-limited reaction conditions affected the properties of the ERGO film, which in turn affected the morphology, charge transfer resistance and catalytic behaviour of the rGO/ZnO samples.

The FESEM images indicated that the method of preparing ERGO film influenced the morphology of the electrodeposited ZnO film. The appearance of porous ZnO films suggested that the formation of ZnO proceeded *via* H_2-bubble templated electrodeposition as per a recent study on the formation of porous Cu films (Plowman et al., 2015). The authors describe the use of electrolyte solutions containing NH_4Cl to generate H_2 gas bubbles off the surface of the electrode (Ito et al., 1980). The presence of electrode/electrolyte/gas phase was proposed to cause heterogeneous nucleation of metal on the electrode surface. The porous structure was thus formed due to the electrodeposition of the metal at the bubble-electrolyte interface. In the present experiment, NH_4NO_3 was used as supporting electrolyte for in the electrodeposition of ZnO, which, according the H_2-bubble templated electrodeposition method, resulted in the formation of porous ZnO structures as a result of ZnO growth around the H_2 bubbles. The nucleation and growth phases of ZnO observed in Figure 4.18 were also affected by the method used to prepare the ERGO films. The duration of the nucleation phase may be attributed to the quality of the ERGO film as a result of controlling between diffusion-limited and rate-limited conditions.

The J_{SC} properties of ZnO were enhanced due to hybridisation with ERGO, this effect can be attributed to the reduction of charge transfer resistance within the film. EIS analysis showed that rGO/ZnO film prepared by deposition of ZnO on CV(10,50) and CV(1,1) ERGO film were able to produce comparable charge transfer resistance properties. However, an increase in charge transfer resistance as a result of preparing ERGO using repeated slow scan cycles i.e. sample CV(1,5), suggested that multiple scan cycles under diffusion-controlled conditions were not beneficial in the ERGO preparation process. The maximum photovoltage achievable has been found to be dependent on the work function of the Schottky-barrier formed at the metal-semiconductor interface (Thimsen et al., 2011), which corresponds to the observation that the short-circuit photocurrent output was directly related to its charge transfer resistance at the semi-metallic ERGO-ZnO interface. The experiment revealed that ZnO deposited on fast scan CV-deposited rGO (10 mV s^{-1}, 50 cycles) produced the highest PCD of 1.042 mA cm^{-2} at +1.0 V vs Ag/AgCl.

ERGO was also observed to play an electrocatalytic role by improving the photostability of ZnO. rGO/ZnO films were observed to possess onset potentials at more negative potentials compared to unmodified ZnO (LSV analysis, Figure 4.21), which suggested that ERGO provided a lower overpotential for the oxygen evolution reaction (OER) (Warren and Thimsen, 2012).

In summary, this experiment revealed that the properties of ERGO films were changed as a result of modifying the electrochemical reduction technique, which directly influenced the formation and properties of rGO/ZnO films. The preparation of ERGO films was found to affect two parameters in the rGO/ZnO films: (1) photoresponse and (2) photostability of the thin films. The photoresponse of ZnO increased with hybridisation of ERGO due to efficient charge collection from

photogeneration sites. The quality of the ERGO film also affected the V_{OC} value, which in turn improved the PEC property of ZnO. The strategies to improve the quantum yield of photoinduced electron-transfer processes include increasing the discharge rate of photogenerated electrons across the interface and providing a redox pathway with low overpotential (Kamat, 2012). Thus, the findings from this experiment supports the role of ERGO as a promising electron transfer agent, through its ability to enhance charge transfer across interfaces as well as improving the photostability of ZnO. One limitation of this experiment was that the surface properties of the ERGO films were not examined using analytical tools such as XPS. Therefore, further study needs to be carried out on the changes in surface properties of each ERGO film as a result of controlling between diffusion-limited and rate-limited conditions.

CHAPTER 5: NANOSTRUCTURED CARBON AS PHOTOCATALYTIC PROMOTER AT THE ELECTRODE-ELECTROLYTE INTERFACE

5.1 Introduction

The surface interaction between electrode and electrolyte is an important factor affecting the adsorption of redox species, charge transfer and recombination rate of electron-hole pairs in semiconductor photocatalysts. Thus far, research conducted on amorphous silicon carbide (a-SiC) and tungsten oxide, WO have been able to reach photocurrents of > 4 mA cm^{-2} and durability of > 200 hours (N. Gaillard et al., 2010; Matulionis et al., 2010), by enhancing the optical and film surface properties. Most recently, $CuInGaS_2$ photoelectrodes have been able to produce a short-circuit current of 15 mA cm^{-2}, and research is underway to enhance its properties further by passivating surface defects and developing alternative buffer layers (Nicolas Gaillard, 2015). Thus, the enhancement of surface properties remains one of the key strategies to improve the photo-conversion efficiency of ZnO.

Surface defects such as oxygen or metal vacancies, formed during the synthesis of ZnO nanoparticles, are potential sites for the recombination of photoexcited electron-hole pairs. The recombination effect limits the availability of photogenerated holes to react with H_2O to produce O_2. As with other solid materials, the structure on the surface of ZnO crystal is different to its bulk structure. In the bulk crystal, the wurtzite structure of ZnO is maintained, but at the surface of the crystal, the ZnO crystal terminates with –OH and V_o groups (X. Q. Wei et al., 2007). These "dangling bonds" at the surface of ZnO (and other semiconductor materials) interfere with the OER at ZnO photoanodes.

The application of graphene and rGO was found to enhance the surface properties of semiconductors by inhibiting photocorrosion and suppressing recombination of

electron-hole pairs. Monolayer graphene was previously recommended as an ultimate chemical passivation layer for metal surfaces by protecting the underlying metal surface against reaction with ambient gases (Sutter et al., 2010). Subsequent studies support this argument, for instance, a coating of graphene inhibited the corrosion of Cu and Cu/Ni alloy (S. Chen et al., 2011). The chemical stability of Ag nanowire photoelectrodes was enhanced by an rGO coating which acted as a gas-barrier (Ahn et al., 2012). Additionally, the authors reported that the rGO layer was sufficiently thin such that the photovoltaic behaviour was same as that of uncoated Ag nanowire thin film. Graphene was also reported as the thinnest known corrosion-protecting coating, whereby Cu coated with graphene experience a corrosion rate 7 times slower in an aerated Na_2SO_4 solution as compared to the corrosion rate of bare copper (Prasai et al., 2012).

The enhancement of Cu_xO photocatalytic activity by GO was attributed to the negative fixed charge of GO which suppressed the recombination of minority electrons at the surface (Chang et al., 2015). In another study, ZnO/rGO quantum dots were reported to enhance the extraction and transfer of charge carriers in perovskite solar cells (Tavakoli et al., 2016). Graphene and its derivatives were also suggested to participate as photosensitiser and co-catalyst, as summarised in a recent review (Xie et al., 2013).

rGO and HTC-biocarbon are potential candidates for enhancing the surface properties of ZnO due to its structural and surface properties. rGO possesses a disrupted sp^2 network that is able to act as electron transfer agent and protective layer over the ZnO layer. On the other hand, HTC-biocarbon prepared *via* PVA-templated method comprised of a carbon-carbon hybrid of carbonaceous spheres and graphene-like carbon sheets, which suggested that HTC-biocarbon may act as a protective layer over ZnO against photocorrosion. The availability of oxygen-containing functional groups on the

surface of rGO and HTC-biocarbon potentially allows the materials to interact with ZnO surface and form a protective layer over the ZnO film. **Therefore, the experiments in this Chapter were conducted to investigate the ability of rGO and HTC-biocarbon to enhance the surface properties of ZnO.**

This chapter is organized into three sections as summarised in Figure 5.1. The chapter begins with a description of the electrochemical preparation of ZnO and nanostructured carbon-hybridised ZnO photoanodes, as well as techniques used to analyse the chemical, physical and electrochemical properties of the photoanodes (Section 5.1). Section 5.2.1 presents an analysis of the changes in physical, chemical and electrochemical properties of rGO-hybridised ZnO photoanodes as a result of rGO ordering i.e. a comparison is made between rGO/ZnO and ZnO/rGO with regards to the improvement in electron transfer efficiency. Subsequently, HTC-biocarbon prepared in this research project was explored and developed as a potential material for surface passivation layer in Section 5.2.2. The results from both studies are discussed in Section 5.3.

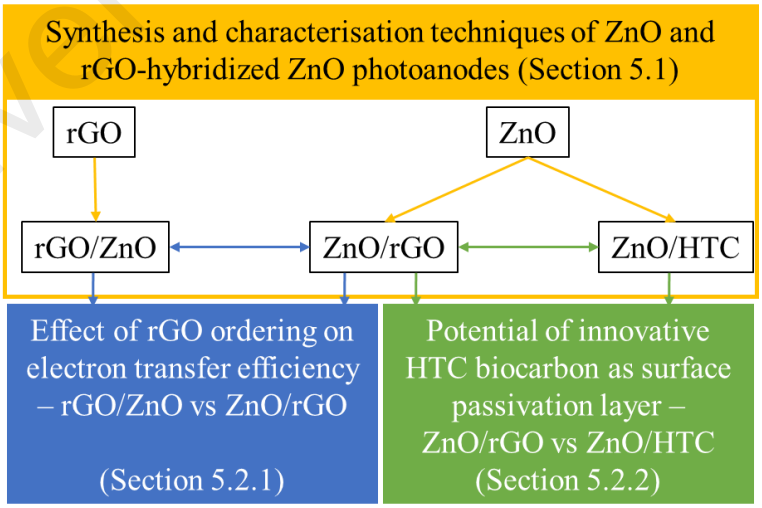

Figure 5.1 Experimental outline of Chapter 5

5.2 Materials and methods

The chemicals used in this study were as follows. $Zn(NO_3)_2 \cdot 6H_2O$ and EDA were obtained from R&M Chemicals (Malaysia), whereas NH_4NO_3, KOH and KCl were purchased from Merck (USA). ITO-coated glass with sheet resistance of < 7 Ω sq^{-1} purchased from Magna Value Sdn. Bhd. (Malaysia) was used as the conductive substrate for the electrodeposition of rGO-hybridised ZnO thin films.

To distinguish the rGO-hybridised ZnO photoanodes, the naming convention of the samples follows the number of layers and the order of layering, beginning from the bottom layer i.e. the term "rGO/ZnO" refers to ZnO grown on rGO coated ITO glass, whereas "ZnO/rGO" refers to rGO-coated ZnO. Similarly, "ZnO/HTC" refers to HTC-biocarbon-coated ZnO thin film.

5.2.1 Preparation of rGO-hybridised ZnO photoanodes (rGO/ZnO and ZnO/rGO)

The rGO/ZnO and ZnO/rGO films were prepared *via* a layer-by-layer electrochemical deposition technique using a three-electrode electrochemical cell coupled to an Autolab PGSTAT302A electrochemical workstation. Platinum wire and Ag/AgCl were used as the counter and reference electrode, respectively. Briefly, the rGO/ZnO film was prepared by growing a layer of ZnO on rGO film, whereas the ZnO/rGO film was prepared by dip-coating the ZnO film with GO followed by electrochemical reduction, and is summarised in Figure 5.2. Prior to electrochemical deposition, the ITO substrate was cleaned using the method outlined in Section 4.2.1.1.

Following a previously-established method (Upadhyay et al., 2014), the preparation of rGO/ZnO sample was as follows. GO was reduced to rGO using a potentiodynamic

method, whereby the applied potential was scanned between 0.0 to -1.5 V at a scan rate of 10 mV s^{-1} over 4 cycles. The electrolyte solution comprised of 0.2 g GO dispersed in 50 mL 0.05 M KOH solution as the electrolyte solution. After rinsing the rGO film with deionized H_2O and air-dried, the ZnO layer was electrochemically deposited by applying a constant potential of -1.1 V for 15 minutes in a 60 °C H_2O bath and constant stirring. The duration of 15 minutes was selected based on the findings in Section 4.3.2.2 (Figure 4.17), to prevent a runaway ZnO growth reaction from occurring. A temperature of 60 °C was selected in order to facilitate the dehydration of $Zn(OH)_2$ to ZnO during the electrochemical process. The electrolyte solution used for the electrochemical deposition of ZnO layer consisted of 0.05 M $Zn(NO_3)_2$, 0.1 M KCl, and 0.05 M ethylenediamine (EDA). The as-prepared thin films were then annealed at 400 °C, at a heating rate of 1 °C min^{-1} and residence time of 3 hours, under argon gas flow.

To prepare the ZnO/rGO sample, ZnO was electrochemically deposited on bare ITO substrate using the same electrolyte and electrochemical technique as described in the previous paragraph. The ZnO layer was coated with GO dip-coating the ZnO film in a 50 mL solution of 7 mg mL^{-1} GO dispersed in ethanol, and allowed to dry between each immersion. Then, the as-prepared film was immersed in phosphate buffer solution and a voltage of -1.2 V was applied for 2 minutes, in order to reduce GO to rGO.

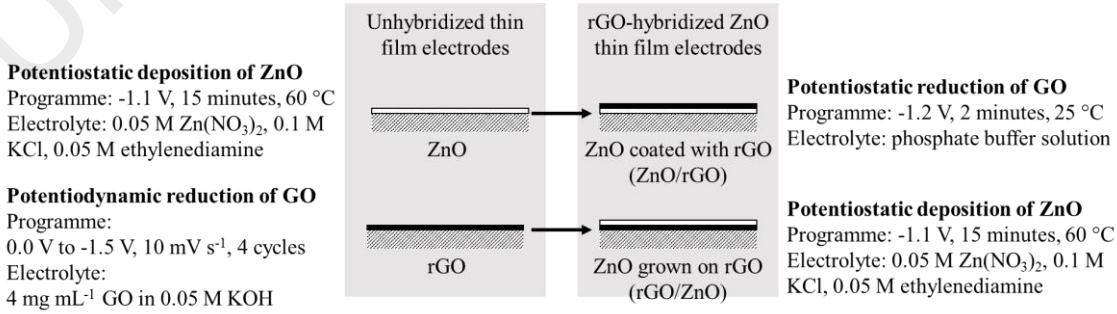

Figure 5.2 Summary of preparation of rGO-hybridised ZnO thin films using electrochemical deposition techniques

5.2.2 Preparation of HTC-hybridised ZnO thin films (ZnO/HTC)

ZnO/HTC samples were prepared as follows, and is illustrated in Figure 5.3. Clean ITO substrate was used as the working electrode, and immersed into the electrolyte solution. A constant voltage of -0.9 V was applied for 15 minutes. The temperature of the electrodeposition cell was maintained at 60 °C using a H_2O bath. The electrolyte solution used for the electrodeposition of ZnO comprised $Zn(NO_3)_2 \cdot 6H_2O$, NH_4NO_3 and EDA which were used as zinc precursor, supporting electrolyte and structure directing agent, respectively. The electrolyte solution was prepared by dissolving 1.487 g of $Zn(NO_3)_2 \cdot 6H_2O$, 0.400 g of NH_4NO_3 and 5.0 mL of 0.1 M EDA solution to 50 ml with deionized H_2O to produce a cloudy solution with a concentration of 0.1 M $Zn(NO_3)_2 \cdot 6H_2O$, 0.1 M NH_4NO_3 and 0.01 M EDA. This solution was immediately used, and a fresh solution was prepared for the deposition of each thin film. After electrodeposition, all thin film samples were carefully rinsed with deionized H_2O so as not to damage the thin film coating by mechanical abrasion and allowed to air-dry in a desiccator before annealing. A calcination step was performed at 300 °C for 2 hours in argon gas flow to increase the crystallinity of the ZnO film.

The ZnO thin films were HTC-biocarbon as follows. 0.2 g HTC-biocarbon obtained from Section 3.2.2 was dispersed by ultrasonication in 50 mL 95 % ethanol. The ZnO thin films were then dip-coated repeatedly until 5 mL of the HTC-biocarbon+ethanol mixture was deposited on the surface of the ZnO thin film. The ZnO thin film was allowed to dry between successive immersions. A potential of -0.9 V was applied for 30 seconds to reduce the oxygen-containing functional groups on the HTC-biocarbon coating, using an electrolyte containing pH 3 HNO_3 solution. The thin films were rinsed carefully with deionized H_2O and ethanol, then allowed to air-dry before storing in a desiccator until further analysis. This procedure was repeated by substituting HTC-

biocarbon with GO, to produce ZnO/rGO photoanode. A control sample was prepared by immersing a ZnO thin film sample in 95 % ethanol solution, and applying a potential of -0.9 V for 30 seconds using an electrolyte containing pH 3 HNO_3 solution.

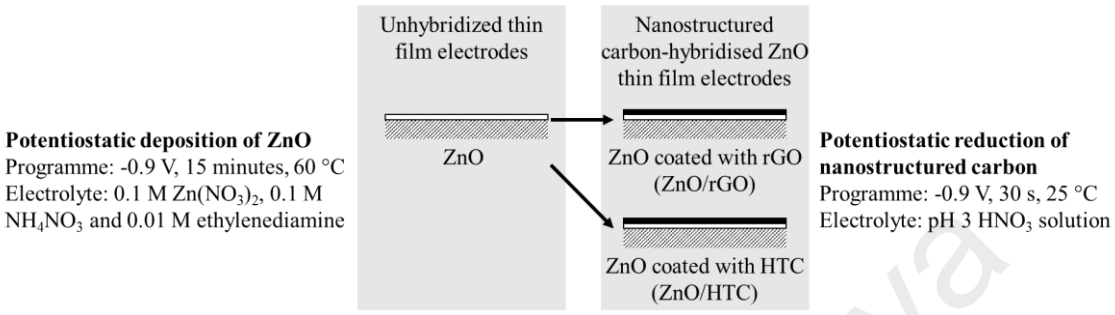

Figure 5.3 Summary of preparation of ZnO/rGO and ZnO/HTC thin films using electrochemical deposition techniques

5.2.3 Materials characterisation

FESEM analysis was carried out using a SUPRA^{TM} 35 VP Field Emission Scanning Electron Microscope (Carl Zeiss, Germany) at an accelerating voltage of 5 kV under high-vacuum conditions. The crystal phase of the rGO/ZnO films were characterized using a model D8 ADVANCE X-ray diffractometer (Bruker, Germany) equipped with Cu Kα radiation (λ = 1.5418 Å) at 40 kV and 30 mA. All the patterns were recorded in the 5–90° range, with a step size of 0.02°. The phase identification of the samples were performed with HighScore Plus software and using reference patterns from the Crystallography Open Database (COD) (Gražulis et al., 2012).

The potential of HTC-biocarbons as material for photocatalytic promoter at the electrode-electrolyte interface was investigated using EIS, LSV and chronoamperometric techniques. The photoelectrochemical characterisations of ZnO/HTC and ZnO/rGO films were carried out in an aqueous 0.1 M KOH electrolyte solution (pH 11). EIS measurements were conducted to determine the internal resistance of the photoanodes, in the 100 mHz to 1 MHz frequency range, with an amplitude of

5 mV at 0 V. Linear scan voltammetries (LSVs) were performed in the dark and under simulated solar light. The linear scan voltammetry was recorded in the anodic direction, in the range of -1.0 to +1.0 V at a scan rate of 50 mV s^{-1}. Chronoamperometry (*I–t*) measurements were performed in two modes, the first at 0.0 V vs. Ag/AgCl over continuous light on–off cycles. The second chronoamperometry measurement was carried out at +1.23 V vs. Ag/AgCl under constant light illumination.

5.3 Research findings

The results of the experiments were analysed to investigate the effect of rGO hybridisation on the physical, chemical and electrochemical properties of ZnO, which in turn affects the photo-conversion efficiency of ZnO. Section 5.2.1 makes a comparison of rGO/ZnO and ZnO/rGO using ZnO grown with KCl as supporting electrolyte. Section 5.2.2 presents an analysis of the properties of ZnO due to coating with rGO and HTC, while making a comparison with rGO/ZnO from Section 4.3.

5.3.1 Effect of ERGO ordering on photoanode photo-conversion efficiency

Figure 5.4 shows the top- and cross-section FESEM images of rGO, ZnO, rGO/ZnO and ZnO/rGO. The electrochemical reduction of GO resulted in the deposition of thin sheets of rGO covering the ITO conductive substrate (Figure 5.4a). The ZnO thin film comprises vertically-aligned, rod-shaped ZnO with tapered ends, due to the application of EDA as the structure-directing agent in this study. The diameter of the rods ranged between 150 nm to 1.1 µm (Figure 5.4b), and the ZnO film possessed a film thickness of 2.61 µm (Figure 5.4f). This observation agrees with previous studies which have

reported the formation of tapered rods with diameters between 100 to 500 nm and rod length of 2 µm (L. Xu et al., 2005).

The ZnO nanorod arrays which were deposited on rGO-coated ITO substrate (rGO/ZnO) possessed rod diameter range between 200 nm to 300 nm (Figure 5.4c), which was narrower compared to the ZnO sample. Nevertheless, the film thickness was reduced to 1.43 µm (Figure 5.4g), which may be due to the further reduction of rGO before ZnO is nucleated and grown on the rGO surface.

The diameter of ZnO sub-microrods in the ZnO/rGO sample were similar to that of the ZnO thin film, with an additional layer of rGO coating the ZnO rods (Figure 5.4d). The ZnO/rGO possessed a film thickness of 2.36 µm (Figure 5.4h), which was similar to ZnO sample.

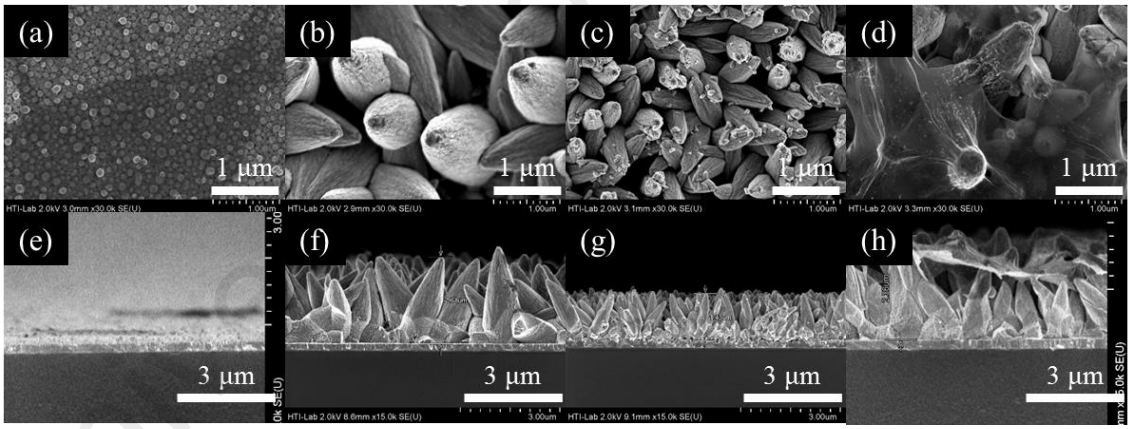

Figure 5.4 FESEM micrographs of the unhybridised and ERGO-hybridised thin films at 30k magnification.

XRD was carried out to confirm the crystal phases present in the prepared thin film electrodes. Figure 5.5a shows diffraction patterns of GO and rGO as well as graphite in the inset graph. The peaks marked with an * symbol are attributed to the ITO conductive layer. The GO sample featured peaks at $2\theta = 9.8$ ° and 15.1 ° were observed,

corresponding to the [001] phase of GO (N. Kumar et al., 2015a) and graphite oxide (K. Zhang et al., 2013a), respectively. The absence of peaks at 2θ = 26.5 ° and 54.5 ° which belong to the [002] and [004] phases of graphite indicate that the restacking of graphene sheets were confined to few layers and did not result in the formation of bulk graphite (Z. Q. Li et al., 2007). Figure 5.5a indicated that GO was reduced to rGO *via* the potentiodynamic method as the XRD diffractogram displayed the formation of a broad [002] peak between 2θ = 13.5 ° to 35 ° (Fang et al., 2009; Mhamane et al., 2011), alongside a sharp [004] peak at 2θ = 33.1 ° (Hiramatsu et al., 2013). The change of [002] and [004] diffraction peak position in GO and rGO was due to the change in crystal structure from sp^3 to sp^2 structure, through the deoxygenation of the oxygen-containing functional groups on the GO surface (Toh et al., 2014).

Figure 5.5b represents the diffractograms of the unhybridised and rGO-hybridised ZnO thin films on ITO glass surface. A broad, low peak between 13.5 to 35 °, attributed to the presence of rGO, was observed in the rGO-hybridised ZnO thin films, but was not present in the unhybridised ZnO thin film. The peaks at 31.8 °, 34.5 °, 36.3 °, 47.5 °, 62.8 ° correspond to the crystalline planes of hexagonal wurtzite structure of ZnO (COD Reference Pattern: 96-101-1259) (Lv et al., 2015). All diffraction patterns exhibited sharp peaks, indicating that a highly crystalline ZnO structure was formed. The [002] peak at 2θ = 34.9 ° was the most intense peak for all samples, which is agreeable with the formation of vertically-aligned ZnO rods observed in FESEM images (Alver et al., 2012; Yin et al., 2010).

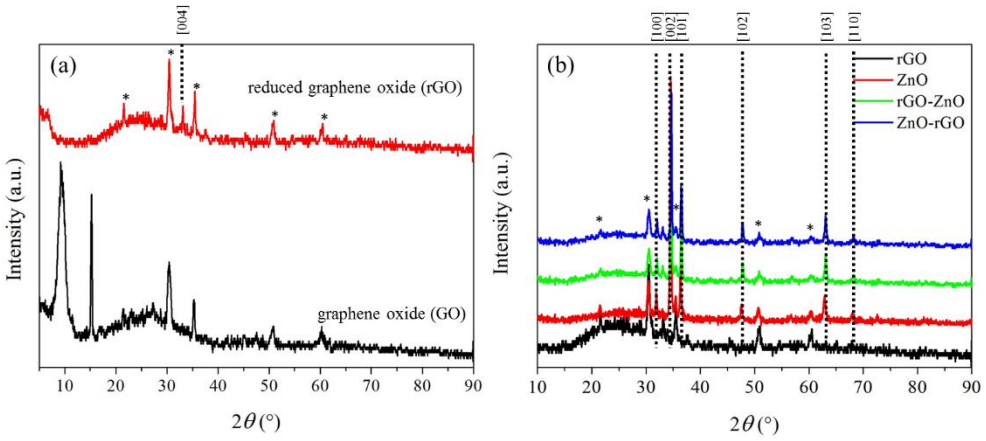

Figure 5.5 XRD diffractograms of (a) GO and rGO, (b) rGO, ZnO, rGO/ZnO and ZnO/rGO films.

The samples were analysed with Raman spectroscopy to investigate the effect of rGO hybridisation on the crystal structure of ZnO. The presence of ZnO was indicated by the E_{2H} peak at 436 cm^{-1}, which can be attributed to the E_{2H} phonon mode (Pradhan et al., 2009). The position of ZnO E_{2H} peak at 436 cm^{-1} indicated that the electrodeposition method was able to prepare crystalline ZnO with few bulk crystal defects. The peak position remained at 436 cm^{-1} for samples rGO/ZnO and ZnO/rGO, which suggested that the rGO hybridisation method did not introduce additional bulk crystal defects during the ZnO crystal growth process.

The D, G, 2D and D+G peaks characteristic to carbon-rich compounds were present in the rGO/ZnO and ZnO/rGO samples at 1350, 1580, 2700 and 2900 cm^{-1} respectively (Malard et al., 2009). The D band, also known as the disorder band, represents a ring breathing mode from sp^2 carbon rings. This mode is activated in the presence of defects or graphene edges, and previous studies reported stronger D band intensity at the edges of graphene, compared to the centre of the graphene sheet (Casiraghi et al., 2009). The G band is an in-plane vibrational mode involving the sp^2 hybridised carbon atoms that

comprises the graphene sheet. The 2D band is the second order of the D band, sometimes referred to as an overtone of the D band (Berciaud et al., 2009).

The structural defects present in rGO can be evaluated its I_D/I_G ratio. In this study, the I_D/I_G ratio increased slightly from 0.65 for the GO film to 0.68 in the rGO film (Figure 5.6a), which suggested that the reduction of C=O group occurred, but restoration of the π conjugation did not occur. When ZnO was grown on rGO-coated ITO glass (rGO/ZnO sample) an I_D/I_G ratio of 0.48 was observed for the rGO/ZnO thin film (Figure 5.6b). In contrast, rGO coated on ZnO by dip-coating technique possessed a higher I_D/I_G ratio of 0.95, compared to the rGO/ZnO thin film. This indicated that the electrochemical reduction of GO resulted in rGO structure with lower sp^3 defects in the rGO/ZnO sample, corresponding with the lowered I_D/I_G ratio. On the other hand, the increase of I_D/I_G ratio for the ZnO/rGO sample suggested that the coating of ZnO with GO by dip-coating method resulted in a high amount of hydrogenated, sp^3 C-H functionality on the basal plane of graphene (Kudin et al., 2008).

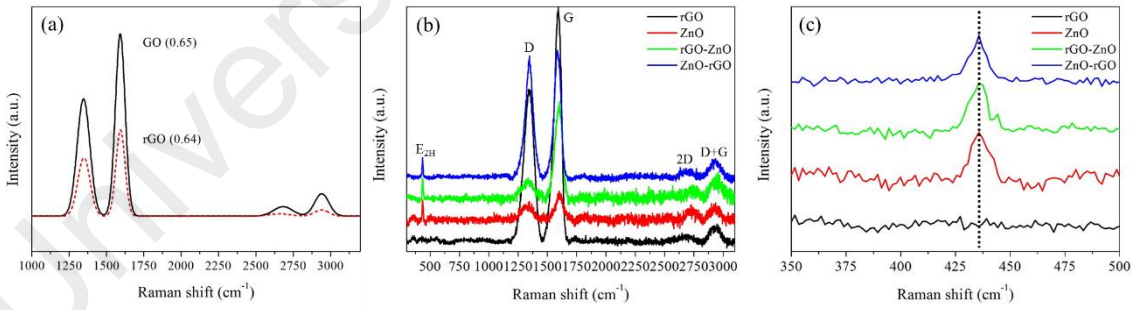

Figure 5.6 Raman spectra of the thin films, showing (a) changes in I_D/I_G ratio from GO to rGO and (b) the E_2, D, G and 2D bands in unhybridised and rGO-hybridised ZnO thin films (c) magnification of E_{2H} peaks

PL spectroscopy provides information on the types of charge transfer (band-to-band, defect based), charge carrier trapping and changes in recombination rate of electron-

hole pairs due to the hybridisation of rGO with ZnO. In this study, ZnO exhibited weak emission peaks at ~360 and 370 nm, which arise due to near-band gap emissions or band-to-band emissions (Figure 5.7). XRD and Raman analyses of the ZnO thin film confirm the formation of well-crystalline, wurtzite phase ZnO, which rules out the possibility of the photoemissions originating from amorphous ZnO present in the sample (Sagnik Das et al., 2014; Somnath Das and Ghosh, 2013). The XRD diffraction pattern of amorphous ZnO feature low, broad peaks (Zhijian Wang et al., 2003), in contrast with the sharp peaks observed in this study. The band-to-band emissions peak is commonly positioned at 380 nm (Valverde-Aguilar and Manríquez Zepeda, 2015), hence, the blueshift of the band-edge emission peak has been previously attributed to localised stain defects leading to quantum trapping at the ZnO crystal surface (J. W. Li et al., 2009). The Burstein-Moss effect may also have been the cause for the blueshift, whereby the apparent band gap increases due to the filling of the CB by electrons (G. H. Lee et al., 2001). The ZnO films (with and without hybridisation) were annealed under inert condition i.e. argon gas was flowed during the annealing process to provide an oxygen-free environment and prevent the oxidation of rGO to CO_2. Li and co-workers proposed that the ZnO polar planes stabilised by OH groups are subject to form V_O by removing either OH or H_2O groups from the surface (G. R. Li et al., 2008). Under inert annealing conditions, the bulk crystal undergoes grain growth but the lack of oxygen prevents the restoration of ZnO crystalline structure at the material's surface (Hernández et al., 2014).

When the ZnO thin film was hybridised with rGO, a redshift in band-to-band emission was observed i.e. the photoluminescence peaks at 360 and 370 nm diminished and was replaced with an emission peak at 380 nm for rGO/ZnO and ZnO/rGO films. It was observed that ZnO/rGO sample possessed higher PL intensity at 380 nm, compared to rGO/ZnO. This suggested that the rGO coating promoted electron transfer process

from rGO to ZnO whereas, rGO as back contact quenched band-to-band emissions due to electron transfer from ZnO to rGO (Ruiz Peralta et al., 2012). It will be noted later that the PEC performance is more significantly affected by recombination due to oxygen defects compared to recombination due to band-to-band emissions.

The origin of the visible emissions at 580 nm has been attributed to V_O (Janotti and Van de Walle, 2009). ZnO possessed the highest photoemission intensity in the visible range, which can be expected due to the formation of V_O under inert annealing conditions. The PL intensities in the visible range were reduced for rGO/ZnO and ZnO/rGO samples, which corresponded to the quenching of PL in the visible region as in the presence of rGO (Q.-P. Luo et al., 2012).

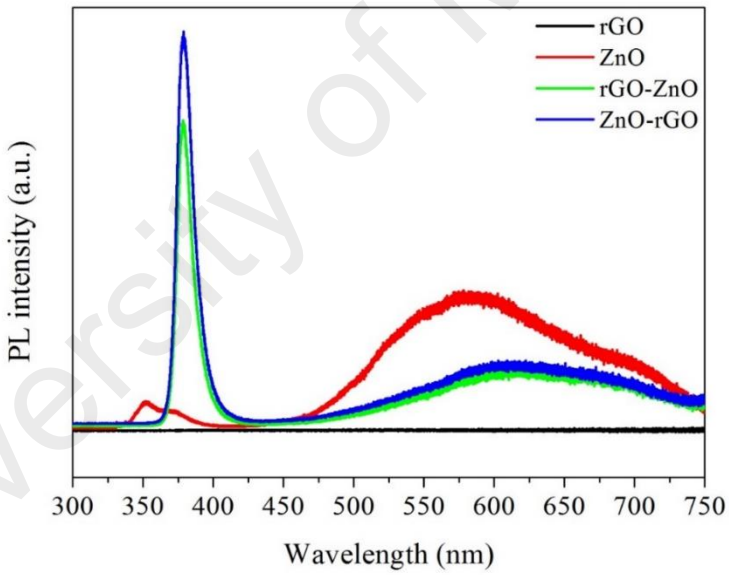

Figure 5.7 PL spectra of the thin films obtained at excitation wavelength of 325 nm

The reflectance properties of ZnO, rGO/ZnO and ZnO/rGO was measured *via* diffuse reflectance UV-Visible spectroscopy and converted to obtain the absorbance, F(R) using the K-M equation:

$$F(R) = \frac{(1-R)^2}{2R} \qquad \text{(Eq. 5.1)}$$

Whereby R = reflectance. Figure 5.8 shows the changes in absorbance properties as a function of incident wavelength. The absorption edge increased from 372 nm (unhybridised ZnO) to 382 and 384 nm for rGO/ZnO and ZnO/rGO samples, respectively. The hybridisation of rGO with ZnO also increased the absorption intensity of ZnO, due to an increase in surface electric charge of the oxides in the ZnO–RGO composite and modification of the fundamental process of electron–hole pair formation during irradiation (X. Liu et al., 2013b; Liwu Zhang et al., 2009a).

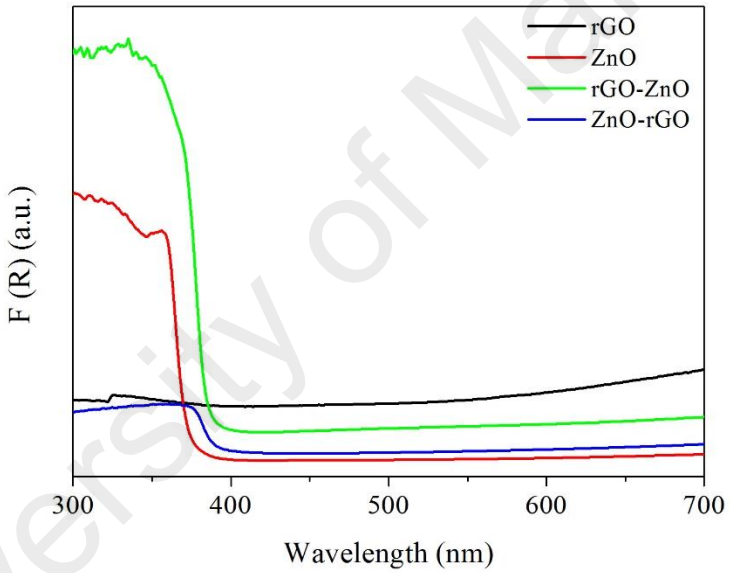

Figure 5.8 K-M absorption spectra of rGO, ZnO, rGO/ZnO and ZnO/rGO films

The effect of rGO hybridisation towards the charge transfer properties of ZnO was evaluated using EIS. Figure 5.9 displays the Nyquist plot obtained under 1.5 AM Xe illumination at +0.4 V vs Ag/AgCl in a three-electrode configuration using 1.0 M NaOH electrolyte. A positive potential was applied in order to observe the properties of unhybridised and rGO-hybridised ZnO thin film as photoanode, through the formation of the depletion layer at the ZnO interface. The raw data was fitted following an

equivalent electrochemical circuit of $R_s(R_{ct}Q)$, whereby R_s, R_{ct} and Q refer to the circuit resistance, charge transfer resistance and constant phase element, respectively (Moniz et al., 2015). The Nyquist plots of ZnO, rGO/ZnO and ZnO/rGO films feature semicircular curves, which is characteristic of the charge transfer process. The diameter of the semicircle represents the charge transfer resistance of the material (R_{ct}) (Lopes et al., 2010). In this study, it can be observed that the charge transfer resistance of the thin films decreased from ZnO > ZnO/rGO > rGO/ZnO, indicating that rGO placed at the ZnO/ITO substrate interface (rGO/ZnO sample) provided a significant reduction in the photoanode charge transfer resistance, compared if rGO was placed at the ZnO/electrolyte interface (ZnO/rGO sample). The observations from EIS analysis suggested that the formation of C-O-Zn bonds as well as narrowing of ZnO rod diameter of ZnO reduced the charge transfer resistance of ZnO.

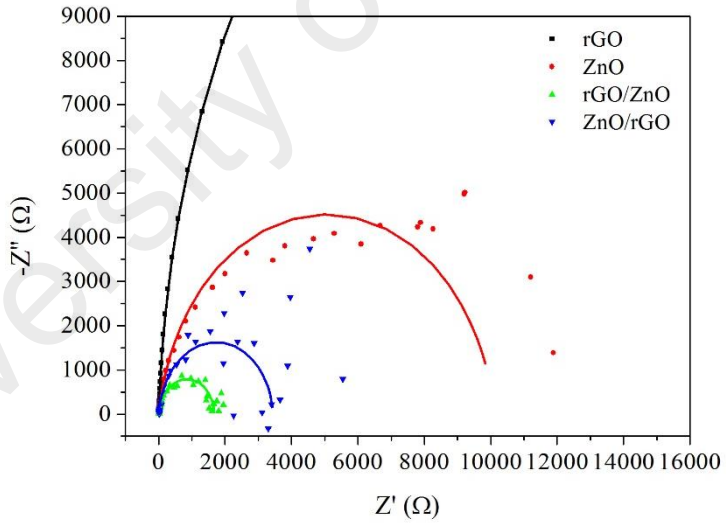

Figure 5.9 Nyquist plots of rGO, ZnO, rGO/ZnO and ZnO/rGO films at +0.4 V vs Ag/AgCl in 1.0 M NaOH under 1.5 AM Xe lamp illumination

The effect of rGO layer ordering towards the photo-conversion efficiency of ZnO was analysed using LSV, with a scan range of -1.0 to +1.0 V and scan rate of 50 mV s^{-1} (Figure 5.10). The ZnO, rGO/ZnO and ZnO/rGO films produced a small current in the

range of 10^{-7} mA cm^{-2} under dark conditions. When the ZnO film was irradiated with 1.5 AM simulated sunlight from a Xe lamp source, a photocurrent was produced from a V_{OC} of -0.42 V. The photocurrent of the ZnO film reached a maximum J of 0.26 mA cm^{-2}, which corresponded to an ABPE of 0.33 % at 0 V. The rGO/ZnO film produced a photocurrent at an onset V_{OC} of -0.44 V and J_{SC} of 0.26 mA cm^{-2}, which indicated that the rGO/ZnO film possessed similar photo-conversion efficiency to ZnO. Nevertheless, the photocurrent of rGO/ZnO film does not reach a plateau, but instead continued to rise to 1.15 mA cm^{-2} at an applied potential of +1.0 V. The ZnO/rGO sample possessed the V_{OC} with the most negative value of -0.48 and an enhanced J_{SC} of 0.46 mA cm^{-2}, which suggested that a layer of rGO coating over the ZnO film was able to enhance the photo-conversion efficiency of ZnO. In comparison with the experiment in Section 4.2, the ABPE values obtained in this experiment are far lower i.e. the rGO/ZnO film in the present experiment yielded ABPE of 0.32 %, whereas the rGO/ZnO film prepared in Section 4.2 yielded ABPE values of 0.39 up to 0.89 %, depending on the rGO preparation method. The major difference between the two experiments was the selection of supporting electrolyte in the electrochemical deposition process. NH_4NO_3 and KCl were used as the supporting electrolytes in Section 4.2 and the present experiment, respectively. Table 5.1 presents a summary of V_{OC} and ABPE values obtained in this experiment.

It was found that although the ZnO/rGO sample possessed the greater Voc compared to rGO/ZnO sample, the charge transfer resistance for the ZnO/rGO sample was also greater than the rGO/ZnO sample. One basic assumption involved in the measurement of charge transfer resistance using EIS is that there are no mediator trap states or surface states present at the interface. However, specific adsorption and other processes at the semiconductor-electrolyte interface may influence the flatband potential as well as the space-charge layer properties (Krishnan, 2007), and may have played a role in the

results obtained from EIS analysis. This observation highlights an important learning point for future experimental design i.e. to examine the adsorption processes at the semiconductor-electrolyte interface, and its impact towards Fermi level and charge transfer resistance.

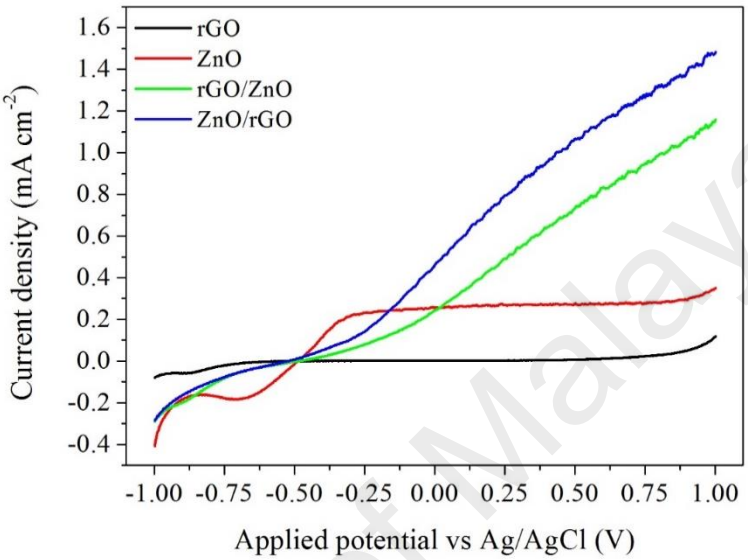

Figure 5.10 LSV curves of rGO, ZnO, rGO/ZnO and ZnO/rGO

Table 5.1 Summary of electrochemical properties of ZnO, rGO/ZnO and ZnO/rGO

Sample	V_{oc} (dark)	V_{oc} (light)	J_{sc} (mA cm^{-2})	J_{1V}, LSV (mA cm^{-2})	ABPE (%)
ZnO	-0.18	-0.42	0.27	0.35	0.33
rGO/ZnO	-0.17	-0.44	0.26	1.15	0.32
ZnO/rGO	-0.16	-0.48	0.46	1.48	0.57

5.3.2 Effect of HTC-biocarbon as alternative nanostructured carbon for hybridised ZnO photoanodes

The FESEM micrographs of ZnO/rGO and ZnO/HTC films are represented in Figure 5.11. The electrochemical deposition method using NH_4NO_3 and EDA as supporting electrolyte and structure-directing agent, respectively, produced ZnO thin films

comprising porous, vertically aligned, rod-shaped ZnO. The ZnO/rGO film contained porous ZnO nanorods with diameters up to 1 µm, whereas the ZnO nanorods in ZnO/HTC possessed narrower diameter (less than 500 nm) and a denser structure. The formation of porous structure was attributed to the formation of H_2 bubbles as structural template during the electrochemical deposition process (Plowman et al., 2015) and was discussed in Section 4.2. Although care was made to ensure that each electrodeposition of ZnO thin film was the same (ITO substrate cleaning method, electrolyte concentration, temperature, applied potential, duration), the variations in ZnO nanorod diameter between ZnO/rGO and ZnO/HTC suggested that the mechanism of ZnO nucleation at the ITO substrate surface was not fully controlled.

The dip-coating and electrochemical reduction by potentiodynamic method resulted in the deposition of thin sheets of rGO covering the ZnO nanorods in the ZnO/rGO thin film. On the contrary, no carbon nanomaterials were visible on the surface of the ZnO/HTC thin film. The reason might be attributed to the issue of poor adhesion, as the HTC material is micro-sized and physisorption may not be sufficient for the initial adhesion to the ZnO nanorod surface.

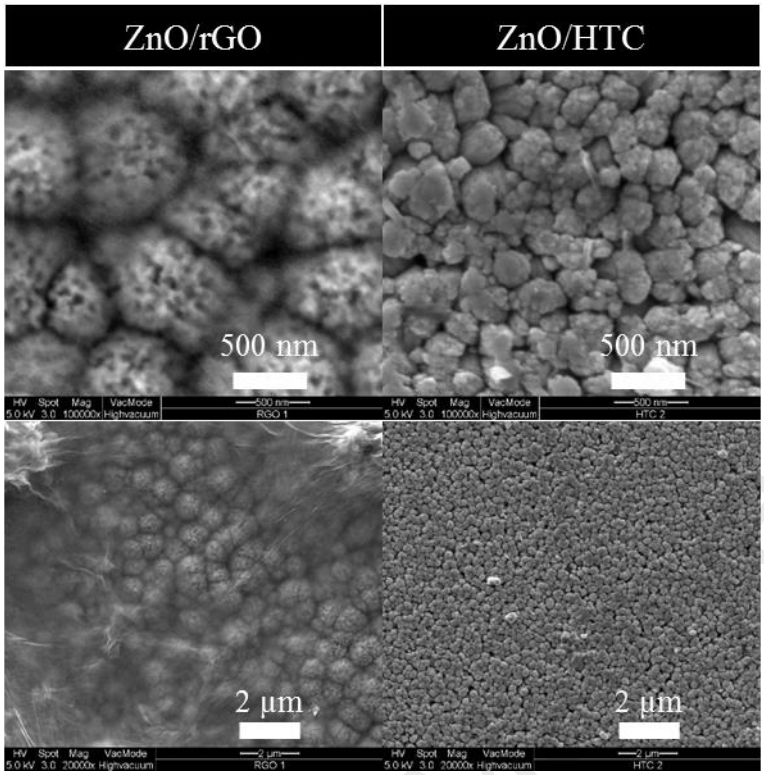

Figure 5.11 FESEM images showing the rGO coating on top of ZnO nanorod arrays. No HTC nanoparticles were observed on the surface of ZnO due to adhesion factors.

Figure 5.12 represents the XRD diffractograms of ZnO, ZnO/rGO and ZnO/HTC thin films. The peaks at 31.8 °, 34.5 °, 36.3 °, 47.5 °, 62.8 ° correspond to the [010], [002], [011], [110] and [013] crystalline planes of hexagonal wurtzite ZnO (COD Reference Pattern: 96-101-1259). All diffraction patterns exhibited sharp peaks, indicating that a highly crystalline ZnO structure was formed. The [002] peak at 2θ = 34.9 ° was the most intense peak for all samples, which is agreeable with the formation of vertically-aligned ZnO nanorods (Alver et al., 2012; Yin et al., 2010).

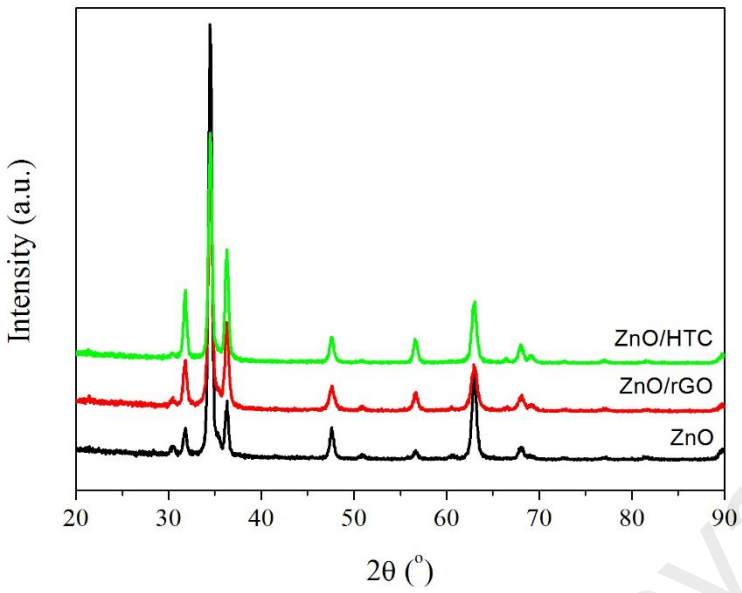

Figure 5.12 XRD diffractograms of ZnO and carbon nanomaterial coated ZnO (ZnO/rGO and ZnO/HTC), showing the presence of [002] dominant phase in ZnO.

The charge transfer resistance of ZnO, ZnO/rGO and ZnO/HTC films were measured at V_{OC} (Figure 5.13a) and 0.0 V (Figure 5.13b) vs Ag/AgCl. The EIS analysis was measured at Voc to observe the charge transfer resistance in the absence of a Schottky barrier), whereas the value of 0.0 V vs Ag/AgCl was selected to determine the internal resistance of the film at the point where the largest current which may be drawn from the photoelectrode (short-circuit potential). The diameter of the semicircle is equal to the charge transfer resistance (Rct) (Lopes et al., 2010).

Based on the Nyquist plot at V_{oc} (Figure 5.13(a)), the graph showed that ZnO/HTC possessed higher charge transfer resistance compared to pristine ZnO, whereas the rGO-coating in ZnO/rGO sample was able to reduce the charge transfer resistance. Interestingly, however, the charge transfer resistance of ZnO/HTC at 0 V (Figure 5.13(b)) is lower compared to pristine ZnO. This observation suggested that the HTC-coating step created favourable surface sites for efficient charge transfer at more

positive bias, thus reducing the charge transfer resistance of the photoelectrode and therefore highest ABPE value.

Figure 5.13b showed that the charge transfer resistance of ZnO was ~1200 Ω, which reduced to 500 and 280 Ω for the ZnO/rGO and ZnO/HTC films, respectively. However, a control ZnO sample, which was not coated with GO but subjected to the electrochemical reduction process similar to ZnO/rGO and ZnO/HTC, demonstrated a charge transfer resistance of 310 Ω. This result indicated that the enhancement of the internal charge resistance was not a result of the rGO coating. Instead, a surface passivation effect took place on the surface of ZnO when a negative potential was applied on the film. It is possible that the application of a negative potential on the ZnO surface was able to reduce the Zn-OH surface functional groups, and thereby reducing the charge transfer resistance of ZnO.

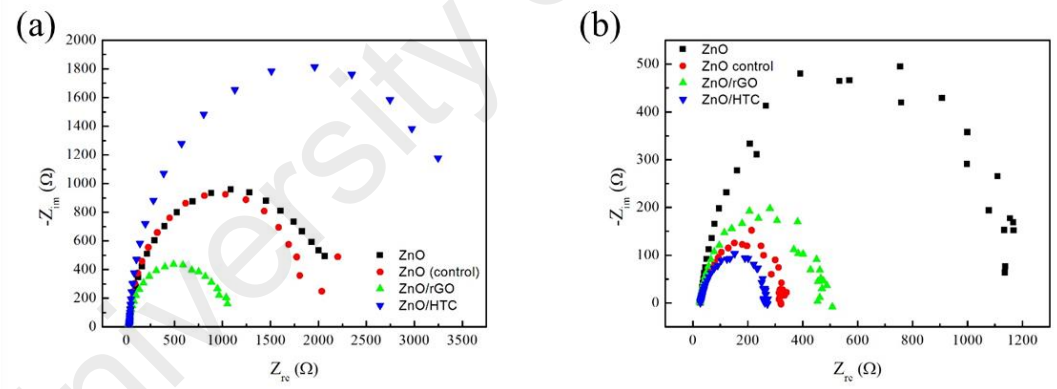

Figure 5.13 Nyquist plots of unhybridised, ZnO/rGO and ZnO/HTC thin films at (a) V_{OC} and (b) 0 V.

Based on the LSV curves in Figure 5.14, the ZnO thin film demonstrated a J_{SC} of 0.245 mA cm^{-2}, whereas the ZnO control and ZnO/rGO films showed an enhanced J_{SC} of 0.385 mA cm^{-2}. The ZnO/HTC thin film showed the highest J_{SC} of 0.425 mA cm^{-2}. Figure 5.14a showed that a small current of 10^{-7} mA cm^{-2} was produced in the absence

of simulated solar irradiation. An oxidation peak at +0.81 V was observed for the linear sweep voltammetry curve for the ZnO/rGO thin film sample, which is attributed to the recombination of O_2 molecules with H^+ ions to form H_2O. Figure 5.14(b) shows that current produced by the ZnO, ZnO control, ZnO/rGO and ZnO/HTC films increased significantly when exposed to 1.5 AM illumination from a Xe lamp source. In particular, ZnO treated using HTC-biocarbon showed the highest increase in PCD, followed by the ZnO control sample, ZnO/rGO and ZnO thin films. The ZnO control, ZnO/rGO and ZnO/HTC films yielded ABPE values of 0.87, 0.81 and 0.90 % (measured at 0 V), which was a significant increase in comparison with the unmodified ZnO film (0.31 %).

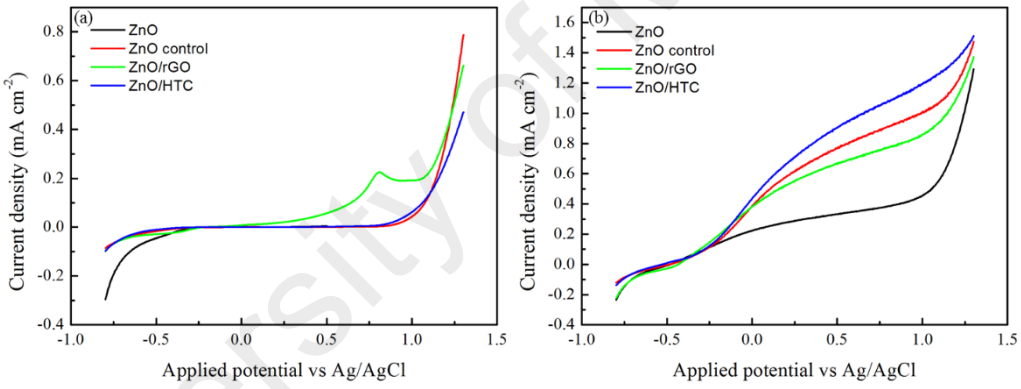

Figure 5.14 Linear sweep voltammetry curves under (a) dark and (b) illumined conditions

Chronoamperometry measurements which were recorded at constant potentials of 0.0 V (Figure 5.15a) and +1.23 V (Figure 5.15b) revealed that the PCD increased from ZnO < ZnO/rGO < ZnO control < ZnO/HTC. The rapid rise and fall in photocurrent due to on/off light exposure in Figure 5.15a indicated that the photogeneration of electron-hole pairs was a rapid process, and that phosphorescence was not the main route of recombination. The photoinduced electron transfer (PET) effect reduces the internal

charge resistance of ZnO thin films under exposure to light (Y. Hu et al., 2010b). The high value of J_{SC} exhibited by the ZnO control indicated that the increase in ZnO thin film photocurrent output was due to the surface passivation of ZnO, rather than the role of rGO as PEC promoter. The lowered PCD of rGO-coated ZnO was likely due to the thickness of the rGO layer, which affected the penetration of light onto the ZnO surface. The highest photocurrent observed for the ZnO thin film treated with HTC-biocarbon, although no HTC-biocarbon was observed from FESEM, is most likely due to the physical property of the ZnO film itself as the nanorod diameter was narrower, and coupled with the surface passivation effect. The chronoamperometry curve measured at +1.23 V revealed that the poor photostability of the unmodified ZnO film, as the photocurrent dropped from an initial value of 1.8 to 0.5 mA cm^{-2} after exposure to simulated solar irradiation for 30 minutes (Figure 5.15b). The surface passivation effect was able to increase the photostability of the ZnO/rGO and ZnO/HTC films, whereby the photocurrent was ~1.3 and 1.4 mA cm^{-2}, respectively. A summary of the V_{OC}, J_{SC} and ABPE yield are summarised in Table 5.2.

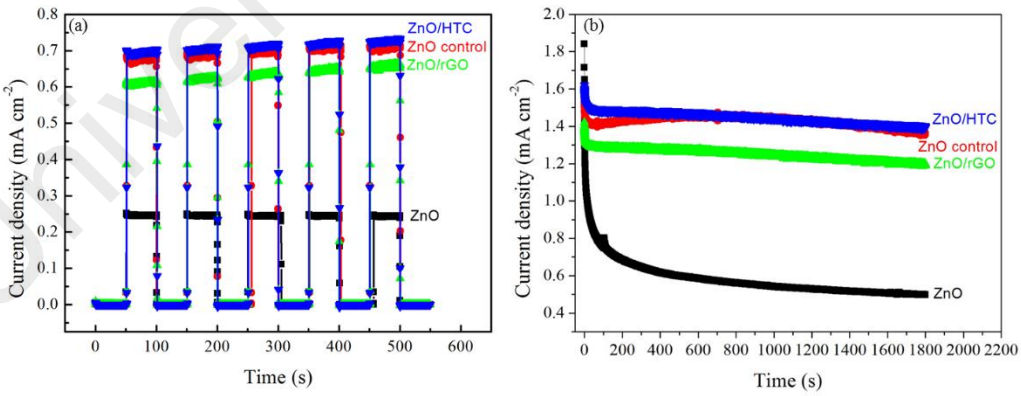

Figure 5.15 Photocurrent response of ZnO, control ZnO, ZnO/rGO and ZnO/HTC at (a) 0.0 V and (b) +1.23 V vs Ag/AgCl.

Table 5.2 Summary of electrochemical properties of ZnO, ZnO/rGO and ZnO/HTC films

Sample	V_{oc} (dark)	V_{oc} (light)	J_{sc} (mA cm^{-2})	J_{1V}, LSV (mA cm^{-2})	ABPE (%)
ZnO	-0.11	-0.47	0.25	0.46	0.31
ZnO control		-0.55	0.71	1.01	0.87
ZnO/rGO		-0.48	0.66	0.87	0.81
ZnO/HTC		-0.53	0.73	1.20	0.90

5.4 Discussion

The study of rGO and HTC-biocarbon as potential material to enhance the surface properties of ZnO highlighted two main points i.e. the role of supporting electrolyte in the preparation of ZnO film and technical issues surrounding the fabrication of ZnO/rGO and ZnO/HTC films.

From this study, it can be observed that the electrochemical deposition of ZnO on bare- and rGO-coated ITO conductive substrate resulted in the formation of ZnO sub-micron rods. XRD analysis confirms the formation of wurtzite ZnO crystal structure. The formation of rod-shaped morphology and sub-micron diameter in the ZnO sample (0.5 to 1.0 µm) agrees with published literature. The formation of rod-shaped morphology was proposed to due to the attachment of structure directing agent to the non-polar [101] and [110] surfaces of the ZnO crystal planes (Postels et al., 2008). This hinders the Zn^{2+} supply and the growth predominantly occurs on the exposed [002] plane, leading to a preferential growth along the c-axis. The selected conditions for electrochemical deposition i.e. electrolyte concentration, applied voltage, temperature and electrodeposition time contributed towards the Ostwald ripening process which resulted in the formation of broad ZnO rod diameter. It was previously reported that a combination of high solution temperature and low precursor concentration resulted in the decrease in rod diameters (F. Xu et al., 2009a). Another study reported that an increase in Zn^{2+} concentration in the electrolyte solution increased the diameter of the

ZnO rod structure (Xue et al., 2011). This same study also reported the formation of ZnO rods with diameter of 350 nm using 0.1 M $Zn(NO)_3$ electrolyte solution and solution temperature of 80 °C. Subsequent studies revealed that dissolved oxygen in the electrolyte solution affects the localised pH at the electrode surface, and an increase in pH results in the increased deposition of ZnO (Cruickshank et al., 2011). The electrodeposition of ZnO on rGO-coated ITO conductive substrate reduced the diameter of the ZnO rods to < 500 nm, which suggests that the rGO affected the growth mechanism of ZnO by moderating the growth rate.

Additionally, the growth of ZnO using NH_4NO_3 electrolyte resulted in the formation of porous structures due to dynamic H_2 bubble templating effect. ZnO crystals grown using NH_4NO_3 as supporting electrolyte was able to increase the photocurrent response (J_{SC} = 0.31 to 0.89 mA cm^{-2}), compared to ZnO grown using KCl as supporting electrolyte (J_{SC} = 0.33 to 0.57 mA cm^{-2}). It was previously reported that Cl^- ions inhibit the photocatalytic efficiency of TiO_2 through competitive adsorption and photogenerated-hole scavenging which led to the formation of -O-Ti-Cl bond on unsaturated Ti sites (Krivec et al., 2014; Y. Yu et al., 2015). It is possible that the Cl^- ion was incorporated at unsaturated Zn sites during the electrochemical deposition process in the experiment described in Section 5.2.1, which resulted in the lower photo-conversion efficiency.

The findings from Section 5.2.1 demonstrated that the layer ordering alters the interaction between the electrode-electrolyte interfaces and subsequently alters the electrochemical properties of the rGO-hybridised ZnO thin film. This observation adds to the understanding that alterations in the morphology of the thin films changes its photovoltaic properties (Zi et al., 2014). Based on EIS analysis, the lowest charge transfer resistance was attributed to rGO/ZnO which agrees with Raman spectroscopy

analysis which indicated the lower presence of sp^3 defects in the rGO layer. We observe, however, that ZnO/rGO demonstrated the highest J_{SC} (0.46 mA cm^{-2}) among the thin films prepared in this study, despite the fact that the charge transfer resistance of the thin film is not the lowest among the samples. The results in Section 5.2.1 suggested that there are other factors beyond charge transfer resistance which are able to significantly influence the efficiency of the PEC water-splitting process. Previous literature has attributed the enhancement of ZnO photocatalytic activity due to the formation of n-p heterojunctions (T.-T. Chen et al., 2013a; K. Yang et al., 2011), but the present findings are not able to conclude if n-p heterojunctions were successfully formed.

Section 5.2.2 reported the effect of rGO and HTC-biocarbon as PEC promoter at the surface was conducted to further examine the surface passivation method using rGO and HTC-biocarbons as surface passivation material. FESEM analysis indicated that the ZnO/rGO hybrid film was formed, but the ZnO/HTC film was not successfully formed. An ABPE value of 0.81 % was achieved for the ZnO/rGO film which is comparable to the rGO/ZnO film prepared in Section 4.2 (0.89 %).

Although the ZnO/rGO film demonstrated enhanced photo-conversion efficiency, it was discovered that the electrochemical reduction method which was meant to convert the GO coating to rGO, was responsible for improving the surface properties of ZnO. The electrochemical reduction step served as a surface passivation technique which reduced the OH groups on the surface of ZnO. Hence, the enhancement of V_{OC}, absorption intensity and charge transfer resistance may be largely attributed to the electrochemical surface passivation of ZnO. While we know that C-O-Zn bonds exist between rGO and ZnO at the solid-solid interface, the nature of the bonding between rGO and ZnO through the dip-coating method is unclear. Therefore, the preparation

techniques of ZnO/HTC and ZnO/rGO needs to be further improved such that a strong bonding between HTC-biocarbon and ZnO are formed. The applicability of HTC-biocarbon as promoter remains to be further explored.

CHAPTER 6: CONCLUSION

6.1 Preamble

This research project was carried out to investigate the influence of nanostructured carbon on PEC water-splitting, by evaluating the effect of hybridising ZnO with nanostructured carbon (rGO and HTC-biocarbon) on the photo-conversion efficiency of ZnO and by exploring the potential of HTC as a sustainable technique to prepare carbon-based PEC water-splitting promoters. The study has also sought to know whether HTC-biocarbons were able to participate as PEC water-splitting promoters. The general literature on the design of HTC-biocarbon and biomass-based nanostructured carbon as promoters in photocatalytic reactions is limited and offers an open opportunity for exploration. Thus, the study sought to achieve the following objectives:

1. To identify the potential of HTC-biocarbon materials prepared through modified HTC synthesis method as carbon-based promoter for PEC water-splitting photoanodes.
2. To identify optimum preparation methods to obtain higher photoelectric performances in carbon-supported ZnO photoanodes.

To achieve these objectives, the first strategy was to modify the existing HTC technique such that the modified HTC technique could to tune the properties of HTC-biocarbon product, e.g. sp^2 content and morphology. The second strategy was to modify the configuration of the rGO-hybridised ZnO films and determine which configuration yielded the highest ABPE value, which is an indicator of photo-conversion efficiency. The physical, optical and electrochemical properties of the hybridised films were characterized to analyse the influence of synthesis parameters on the enhancement in

ABPE value. A synthesis of the findings from this study is presented in the following paragraphs.

Objective 1: To identify the potential of HTC-biocarbon materials prepared through modified HTC synthesis method as carbon-based promoter for PEC water-splitting photoanodes.

The effect of modifying the HTC process with $ZnCl_2$/NaCl activating agent and PVA soft template on the sp^2 content and morphology of the HTC-biocarbon was investigated. It was found that the $ZnCl_2$/NaCl activating agent was able to accelerate the hydrolysis, dehydration and aromatisation reactions at mild reaction conditions (220 °C, autogeneous pressure) leading to the formation of a carbon-dense product. The application of $ZnCl_2$/NaCl as activating agent in the conversion of raw OPSF to HTC-biocarbon was able to increase the carbon density of the HTC-biocarbon product from 51.61 % (without $ZnCl_2$/NaCl) to 63.20 % (with $ZnCl_2$/NaCl). BET surface area analysis indicated that the surface area of OPSF increased from 347.6 m^2 g^{-1} (without $ZnCl_2$/NaCl) to 597.6 m^2 g^{-1} (with $ZnCl_2$/NaCl) due to the role of $ZnCl_2$/NaCl to increase micropore volume. The OPSF-derived HTC-biocarbon prepared in the presence of $ZnCl_2$/NaCl possessed Type I adsorption properties, which indicated mesoporous structure. Thus, this study demonstrated that activating agents accelerate carbonisation reactions under hydrothermal conditions.

The application of PVA as a soft polymer template was able to change the morphology of the HTC-biocarbon, forming a carbon-carbon hybrid HTC-biocarbon product i.e. TEM analysis showed the formation of graphene-like sheets hybridised with carbonaceous spheres. Thus, the formation of a carbon-carbon hybrid HTC-biocarbon

via HTC of PVA+cellulose foam offers an environmentally-friendly and versatile method of tuning the doping and surface properties of the carbon product. It is a promising method to produce doped nanostructured carbon by easily changing the acid type and concentration (e.g. phosphoric, boric or nitric acid). Additionally, the use of PVA and cellulose offers an added advantage as commercially-available materials, to replace the use of toxic precursors (e.g. resorcinol) and expensive soft-templating agents (e.g. Pluronic).

Objective 2: To identify optimum preparation methods to obtain higher photoelectric performances in carbon-supported ZnO photoanodes.

rGO-hybridised ZnO thin films were prepared using electrochemical reduction of GO and electrodeposition to deposit the rGO and ZnO layers, respectively. The thin films were prepared in two configurations i.e. (1) ZnO grown on rGO (rGO/ZnO) and (2) rGO coated on ZnO (ZnO/rGO), in order to investigate the effect of layer ordering on the photoconversion efficiency. The growth of ZnO on rGO film was able to increase the ABPE from 0.30 % (ZnO) up to 0.89 % (rGO/ZnO prepared with CV(1,1) ERGO film), when NH_4NO_3 was used as supporting electrolyte in the electrochemical deposition of ZnO (Section 4.2). The observed ABPE value of 0.89 % was higher compared to previous literature reports. However, the ABPE of ZnO prepared using KCl as supporting electrolyte did not increase as a result of rGO-hybridisation (ZnO = 0.33 %, rGO/ZnO = 0.32 %) (Section 5.2.1). EIS analysis revealed that the enhancement of photo-conversion efficiency of ZnO in rGO/ZnO samples was due to the enhancement of charge transfer properties at the collector-semiconductor interface. Additionally, EIS analysis indicated that the charge transfer at the collector-semiconductor interface is independent of the conductivity of the ZnO material

(rGO/ZnO vs rGO/Cu-ZnO, section 4.1). Based on these observations, it was induced that the ERGO was able to enhance the photo-conversion efficiency of ZnO by the formation of C-O-Zn bond, which facilitates the transfer of electrons across the collector-semiconductor interface.

The effect of GO electrochemical reduction method was further investigated for rGO/ZnO thin films. It was found that rGO prepared under high flux and rate-controlled conditions during the electrochemical reduction of GO resulted in optimum photo-conversion efficiency in rGO/ZnO films. The highest J_{SC} was observed for rGO/ZnO prepared using CV(1,1) and CV(10,50) ERGO films, at 0.73 and 0.69 mA cm^{-2} respectively. The onset potential of ZnO was reduced from -0.46 to -0.56 V vs Ag/AgCl for the rGO/ZnO film prepared using CV(10,50), which suggested that rGO/ZnO film prepared using CV(10,50) ERGO film provided the lowest overpotential for OER. The scan rate, number of scan cycles, duration and applied potential are important parameters which allow control between diffusion- and rate-controlled reactions.

6.2 Limitations of the study

The study was not able to demonstrate conclusively that HTC-biocarbons are able to participate as PEC water-splitting promoters: Despite structural similarities to rGO, HTC was not able to adhere to ZnO using the same method for rGO. Although other studies report the enhancement of photo-conversion efficiency by applying rGO as a passivating coat, the method used to prepare the rGO-coated ZnO in this present study was not the cause for the enhanced J_{SC} value. In section 4.2, the creation of flux and diffusion layer affects the properties of ERGO which in turn affects the physical, optical and electrochemical properties of ZnO. However, the enhanced photo-conversion efficiency observed in the ZnO/rGO sample was not caused by the rGO layering.

Instead, the photo-conversion efficiency was caused by the reduction of the ZnO surface by application of a negative potential passivated the surface. The electrochemical reduction step served as a surface passivation technique which reduced the OH groups on the surface of ZnO. Hence, the enhancement of V_{OC}, absorption intensity and charge transfer resistance may be largely attributed to the electrochemical surface passivation of ZnO. While we know that C-O-Zn bonds exist between rGO and ZnO at the solid-solid interface, the nature of the bonding between rGO and ZnO through the dip-coating method is unclear. Therefore, the preparation techniques of ZnO/HTC and ZnO/rGO needs to be further improved such that a strong bonding between HTC-biocarbon and ZnO are formed. The applicability of HTC-biocarbon as photocatalyst promoter remains to be further explored.

The change of supporting electrolyte complicated the evaluation of photo-conversion efficiency of rGO-hybridised ZnO samples: The analysis of the study was confounded by the change in properties of ZnO as a result of changing the supporting electrolyte. ZnO crystals grown using NH_4NO_3 as supporting electrolyte was able to increase the photocurrent response (J_{SC} = 0.31 to 0.89 mA cm^{-2}), compared to ZnO grown using KCl as supporting electrolyte (J_{SC} = 0.33 to 0.57 mA cm^{-2}). Additionally, the growth of ZnO using NH_4NO_3 electrolyte resulted in the formation of porous structures due to dynamic H_2 bubble templating effect, whereas tapered, non-porous ZnO nanorods were formed when KCl was used as supporting electrolyte. This study highlighted that the composition of supporting electrolyte in the electrodeposition of ZnO is an important parameter affecting the morphology and crystal properties of the electrochemically-deposited ZnO film.

6.3 Recommendations for further research

To produce effective carbon-based PEC water-splitting promoters using sustainable, renewable carbon precursors, there is need for further improvement in the design and synthesis of nanostructured carbon with electrochemical and/or electrocatalytic properties. Exploring the following as future research strategies can facilitate the attainment of this goal:

- Enhancing the conductivity of the HTC-biocarbon
- Development of novel catalysts to tune the sp^2/sp^3 ratio
- Functionalisation and control of surface properties of the HTC-biocarbon
- In-depth study of surface properties of ERGO as a function of flux conditions during electrodeposition process
- Developing other methods to hybridise ZnO with HTC-biocarbon
- Surface study of ERGO prepared by various electrodeposition methods would benefit from advanced surface analysis methods such as XPS.

This study demonstrated that the addition of activating agent and soft template were able to modify the sp^2 content, surface area and morphology of the nanostructured carbon obtained from HTC of renewable carbon precursors, which further informs future design and synthesis efforts of HTC-biocarbons for potential application as PEC water-splitting promoters. This study also demonstrated the effectiveness and tunability of the electrochemical reduction technique to prepare rGO thin films from a colloidal GO solution. Electrochemical parameters such as scan rate, number of cycles, duration and applied voltage control the flux of electrons and GO particles, offering control between diffusion- and rate-controlled reactions.

REFERENCES

Abd Samad, N. A., Lai, C. W., and Abd Hamid, S. B. (2016). Influence Applied Potential on the Formation of Self-Organized ZnO Nanorod Film and Its Photoelectrochemical Response. *International Journal of Photoenergy, 2016*: 8. doi:10.1155/2016/1413072

Abe, R. (2010). Recent progress on photocatalytic and photoelectrochemical water splitting under visible light irradiation. *Journal of Photochemistry and Photobiology C: Photochemistry Reviews, 11*(4): 179-209. doi:10.1016/j.jphotochemrev.2011.02.003

Abe, R., Sayama, K., and Arakawa, H. (2003). Significant effect of iodide addition on water splitting into H_2 and O_2 over Pt-loaded TiO_2 photocatalyst: suppression of backward reaction. *Chemical Physics Letters, 371*(3–4): 360-364. doi:10.1016/S0009-2614(03)00252-5

Addou, R., Dahal, A., Sutter, P., and Batzill, M. (2012). Monolayer graphene growth on Ni[111] by low temperature chemical vapor deposition. *Applied Physics Letters, 100*(2): 02161-02163. doi:10.1063/1.3675481

Ahn, Y., Jeong, Y., and Lee, Y. (2012). Improved thermal oxidation stability of solution-processable silver nanowire transparent electrode by reduced graphene oxide. *ACS Applied Materials & Interfaces, 4*(12): 6410-6414. doi:10.1021/am301913w

Akhavan, O. (2011). Photocatalytic reduction of graphene oxides hybridized by ZnO nanoparticles in ethanol. *Carbon, 49*(1): 11-18. doi:10.1016/j.carbon.2010.08.030

Akihiro, N., Yasuyuki, O., Kayo, K., Yoshihide, H., Kensuke, N., Masakazu, S., and Katsushi, F. (2015). A 24.4% solar to hydrogen energy conversion efficiency by combining concentrator photovoltaic modules and electrochemical cells. *Applied Physics Express, 8*(10): 107101. doi:10.7567/APEX.8.107101

Alexander, B. D., Kulesza, P. J., Rutkowska, I., Solarska, R., and Augustynski, J. (2008). Metal oxide photoanodes for solar hydrogen production. *Journal of Materials Chemistry, 18*(20): 2298-2303. doi:10.1039/B718644D

Alver, U., Zhou, W., Belay, A. B., Krueger, R., Davis, K. O., and Hickman, N. S. (2012). Optical and structural properties of ZnO nanorods grown on graphene oxide and reduced graphene oxide film by hydrothermal method. *Applied Surface Science, 258*(7): 3109-3114. doi:10.1016/j.apsusc.2011.11.046

Ansari, S. A., Khan, M. M., Kalathil, S., Nisar, A., Lee, J., and Cho, M. H. (2013). Oxygen vacancy induced band gap narrowing of ZnO nanostructures by an electrochemically active biofilm. *Nanoscale, 5*(19): 9238-9246. doi:10.1039/C3NR02678G

Baccile, N., Laurent, G., Babonneau, F., Fayon, F., Titirici, M.-M., and Antonietti, M. (2009). Structural characterization of hydrothermal carbon spheres by advanced

solid-state MAS ^{13}C NMR investigations. *The Journal of Physical Chemistry C, 113*(22): 9644-9654. doi:10.1021/jp901582x

Bai, Z., Yan, X., Kang, Z., Hu, Y., Zhang, X., and Zhang, Y. (2015). Photoelectrochemical performance enhancement of ZnO photoanodes from $ZnIn_2S_4$ nanosheets coating. *Nano Energy, 14*: 392-400. doi:10.1016/j.nanoen.2014.09.005

Balahmar, N., Mitchell, A. C., and Mokaya, R. (2015). Generalized mechanochemical synthesis of biomass-derived sustainable carbons for high performance CO_2 storage. *Advanced Energy Materials, 5*(22): 1500867. doi:10.1002/aenm.201500867

Baquero, M. C., Giraldo, L., Moreno, J. C., Suárez-Garcia, F., Martinez-Alonso, A., and Tascón, J. M. D. (2003). Activated carbons by pyrolysis of coffee bean husks in presence of phosphoric acid. *Journal of analytical and applied pyrolysis, 70*(2): 779-784. doi:10.1016/S0165-2370(02)00180-8

Baruah, S., and Dutta, J. (2009). Hydrothermal growth of ZnO nanostructures. *Science and Technology of Advanced Materials, 10*(1): 013001-013018. doi:10.1088/1468-6996/10/1/013001

Batzill, M. (2012). The surface science of graphene: metal interfaces, CVD synthesis, nanoribbons, chemical modifications, and defects. *Surface Science Reports, 67*(3–4): 83-115. doi:10.1016/j.surfrep.2011.12.001

Berciaud, S., Ryu, S., Brus, L. E., and Heinz, T. F. (2009). Probing the Intrinsic Properties of Exfoliated Graphene: Raman Spectroscopy of Free-Standing Monolayers. *Nano Letters, 9*(1): 346-352. doi:10.1021/nl8031444

Bockris, J. O., and Otagawa, T. (1983). Mechanism of oxygen evolution on perovskites. *The Journal of Physical Chemistry, 87*(15): 2960-2971. doi:10.1021/j100238a048

Bockris, J. O. M., and Huq, A. K. M. S. (1956). The Mechanism of the Electrolytic Evolution of Oxygen on Platinum. *Proceedings of the Royal Society of London. Series A. Mathematical and Physical Sciences, 237*(1209): 277-296. doi:10.1098/rspa.1956.0177

Bockris, J. O. M., and Otagawa, T. (1984). The Electrocatalysis of Oxygen Evolution on Perovskites. *Journal of The Electrochemical Society, 131*(2): 290-302. doi:10.1149/1.2115565

Bott, A. W. (1998). Electrochemistry of semiconductors. *Current Separations, 17*: 87-92.

Braga, L. B., Silveira, J. L., da Silva, M. E., Tuna, C. E., Machin, E. B., and Pedroso, D. T. (2013). Hydrogen production by biogas steam reforming: A technical, economic and ecological analysis. *Renewable and Sustainable Energy Reviews, 28*: 166-173. doi:10.1016/j.rser.2013.07.060

Bu, Y., Chen, Z., Li, W., and Hou, B. (2013). Highly efficient photocatalytic performance of graphene–ZnO quasi-shell–core composite material. *ACS Applied Materials & Interfaces, 5*(23): 12361-12368. doi:10.1021/am403149g

Cai, Y., and Feng, Y. P. (2016). Review on charge transfer and chemical activity of TiO_2: Mechanism and applications. *Progress in Surface Science, 91*(4): 183-202. doi:10.1016/j.progsurf.2016.11.001

Cai, Y., Hu, Y., Song, L., Xuan, S., Zhang, Y., Chen, Z., and Fan, W. (2007). Catalyzing carbonization function of ferric chloride based on acrylonitrile–butadiene–styrene copolymer/organophilic montmorillonite nanocomposites. *Polymer Degradation and Stability, 92*(3): 490-496. doi:10.1016/j.polymdegradstab.2006.08.029

Carmo, M., Fritz, D. L., Mergel, J., and Stolten, D. (2013). A comprehensive review on PEM water electrolysis. *International Journal of Hydrogen Energy, 38*(12): 4901-4934. doi:10.1016/j.ijhydene.2013.01.151

Carrasco, J. M., Franquelo, L. G., Bialasiewicz, J. T., Galvan, E., Guisado, R. C. P., Prats, M. A. M., . . . Moreno-Alfonso, N. (2006). Power-electronic systems for the grid integration of renewable energy sources: A survey. *IEEE Transactions on Industrial Electronics, 53*(4): 1002-1016. doi:10.1109/TIE.2006.878356

Casiraghi, C., Hartschuh, A., Qian, H., Piscanec, S., Georgi, C., Fasoli, A., . . . Ferrari, A. C. (2009). Raman spectroscopy of graphene edges. *Nano Letters, 9*(4): 1433-1441. doi:10.1021/nl8032697

Caturla, F., Molina-Sabio, M., and Rodríguez-Reinoso, F. (1991). Preparation of activated carbon by chemical activation with $ZnCl_2$. *Carbon, 29*(7): 999-1007. doi:10.1016/0008-6223(91)90179-M

Chandrasekaran, S., Chung, J. S., Kim, E. J., and Hur, S. H. (2016). Exploring complex structural evolution of graphene oxide/ZnO triangles and its impact on photoelectrochemical water splitting. *Chemical Engineering Journal, 290*: 465-476. doi:10.1016/j.cej.2016.01.029

Chang, Y.-H., Wang, C.-M., Hsu, Y.-K., Pai, Y.-H., Lin, J.-Y., and Lin, C.-H. (2015). Graphene oxide as the passivation layer for Cu_xO photocatalyst on a plasmonic Au film and the corresponding photoluminescence study. *Optics Express, 23*(19): A1245-A1252. doi:10.1364/OE.23.0A1245

Chen, H. M., Chen, C. K., Chang, Y.-C., Tsai, C.-W., Liu, R.-S., Hu, S.-F., . . . Chen, K.-H. (2010). Quantum dot monolayer sensitized ZnO nanowire-array photoelectrodes: True efficiency for water splitting. *Angewandte Chemie, 122*(34): 6102-6105. doi:10.1002/ange.201001827

Chen, H. M., Chen, C. K., Liu, R.-S., Zhang, L., Zhang, J., and Wilkinson, D. P. (2012). Nano-architecture and material designs for water splitting photoelectrodes. *Chemical Society Reviews, 41*(17): 5654-5671. doi:10.1039/C2CS35019J

Chen, M. X., Ge, Z., Li, Y. Y., Agterberg, D. F., Li, L., and Weinert, M. (2016). Effects of interface oxygen vacancies on electronic bands of FeSe/$SrTiO_3$ (001). *Physical Review B, 94*(24): 245139.

Chen, S., Brown, L., Levendorf, M., Cai, W., Ju, S.-Y., Edgeworth, J., . . . Ruoff, R. S. (2011). Oxidation resistance of graphene-coated Cu and Cu/Ni alloy. *ACS Nano, 5*(2): 1321-1327. doi:10.1021/nn103028d

Chen, T.-T., Chang, I. C., Yang, M.-H., Chiu, H.-T., and Lee, C.-Y. (2013a). The exceptional photo-catalytic activity of ZnO/RGO composite via metal and oxygen vacancies. *Applied Catalysis B: Environmental, 142–143*: 442-449. doi:10.1016/j.apcatb.2013.05.059

Chen, Z., Dinh, H., and Miller, E. (2013b). *Photoelectrochemical water splitting: standards, experimental methods, and protocols*: Springer Science & Business Media.

Chen, Z., Zhang, N., and Xu, Y.-J. (2013c). Synthesis of graphene-ZnO nanorod nanocomposites with improved photoactivity and anti-photocorrosion. *CrystEngComm, 15*(15): 3022-3030. doi:10.1039/C3CE27021A

Coenen, J. W. E. (1976). Hydrogenation of Edible oils. *Journal of the American Oil Chemists' Society, 53*(6): 382-389. doi:10.1007/bf02605727

Cortright, R. D., Davda, R. R., and Dumesic, J. A. (2002). Hydrogen from catalytic reforming of biomass-derived hydrocarbons in liquid water. *Nature, 418*(6901): 964-967.

Cruickshank, A. C., Tay, S. E. R., Illy, B. N., Da Campo, R., Schumann, S., Jones, T. S., . . . Ryan, M. P. (2011). Electrodeposition of ZnO nanostructures on molecular thin films. *Chemistry of Materials, 23*(17): 3863-3870. doi:10.1021/cm200764h

Cui, X., Antonietti, M., and Yu, S. H. (2006). Structural effects of iron oxide nanoparticles and iron ions on the hydrothermal carbonization of starch and rice carbohydrates. *Small, 2*(6): 756-759. doi:10.1002/smll.200600047

Damjanovic, A., Dey, A., and Bockris, J. O. M. (1966). Electrode Kinetics of Oxygen Evolution and Dissolution on Rh, Ir, and Pt‐Rh Alloy Electrodes. *Journal of The Electrochemical Society, 113*(7): 739-746. doi:10.1149/1.2424104

Das, J., Pradhan, S. K., Sahu, D. R., Mishra, D. K., Sarangi, S. N., Nayak, B. B., . . . Roul, B. K. (2010). Micro-Raman and XPS studies of pure ZnO ceramics. *Physica B: Condensed Matter, 405*(10): 2492-2497. doi:10.1016/j.physb.2010.03.020

Das, S., Bhattacharjee, K., Maitra, S., and Das, G. C. (2014). Effect of oxygen partial pressure on the photoluminescence properties of sol–gel synthesized nano-structured ZnO thin films. *Thin Solid Films, 550*: 65-70. doi:10.1016/j.tsf.2013.10.045

Das, S., and Ghosh, S. (2013). Fabrication of different morphologies of ZnO superstructures in presence of synthesized ethylammonium nitrate (EAN) ionic liquid: synthesis, characterization and analysis. *Dalton Transactions, 42*(5): 1645-1656. doi:10.1039/C2DT31920A

Dharmadasa, I. M., and Haigh, J. (2006). Strengths and advantages of electrodeposition as a semiconductor growth technique for applications in macroelectronic devices. *Journal of The Electrochemical Society, 153*(1): G47-G52. doi:10.1149/1.2128120

Djurišić, A. B., and Leung, Y. H. (2006). Optical properties of ZnO nanostructures. *Small, 2*(8 ‐ 9): 944-961. doi:10.1002/smll.200600134

Dom, R., Baby, L. R., Kim, H. G., and Borse, P. H. (2013). Enhanced Solar Photoelectrochemical Conversion Efficiency of ZnO:Cu Electrodes for Water-Splitting Application. *International Journal of Photoenergy, 2013*: 9. doi:10.1155/2013/928321

Dong, H., Su, H., Chen, Z., Yu, H., and Yu, H. (2016). Fabrication of Electrochemically Reduced Graphene Oxide Modified Gas Diffusion Electrode for In-situ Electrochemical Advanced Oxidation Process under Mild Conditions. *Electrochimica Acta, 222*: 1501-1509. doi:10.1016/j.electacta.2016.11.131

Dotan, H., Mathews, N., Hisatomi, T., Grätzel, M., and Rothschild, A. (2014). On the solar to hydrogen conversion efficiency of photoelectrodes for water splitting. *The Journal of Physical Chemistry Letters, 5*(19): 3330-3334. doi:10.1021/jz501716g

Dresselhaus, M. S., Jorio, A., and Saito, R. (2010). Characterizing graphene, graphite, and carbon nanotubes by Raman spectroscopy. *Annual Review of Condensed Matter Physics, 1*(1): 89-108. doi:10.1146/annurev-conmatphys-070909-103919

Du, A., Ng, Y. H., Bell, N. J., Zhu, Z., Amal, R., and Smith, S. C. (2011). Hybrid graphene/titania nanocomposite: Interface charge transfer, hole doping, and sensitization for visible light response. *The Journal of Physical Chemistry Letters, 2*(8): 894-899. doi:10.1021/jz2002698

Duerksen, J. H. (1992). USA Patent No. 5145003. T. U. S. P. a. T. Office.

Edwards, P. P., Kuznetsov, V. L., David, W. I. F., and Brandon, N. P. (2008). Hydrogen and fuel cells: towards a sustainable energy future. *Energy Policy, 36*(12): 4356-4362. doi:10.1016/j.enpol.2008.09.036

Egusa, S., Yokota, S., Tanaka, K., Esaki, K., Okutani, Y., Ogawa, Y., . . . Wariishi, H. (2009). Surface modification of a solid-state cellulose matrix with lactose by a surfactant-enveloped enzyme in a nonaqueous medium. *Journal of Materials Chemistry, 19*(13): 1836-1842. doi:10.1039/B819025A

Elaigwu, S. E., and Greenway, G. M. (2016). Chemical, structural and energy properties of hydrochars from microwave-assisted hydrothermal carbonization of glucose. *International Journal of Industrial Chemistry*: 1-8. doi:10.1007/s40090-016-0081-0

Fabbri, E., Habereder, A., Waltar, K., Kotz, R., and Schmidt, T. J. (2014). Developments and perspectives of oxide-based catalysts for the oxygen evolution reaction. *Catalysis Science & Technology, 4*(11): 3800-3821. doi:10.1039/C4CY00669K

Faid, A. Y., and Allam, N. K. (2016). Stable solar-driven water splitting by anodic ZnO nanotubular semiconducting photoanodes. *RSC Advances, 6*(83): 80221-80225. doi:10.1039/C6RA18747A

Fan, G.-C., Zhu, H., Du, D., Zhang, J.-R., Zhu, J.-J., and Lin, Y. (2016). Enhanced Photoelectrochemical Immunosensing Platform Based on CdSeTe@CdS:Mn Core–Shell Quantum Dots-Sensitized TiO_2 Amplified by CuS Nanocrystals Conjugated Signal Antibodies. *Analytical Chemistry, 88*(6): 3392-3399. doi:10.1021/acs.analchem.6b00144

Fan, J., Cao, Y., and Yuan, F. (2015). Shape-control and characterization of iron nanocrystals prepared via a one-step solvothermal method. *Journal of Magnetism and Magnetic Materials, 395*: 257-262. doi:10.1016/j.jmmm.2015.07.070

Fan, W., Lai, Q., Zhang, Q., and Wang, Y. (2011). Nanocomposites of TiO_2 and reduced graphene oxide as efficient photocatalysts for hydrogen evolution. *The Journal of Physical Chemistry C, 115*(21): 10694-10701. doi:10.1021/jp2008804

Fang, M., Wang, K., Lu, H., Yang, Y., and Nutt, S. (2009). Covalent polymer functionalization of graphene nanosheets and mechanical properties of composites. *Journal of Materials Chemistry, 19*(38): 7098-7105. doi:10.1039/B908220D

Farhat, O. F., Halim, M. M., Abdullah, M. J., Ali, M. K. M., Ahmed, N. M., and Allam, N. K. (2015). Growth of vertically aligned ZnO nanorods on Teflon as a novel substrate for low-power flexible light sensors. *Applied Physics A, 119*(4): 1197-1201. doi:10.1007/s00339-015-9177-1

Fechler, N., Wohlgemuth, S.-A., Jäker, P., and Antonietti, M. (2013). Salt and sugar: direct synthesis of high surface area carbon materials at low temperatures via hydrothermal carbonization of glucose under hypersaline conditions. *Journal of Materials Chemistry A, 1*(33): 9418-9421. doi:10.1039/C3TA10674H

Feng, Y., Feng, N., Wei, Y., and Zhang, G. (2014). An in situ gelatin-assisted hydrothermal synthesis of ZnO-reduced graphene oxide composites with enhanced photocatalytic performance under ultraviolet and visible light. *RSC Advances, 4*(16): 7933-7943. doi:10.1039/C3RA46417B

Ferrari, A. C. (2007). Raman spectroscopy of graphene and graphite: Disorder, electron–phonon coupling, doping and nonadiabatic effects. *Solid State Communications, 143*(1–2): 47-57. doi:10.1016/j.ssc.2007.03.052

Ferrari, A. C., and Robertson, J. (2000). Interpretation of Raman spectra of disordered and amorphous carbon. *Physical Review B, 61*(20): 14095-14107. doi:10.1103/PhysRevB.61.14095

Fragalà, M. E., Aleeva, Y., and Malandrino, G. (2010). ZnO nanorod arrays fabrication via chemical bath deposition: ligand concentration effect study. *Superlattices and Microstructures, 48*(4): 408-415. doi:10.1016/j.spmi.2010.07.007

Frimmel, F. H., Abbt-Braun, G., Heumann, K. G., Hock, B., Lüdemann, H.-D., and Spiteller, M. (2008). *Refractory organic substances in the environment*: John Wiley & Sons.

Fu, H., Xu, T., Zhu, S., and Zhu, Y. (2008). Photocorrosion inhibition and enhancement of photocatalytic activity for ZnO via hybridization with C_{60}. *Environmental science & technology, 42*(21): 8064-8069. doi:10.1021/es801484x

Funke, A., and Ziegler, F. (2010). Hydrothermal carbonization of biomass: a summary and discussion of chemical mechanisms for process engineering. *Biofuels Bioproducts and Biorefining*,(4): 160-177. doi:10.1002/bbb.198

Gaikwad, S. S., Gandhi, A. C., Pandit, S. D., Pant, J., Chan, T.-S., Cheng, C.-L., . . . Wu, S. Y. (2014). Oxygen induced strained ZnO nanoparticles: an investigation of Raman scattering and visible photoluminescence. *Journal of Materials Chemistry C, 2*(35): 7264-7274.

Gaillard, N. (2015). Wide bandgap copper indium gallium disulfide thin film materials for photoelectrochemical hydrogen production. *Meeting Abstracts, MA2015-02*(43): 1702.

Gaillard, N., Chang, Y., Kaneshiro, J., Deangelis, A., and Miller, E. L. (2010). Status of research on tungsten oxide-based photoelectrochemical devices at the University of Hawai'i*7770*: 77700V-77700V-77714.

Gao, X.-X., Ge, Q.-Q., Xue, D.-J., Ding, J., Ma, J.-Y., Chen, Y.-X., . . . Hu, J.-S. (2016). Tuning the Fermi-level of TiO_2 mesoporous layer by lanthanum doping towards efficient perovskite solar cells. *Nanoscale, 8*(38): 16881-16885. doi:10.1039/C6NR05917A

Gao, X., Li, X., and Yu, W. (2005). Flowerlike ZnO nanostructures via hexamethylenetetramine-assisted thermolysis of zinc−ethylenediamine complex. *The Journal of Physical Chemistry B, 109*(3): 1155-1161. doi:10.1021/jp046267s

Geim, A. K., and Novoselov, K. S. (2007). The rise of graphene. *Nature Materials, 6*(3): 183-191. doi:10.1038/nmat1849

Gonzalez-Valls, I., and Lira-Cantu, M. (2009). Vertically-aligned nanostructures of ZnO for excitonic solar cells: a review. *Energy & Environmental Science, 2*(1): 19-34. doi:10.1039/B811536B

Goux, A., Pauporté, T., Chivot, J., and Lincot, D. (2005). Temperature effects on ZnO electrodeposition. *Electrochimica Acta, 50*(11): 2239-2248. doi:10.1016/j.electacta.2004.10.007

Gratzel, M. (2001). Photoelectrochemical cells. *Nature, 414*(6861): 338-344.

Gražulis, S., Daškevič, A., Merkys, A., Chateigner, D., Lutterotti, L., Quirós, M., . . . LeBail, A. (2012). Crystallography Open Database (COD): an open-access collection of crystal structures and platform for world-wide collaboration. *Nucleic Acids Research, 40*: D420-D427.

Guiotoku, M., Rambo, C. R., Hansel, F. A., Magalhães, W. L. E., and Hotza, D. (2009). Microwave-assisted hydrothermal carbonization of lignocellulosic materials. *Materials Letters, 63*(30): 2707-2709. doi:10.1016/j.matlet.2009.09.049

Guo, C. X., Dong, Y., Yang, H. B., and Li, C. M. (2013). Graphene quantum dots as a green sensitizer to functionalize ZnO nanowire arrays on F-doped SnO_2 glass for enhanced photoelectrochemical water splitting. *Advanced Energy Materials, 3*(8): 997-1003. doi:10.1002/aenm.201300171

Gupta, M., Sharma, V., Shrivastava, J., Solanki, A., Singh, A. P., Satsangi, V. R., . . . Shrivastav, R. (2009). Preparation and characterization of nanostructured ZnO thin films for photoelectrochemical splitting of water. *Bulletin of Materials Science, 32*(1): 23-30. doi:10.1007/s12034-009-0004-1

Gupta, R. (Ed.) (2008). *Hydrogen fuel: Production, transport, and storage*. USA: CRC Press.

Hamid, S. B. A., Teh, S. J., Lai, C. W., Perathoner, S., and Centi, G. (2016). Applied bias photon-to-current conversion efficiency of ZnO enhanced by hybridization with reduced graphene oxide. *Journal of Energy Chemistry, In Press*. doi:10.1016/j.jechem.2016.11.006

Han, C., Yang, M.-Q., Weng, B., and Xu, Y.-J. (2014). Improving the photocatalytic activity and anti-photocorrosion of semiconductor ZnO by coupling with versatile carbon. *Physical Chemistry Chemical Physics, 16*(32): 16891-16903. doi:10.1039/C4CP02189D

Han, J., Liu, Z., Guo, K., Zhang, X., Hong, T., and Wang, B. (2015). $AgSbS_2$ modified ZnO nanotube arrays for photoelectrochemical water splitting. *Applied Catalysis B: Environmental, 179*: 61-68. doi:10.1016/j.apcatb.2015.05.008

Hao, W., Björkman, E., Lilliestråle, M., and Hedin, N. (2013). Activated carbons prepared from hydrothermally carbonized waste biomass used as adsorbents for CO_2. *Applied Energy, 112*: 526-532. doi:10.1016/j.apenergy.2013.02.028

Harinipriya, S., and Sangaranarayanan, M. V. (2002). Influence of the Work Function on Electron Transfer Processes at Metals: Application to the Hydrogen Evolution Reaction. *Langmuir, 18*(14): 5572-5578. doi:10.1021/la025548t

He, C. N., Tian, F., and Liu, S. J. (2009). A simple method for fabricating single-crystalline Fe nanowires. *Materials Letters, 63*(15): 1252-1254. doi:10.1016/j.matlet.2009.02.057

Hernández, S., Cauda, V., Chiodoni, A., Dallorto, S., Sacco, A., Hidalgo, D., . . . Pirri, C. F. (2014). Optimization of 1D ZnO@TiO_2 core–shell nanostructures for enhanced photoelectrochemical water splitting under solar light illumination.

ACS Applied Materials & Interfaces, 6(15): 12153-12167. doi:10.1021/am501379m

Hiramatsu, M., Kondo, H., and Hori, M. (2013). Graphene Nanowalls. In J. R. Gong (Ed.), *New Progress on Graphene Research*: InTech.

Hisatomi, T., Kubota, J., and Domen, K. (2014). Recent advances in semiconductors for photocatalytic and photoelectrochemical water splitting. *Chemical Society Reviews, 43*(22): 7520-7535. doi:10.1039/C3CS60378D

Hoare, J. P. (1967). Oxygen electrode on noble metals. *Advances in Electrochemical Sciences and Engineering, 6*: 201-288.

Hsieh, P. T., Chen, Y. C., Wang, C. M., Tsai, Y. Z., and Hu, C. C. (2006). Structural and photoluminescence characteristics of ZnO films by room temperature sputtering and rapid thermal annealing process. *Applied Physics A, 84*(3): 345-349. doi:10.1007/s00339-006-3620-2

Hsu, Y.-K., Lin, Y.-G., and Chen, Y.-C. (2011). Polarity-dependent photoelectrochemical activity in ZnO nanostructures for solar water splitting. *Electrochemistry Communications, 13*(12): 1383-1386. doi:10.1016/j.elecom.2011.08.016

Hu, B., Wang, K., Wu, L., Yu, S.-H., Antonietti, M., and Titirici, M.-M. (2010a). Engineering carbon materials from the hydrothermal carbonization process of biomass. *Advanced Materials, 22*(7): 813-828. doi:10.1002/adma.200902812

Hu, Y., Chang, Y., Fei, P., Snyder, R. L., and Wang, Z. L. (2010b). Designing the electric transport characteristics of ZnO micro/nanowire devices by coupling piezoelectric and photoexcitation effects. *ACS Nano, 4*(2): 1234-1240. doi:10.1021/nn901805g

Hwang, Y. J., Hahn, C., Liu, B., and Yang, P. (2012). Photoelectrochemical properties of TiO_2 nanowire arrays: A study of the dependence on length and atomic layer deposition coating. *ACS Nano, 6*(6): 5060-5069. doi:10.1021/nn300679d

Illy, B. N., Cruickshank, A. C., Schumann, S., Da Campo, R., Jones, T. S., Heutz, S., . . . Ryan, M. P. (2011). Electrodeposition of ZnO layers for photovoltaic applications: controlling film thickness and orientation. *Journal of Materials Chemistry, 21*(34): 12949-12957. doi:10.1039/C1JM11225B

Inoue, Y. (2009). Photocatalytic water splitting by RuO_2-loaded metal oxides and nitrides with d^0- and d^{10}-related electronic configurations. *Energy & Environmental Science, 2*(4): 364-386. doi:10.1039/B816677N

Iqbal, J., Jan, T., Shafiq, M., Arshad, A., Ahmad, N., Badshah, S., and Yu, R. (2014). Synthesis as well as Raman and optical properties of Cu-doped ZnO nanorods prepared at low temperature. *Ceramics International, 40*(1, Part B): 2091-2095. doi:10.1016/j.ceramint.2013.07.122

Ito, Y., Ohmori, T., Nakamatsu, S., and Yoshizawa, S. (1980). A molten salt electrolytic process for recovering chlorine and ammonia from ammonium chloride. *Journal of Applied Electrochemistry, 10*(4): 419-425. doi:10.1007/bf00614074

IUPAC. (1997a). Diffusion layer (concentration boundary layer). In A. D. McNaught & A. Wilkinson (Eds.), Compendium of Chemical Terminology (2 ed.). Oxford, UK: Blackwell Scientific Publications. doi:10.1351/goldbook.D01725

IUPAC. (1997b). Energy flux density. In A. D. McNaught & A. Wilkinson (Eds.), Compendium of Chemical Terminology (2 ed.). Oxford, UK: Blackwell Scientific Publications. doi:10.1351/goldbook.E02106.

Jafari, T., Moharreri, E., Amin, A. S., Miao, R., Song, W., and Suib, S. L. (2016). Photocatalytic Water Splitting-The Untamed Dream: A Review of Recent Advances. *Molecules, 21*(7). doi:10.3390/molecules21070900

Jamari, S. S., and Howse, J. R. (2012). The effect of the hydrothermal carbonization process on palm oil empty fruit bunch. *Biomass and Bioenergy, 47*: 82-90.

Janotti, A., and Van de Walle, C. G. (2009). Fundamentals of zinc oxide as a semiconductor. *Reports on Progress in Physics, 72*(12): 126501. doi:10.0.4.64/0034-4885/72/12/126501

Jayah, N. A., Yahaya, H., Mahmood, M. R., Terasako, T., Yasui, K., and Hashim, A. M. (2015). High electron mobility and low carrier concentration of hydrothermally grown ZnO thin films on seeded α-plane sapphire at low temperature. *Nanoscale Research Letters, 10*(1): 1-10. doi:10.1186/s11671-014-0715-0

Jeon, T. H., Choi, S. K., Jeong, H. W., Kim, S., and Park, H. (2011). Photoelectrochemical water oxidation using ZnO nanorods coupled with cobalt-based catalysts. *Journal of Electrochemical Science and Technology, 2*(4): 187-192. doi:10.5229/JECST.2011.2.4.187

Jo, W.-K., and Clament Sagaya Selvam, N. (2015). Enhanced visible light-driven photocatalytic performance of ZnO–g-C_3N_4 coupled with graphene oxide as a novel ternary nanocomposite. *Journal of Hazardous Materials, 299*: 462-470. doi:10.1016/j.jhazmat.2015.07.042

Juodkazis, K., Juodkazytė, J., Jelmakas, E., Kalinauskas, P., Valsiūnas, I., Miečinskas, P., and Juodkazis, S. (2010). Photoelectrolysis of water: solar hydrogen–achievements and perspectives. *Optics Express, 18*(S2): A147-A160. doi:10.1364/OE.18.00A147

Kalderis, D., Bethanis, S., Paraskeva, P., and Diamadopoulos, E. (2008). Production of activated carbon from bagasse and rice husk by a single-stage chemical activation method at low retention times. *Bioresource technology, 99*(15): 6809-6816. doi:10.1016/j.biortech.2008.01.041

Kamat, P. V. (2012). Manipulation of charge transfer across semiconductor interface. A criterion that cannot be ignored in photocatalyst design. *The Journal of Physical Chemistry Letters, 3*(5): 663-672. doi:10.1021/jz201629p

Kang, S., Li, X., Fan, J., and Chang, J. (2012). Characterization of hydrochars produced by hydrothermal carbonization of lignin, cellulose, D-xylose, and wood meal. *Industrial & Engineering Chemistry Research, 51*(26): 9023-9031.

Kaniyankandy, S., Rawalekar, S., and Ghosh, H. N. (2012). Ultrafast charge transfer dynamics in photoexcited CdTe quantum dot decorated on graphene. *The Journal of Physical Chemistry C, 116*(30): 16271-16275. doi:10.1021/jp303712y

Karthik, M., Faik, A., Doppiu, S., Roddatis, V., and D'Aguanno, B. (2015). A simple approach for fabrication of interconnected graphitized macroporous carbon foam with uniform mesopore walls by using hydrothermal method. *Carbon, 87*: 434-443. doi:10.1016/j.carbon.2015.02.060

Kavitha, M. K., Gopinath, P., and John, H. (2015). Reduced graphene oxide-ZnO self-assembled films: tailoring the visible light photoconductivity by the intrinsic defect states in ZnO. *Physical Chemistry Chemical Physics, 17*(22): 14647-14655. doi:10.1039/C5CP01318F

Khajavi, M. R., Blackwood, D. J., Cabanero, G., and Tena-Zaera, R. (2012). New insight into growth mechanism of ZnO nanowires electrodeposited from nitrate-based solutions. *Electrochimica Acta, 69*: 181-189. doi:10.1016/j.electacta.2012.02.096

Khaselev, O., Bansal, A., and Turner, J. A. (2001). High-efficiency integrated multijunction photovoltaic/electrolysis systems for hydrogen production. *International Journal of Hydrogen Energy, 26*(2): 127-132. doi:10.1016/S0360-3199(00)00039-2

Khaselev, O., and Turner, J. A. (1998). A monolithic photovoltaic-photoelectrochemical device for hydrogen production via water splitting. *Science, 280*(5362): 425-427. doi:10.1126/science.280.5362.425

Khoa, N. T., Kim, S. W., Yoo, D.-H., Cho, S., Kim, E. J., and Hahn, S. H. (2015). Fabrication of Au/graphene-wrapped ZnO-nanoparticle-assembled hollow spheres with effective photoinduced charge transfer for photocatalysis. *ACS Applied Materials & Interfaces, 7*(6): 3524-3531. doi:10.1021/acsami.5b00152

Kobussen, A. G. C., and Broers, G. H. J. (1981). The oxygen evolution on $La_{0.5}Ba_{0.5}CoO_3$. *Journal of Electroanalytical Chemistry and Interfacial Electrochemistry, 126*(1): 221-240. doi:10.1016/S0022-0728(81)80430-5

Krasil'shchikov, A. I. (1963). On the intermediate stages of anodic oxygen evolution. *Zhurnal Fizicheskoi Khimii*,(37): 531.

Krishnan, R. (2007). Fundamentals of Semiconductor Electrochemistry and Photoelectrochemistry *Encyclopedia of Electrochemistry*: Wiley-VCH Verlag GmbH & Co. KGaA.

Krivec, M., Dillert, R., Bahnemann, D. W., Mehle, A., Strancar, J., and Drazic, G. (2014). The nature of chlorine-inhibition of photocatalytic degradation of

dichloroacetic acid in a TiO_2-based microreactor. *Physical Chemistry Chemical Physics, 16*(28): 14867-14873. doi:10.1039/C4CP01043D

Kudin, K. N., Ozbas, B., Schniepp, H. C., Prud'homme, R. K., Aksay, I. A., and Car, R. (2008). Raman spectra of graphite oxide and functionalized graphene sheets. *Nano Letters, 8*(1): 36-41. doi:10.1021/nl071822y

Kumar, C. S. S. R. (2012). In Situ Raman Spectroscopy of Oxidation of Carbon Nanomaterials *Raman Spectroscopy for Nanomaterials Characterization* (pp. 312-313). Berlin Heidelberg: Springer-Verlag

Kumar, N., Srivastava, A. K., Patel, H. S., Gupta, B. K., and Varma, G. D. (2015a). Facile synthesis of ZnO–Reduced graphene oxide nanocomposites for NO_2 gas sensing applications. *European Journal of Inorganic Chemistry, 2015*(11): 1912-1923. doi:10.1002/ejic.201403172

Kumar, R., Kumar, G., Al-Dossary, O., and Umar, A. (2015b). ZnO nanostructured thin films: depositions, properties and applications-a review. *Materials Express, 5*(1): 3-23. doi:10.1166/mex.2015.1204

Kumari, B., Sharma, S., Satsangi, V. R., Dass, S., and Shrivastav, R. (2015). Surface deposition of Ag and Au nano-isles on ZnO thin films yields enhanced photoelectrochemical splitting of water. *Journal of Applied Electrochemistry, 45*(4): 299-312. doi:10.1007/s10800-015-0790-7

Kuriakose, S., Satpati, B., and Mohapatra, S. (2015). Highly efficient photocatalytic degradation of organic dyes by Cu doped ZnO nanostructures. *Physical Chemistry Chemical Physics, 17*(38): 25172-25181. doi:10.1039/C5CP01681A

Lee, G. H., Yamamoto, Y., Kourogi, M., and Ohtsu, M. (2001). Blue shift in room temperature photoluminescence from photo-chemical vapor deposited ZnO films. *Thin Solid Films, 386*(1): 117-120. doi:10.1016/S0040-6090(01)00764-7

Lee, G. J., Lee, Y. P., Lim, H.-H., Cha, M., Kim, S. S., Cheong, H., . . . Han, S.-H. (2010). Photoluminescence and Lasing Properties of ZnO Nanorods. *Journal of Korean Physical Society, 57*(61): 1624-1629.

Leigh, G. J. (2004). Haber-Bosch and Other Industrial Processes. In B. E. Smith, R. L. Richards, & W. E. Newton (Eds.), *Catalysts for Nitrogen Fixation: Nitrogenases, Relevant Chemical Models and Commercial Processes* (pp. 33-54). Dordrecht: Springer Netherlands.

Li, C., Fang, G., Fu, Q., Su, F., Li, G., Wu, X., and Zhao, X. (2006). Effect of substrate temperature on the growth and photoluminescence properties of vertically aligned ZnO nanostructures. *Journal of Crystal Growth, 292*(1): 19-25. doi:10.1016/j.jcrysgro.2006.03.061

Li, G. R., Hu, T., Pan, G. L., Yan, T. Y., Gao, X. P., and Zhu, H. Y. (2008). Morphology−function relationship of ZnO: Polar planes, oxygen vacancies, and activity. *The Journal of Physical Chemistry C, 112*(31): 11859-11864. doi:10.1021/jp8038626

Li, J. W., Liu, X. J., Yang, L. W., Zhou, Z. F., Xie, G. F., Pan, Y., . . . Sun, C. Q. (2009). Photoluminescence and photoabsorption blueshift of nanostructured ZnO: Skin-depth quantum trapping and electron-phonon coupling. *Applied Physics Letters, 95*(3): 031906. doi:10.1063/1.3184566

Li, K., Gao, S., Wang, Q., Xu, H., Wang, Z., Huang, B., . . . Lu, J. (2015a). In-situ-reduced synthesis of Ti^{3+} Self-Doped TiO_2/g-C_3N_4 heterojunctions with high photocatalytic performance under LED light irradiation. *ACS Applied Materials & Interfaces, 7*(17): 9023-9030. doi:10.1021/am508505n

Li, Q., Liu, F., Zhang, L., Nelson, B. J., Zhang, S., Ma, C., . . . Zhang, X. (2012). In situ construction of potato starch based carbon nanofiber/activated carbon hybrid structure for high-performance electrical double layer capacitor. *Journal of Power Sources, 207*: 199-204. doi:10.1016/j.jpowsour.2012.01.142

Li, S., Zhang, Q., Lu, Y., Ji, D., Zhang, D., Wu, J., . . . Liu, Q. (2017). One step electrochemical deposition and reduction of graphene oxide on screen printed electrodes for impedance detection of glucose. *Sensors and Actuators B: Chemical, 244*: 290-298. doi:10.1016/j.snb.2016.12.142

Li, X., Colombo, L., and Ruoff, R. S. (2016a). Synthesis of graphene films on copper foils by chemical vapor deposition. *Advanced Materials*: n/a-n/a. doi:10.1002/adma.201504760

Li, X., Yu, J., Wageh, S., Al-Ghamdi, A. A., and Xie, J. (2016b). Graphene in Photocatalysis: A Review. *Small, 12*(48): 6640-6696. doi:10.1002/smll.201600382

Li, X., Zhang, Z., Chen, L., Liu, Z., Cheng, J., Ni, W., . . . Wang, B. (2014). Cadmium sulfide quantum dots sensitized tin dioxide–titanium dioxide heterojunction for efficient photoelectrochemical hydrogen production. *Journal of Power Sources, 269*: 866-872. doi:10.1016/j.jpowsour.2014.07.060

Li, Y., Wang, R., Li, H., Wei, X., Feng, J., Liu, K., . . . Zhou, A. (2015b). Efficient and stable photoelectrochemical seawater splitting with TiO_2@g-C_3N_4 nanorod arrays decorated by Co-Pi. *The Journal of Physical Chemistry C, 119*(35): 20283-20292. doi:10.1021/acs.jpcc.5b05427

Li, Z. Q., Lu, C. J., Xia, Z. P., Zhou, Y., and Luo, Z. (2007). X-ray diffraction patterns of graphite and turbostratic carbon. *Carbon, 45*(8): 1686-1695. doi:10.1016/j.carbon.2007.03.038

Libra, J. A., Ro, K. S., Kammann, C., Funke, A., Berge, N. D., Neubauer, Y., . . . Kern, J. (2011). Hydrothermal carbonization of biomass residuals: a comparative review of the chemistry, processes and applications of wet and dry pyrolysis. *Biofuels, 2*(1): 71-106. doi:10.4155/bfs.10.81

Licht, S. (2002). Photoelectrochemical solar energy storage cells. *Encyclopedia of Electrochemistry*.

Lin, K.-F., Cheng, H.-M., Hsu, H.-C., Lin, L.-J., and Hsieh, W.-F. (2005). Band gap variation of size-controlled ZnO quantum dots synthesized by sol–gel method. *Chemical Physics Letters, 409*(4–6): 208-211. doi:10.1016/j.cplett.2005.05.027

Lin, Y.-G., Lin, C.-K., Miller, J. T., Hsu, Y.-K., Chen, Y.-C., Chen, L.-C., and Chen, K.-H. (2012). Photochemically active reduced graphene oxide with controllable oxidation level. *RSC Advances, 2*(30): 11258-11262. doi:10.1039/C2RA21988C

Liu, B., and Zeng, H. C. (2004). Room temperature solution synthesis of monodispersed single-crystalline ZnO nanorods and derived hierarchical nanostructures. *Langmuir, 20*(10): 4196-4204. doi:10.1021/la035264o

Liu, C., Wang, K., Luo, S., Tang, Y., and Chen, L. (2011). Direct electrodeposition of graphene enabling the one-step synthesis of graphene–metal nanocomposite films. *Small, 7*(9): 1203-1206. doi:10.1002/smll.201002340

Liu, G., Wang, L., Yang, H. G., Cheng, H.-M., and Lu, G. Q. (2010a). Titania-based photocatalysts-crystal growth, doping and heterostructuring. *Journal of Materials Chemistry, 20*(5): 831-843. doi:10.1039/B909930A

Liu, L., Zhu, Y.-P., Su, M., and Yuan, Z.-Y. (2015). Metal-Free Carbonaceous Materials as Promising Heterogeneous Catalysts. *ChemCatChem, 7*(18): 2765-2787. doi:10.1002/cctc.201500350

Liu, M., Nam, C.-Y., Black, C. T., Kamcev, J., and Zhang, L. (2013a). Enhancing water splitting activity and chemical stability of zinc oxide nanowire photoanodes with ultrathin titania shells. *The Journal of Physical Chemistry C, 117*(26): 13396-13402. doi:10.1021/jp404032p

Liu, M., Qin, X., Liu, C., Pan, L., and Xin, H. (2010b). Ag and Cu doping and their effects on the thermoelectric properties of β-Zn_4Sb_3. *Physical Review B, 81*(24): 245215. doi:10.1063/1.3544479

Liu, X., Pan, L., Lv, T., and Sun, Z. (2013b). Investigation of photocatalytic activities over ZnO–TiO_2–reduced graphene oxide composites synthesized via microwave-assisted reaction. *Journal of Colloid and Interface Science, 394*: 441-444. doi:10.1016/j.jcis.2012.11.047

Llavona, A., Prados, A., Velasco, V., Crespo, P., Sanchez, M. C., and Perez, L. (2013). Electrochemical synthesis and magnetic properties of goethite single crystal nanowires. *CrystEngComm, 15*(24): 4905-4909. doi:10.1039/C3CE26772E

Lockett, A. M., Thomas, P. J., and O'Brien, P. (2012). Influence of seeding layers on the morphology, density, and critical dimensions of ZnO nanostructures grown by chemical bath deposition. *The Journal of Physical Chemistry C, 116*(14): 8089-8094. doi:10.1021/jp211121d

Lopes, T., Andrade, L., Ribeiro, H. A., and Mendes, A. (2010). Characterization of photoelectrochemical cells for water splitting by electrochemical impedance spectroscopy. *International Journal of Hydrogen Energy, 35*(20): 11601-11608. doi:10.1016/j.ijhydene.2010.04.001

Lowell, S., and Shields, J. E. (1991). Adsorption IsothermsPowder Surface Area and Porosity (Vol. 2, pp. 11-13). Netherlands: Springer. doi:10.1007/978-94-015-7955-1

Luo, L.-B., Yu, S.-H., Qian, H.-S., and Gong, J.-Y. (2006). Large scale synthesis of uniform silver@carbon rich composite (carbon and cross-linked PVA) sub-microcables by a facile green chemistry carbonization approach. *Chemical Communications*,(7): 793-795. doi:10.1039/B516048K

Luo, Q.-P., Yu, X.-Y., Lei, B.-X., Chen, H.-Y., Kuang, D.-B., and Su, C.-Y. (2012). Reduced graphene oxide-hierarchical ZnO hollow sphere composites with enhanced photocurrent and photocatalytic activity. *The Journal of Physical Chemistry C, 116*(14): 8111-8117. doi:10.1021/jp2113329

Lv, R., Wang, X., Lv, W., Xu, Y., Ge, Y., He, H., . . . Li, Q. (2015). Facile synthesis of ZnO nanorods grown on graphene sheets and its enhanced photocatalytic efficiency. *Journal of Chemical Technology & Biotechnology, 90*(3): 550-558. doi:10.1002/jctb.4347

Malard, L. M., Pimenta, M. A., Dresselhaus, G., and Dresselhaus, M. S. (2009). Raman spectroscopy in graphene. *Physics Reports, 473*(5–6): 51-87. doi:10.1016/j.physrep.2009.02.003

Marrani, A. G., Caprioli, F., Boccia, A., Zanoni, R., and Decker, F. (2014). Electrochemically deposited ZnO films: an XPS study on the evolution of their surface hydroxide and defect composition upon thermal annealing. *Journal of Solid State Electrochemistry, 18*(2): 505-513. doi:10.1007/s10008-013-2281-2

Matulionis, I., Hu, J., Zhu, F., Gallon, J., Gaillard, N., Deutsch, T., . . . Madan, A. (2010). Surface modification of a-SiC photoelectrodes for photocurrent enhancement. *Solar Hydrogen and Nanotechnology V, 7770*: 77700Z-77701-77708. doi:10.1117/12.860669

May, M. M., Lewerenz, H.-J., Lackner, D., Dimroth, F., and Hannappel, T. (2015). Efficient direct solar-to-hydrogen conversion by in situ interface transformation of a tandem structure. *Nature Communications, 6*. doi:10.1038/ncomms9286

Menamparambath, M. M., Park, J.-H., Yoo, H.-S., Patole, S. P., Yoo, J.-B., Kim, S. W., and Baik, S. (2014). Large work function difference driven electron transfer from electrides to single-walled carbon nanotubes. *Nanoscale, 6*(15): 8844-8851. doi:10.1039/C4NR01629G

Mhamane, D., Ramadan, W., Fawzy, M., Rana, A., Dubey, M., Rode, C., . . . Ogale, S. (2011). From graphite oxide to highly water dispersible functionalized graphene by single step plant extract-induced deoxygenation. *Green Chemistry, 13*(8): 1990-1996. doi:10.1039/C1GC15393E

Minella, M., Sordello, F., and Minero, C. (2017). Photocatalytic process in TiO_2/graphene hybrid materials. Evidence of charge separation by electron transfer from reduced graphene oxide to TiO_2. *Catalysis Today, 281, Part 1*: 29-37. doi:10.1016/j.cattod.2016.03.040

Modak, J. M. (2002). Haber process for ammonia synthesis. *Resonance, 7*(9): 69-77. doi:10.1007/bf02836187

Moezzi, A., McDonagh, A. M., and Cortie, M. B. (2012). Zinc oxide particles: Synthesis, properties and applications. *Chemical Engineering Journal, 185–186*: 1-22. doi:10.1016/j.cej.2012.01.076

Molina-Sabio, M., and Rodrıguez-Reinoso, F. (2004). Role of chemical activation in the development of carbon porosity. *Colloids and Surfaces A: Physicochemical and Engineering Aspects, 241*(1): 15-25.

Moniz, S. J. A., Shevlin, S. A., Martin, D. J., Guo, Z.-X., and Tang, J. (2015). Visible-light driven heterojunction photocatalysts for water splitting - a critical review. *Energy & Environmental Science, 8*(3): 731-759. doi:10.1039/C4EE03271C

Moo, J. G. S., Khezri, B., Webster, R. D., and Pumera, M. (2014). Graphene oxides prepared by Hummers', Hofmann's, and Staudenmaier's methods: dramatic influences on heavy-metal-ion adsorption. *ChemPhysChem, 15*(14): 2922-2929. doi:10.1002/cphc.201402279

Moshiul Alam, A. K. M., Beg, M. D. H., Reddy Prasad, D. M., Khan, M. R., and Mina, M. F. (2012). Structures and performances of simultaneous ultrasound and alkali treated oil palm empty fruit bunch fiber reinforced poly(lactic acid) composites. *Composites Part A: Applied Science and Manufacturing, 43*(11): 1921-1929. doi:10.1016/j.compositesa.2012.06.012

Murphree, E. V., Brown, C. L., and Gohr, E. J. (1940). Hydrogenation of petroleum. *Industrial & Engineering Chemistry, 32*(9): 1203-1212. doi:10.1021/ie50369a031

Na, Y., Hu, B., Yang, Q.-L., Liu, J., Zhou, L., Fan, R.-Q., and Yang, Y.-L. (2015). CdS quantum dot sensitized p-type NiO as photocathode with integrated cobaloxime in photoelectrochemical cell for water splitting. *Chinese Chemical Letters, 26*(1): 141-144. doi:10.1016/j.cclet.2014.09.011

Nagaraju, G., Manjunath, K., Sarkar, S., Gunter, E., Teixeira, S. R., and Dupont, J. (2015). TiO_2–RGO hybrid nanomaterials for enhanced water splitting reaction. *International Journal of Hydrogen Energy, 40*(36): 12209-12216. doi:10.1016/j.ijhydene.2015.07.094

Natsume, Y., and Sakata, H. (2000). Zinc oxide films prepared by sol-gel spin-coating. *Thin Solid Films, 372*(1–2): 30-36. doi:10.1016/S0040-6090(00)01056-7

Negahdar, L., Delidovich, I., and Palkovits, R. (2016). Aqueous-phase hydrolysis of cellulose and hemicelluloses over molecular acidic catalysts: Insights into the kinetics and reaction mechanism. *Applied Catalysis B: Environmental, 184*: 285-298. doi:10.1016/j.apcatb.2015.11.039

Nizamuddin, S., Jayakumar, N. S., Sahu, J. N., Ganesan, P., Bhutto, A. W., and Mubarak, N. M. (2015). Hydrothermal carbonization of oil palm shell. *Korean Journal of Chemical Engineering, 32*(9): 1789-1797. doi:10.1007/s11814-014-0376-9

Noack, V., and Eychmüller, A. (2002). Annealing of nanometer-sized zinc oxide particles. *Chemistry of Materials, 14*(3): 1411-1417. doi:10.1021/cm011262i

Pang, Q., Wang, L., Yang, H., Jia, L., Pan, X., and Qiu, C. (2014). Cellulose-derived carbon bearing -Cl and -SO_3H groups as a highly selective catalyst for the hydrolysis of cellulose to glucose. *RSC Advances, 4*(78): 41212-41218. doi:10.1039/C4RA05520A

Park, S., and Ruoff, R. S. (2009). Chemical methods for the production of graphenes. *Nature Nanotechnology, 4*(4): 217-224.

Ping, J., Wang, Y., Fan, K., Wu, J., and Ying, Y. (2011). Direct electrochemical reduction of graphene oxide on ionic liquid doped screen-printed electrode and its electrochemical biosensing application. *Biosensors and Bioelectronics, 28*(1): 204-209. doi:10.1016/j.bios.2011.07.018

Plowman, B. J., Jones, L. A., and Bhargava, S. K. (2015). Building with bubbles: the formation of high surface area honeycomb-like films via hydrogen bubble templated electrodeposition. *Chemical Communications, 51*(21): 4331-4346. doi:10.1039/C4CC06638C

Poh, H. L., Sanek, F., Ambrosi, A., Zhao, G., Sofer, Z., and Pumera, M. (2012). Graphenes prepared by Staudenmaier, Hofmann and Hummers methods with consequent thermal exfoliation exhibit very different electrochemical properties. *Nanoscale, 4*(11): 3515-3522. doi:10.1039/C2NR30490B

Postels, B., Bakin, A., Wehmann, H.-H., Suleiman, M., Weimann, T., Hinze, P., and Waag, A. (2008). Electrodeposition of ZnO nanorods for device application. *Applied Physics A, 91*(4): 595-599. doi:10.1007/s00339-008-4487-1

Pradhan, D., Kumar, M., Ando, Y., and Leung, K. T. (2009). Fabrication of ZnO nanospikes and nanopillars on ITO glass by templateless seed-layer-free electrodeposition and their field-emission properties. *ACS Applied Materials & Interfaces, 1*(4): 789-796. doi:10.1021/am800220v

Prasai, D., Tuberquia, J. C., Harl, R. R., Jennings, G. K., and Bolotin, K. I. (2012). Graphene: corrosion-inhibiting coating. *ACS Nano, 6*(2): 1102-1108. doi:10.1021/nn203507y

Prasek, J., Drbohlavova, J., Chomoucka, J., Hubalek, J., Jasek, O., Adam, V., and Kizek, R. (2011). Methods for carbon nanotubes synthesis-review. *Journal of Materials Chemistry, 21*(40): 15872-15884. doi:10.1039/C1JM12254A

Pullini, D., Pruna, A., Zanin, S., and Mataix, D. B. (2011). High-efficiency electrodeposition of large scale ZnO nanorod arrays for thin transparent electrodes. *Journal of The Electrochemical Society, 159*(2): E45-E51. doi:10.1149/2.093202jes

Qiu, Y., Yan, K., Deng, H., and Yang, S. (2012). Secondary branching and nitrogen doping of ZnO nanotetrapods: Building a highly active network for photoelectrochemical water splitting. *Nano Letters, 12*(1): 407-413. doi:10.1021/nl2037326

Rahman, M. Y. A., Umar, A. A., Taslim, R., and Salleh, M. M. (2015). Effect of surfactant on the physical properties of ZnO nanorods and the performance of ZnO photoelectrochemical cell. *Journal of Experimental Nanoscience, 10*(8): 599-609. doi:10.1080/17458080.2013.858374

Reddy, N. K., Devika, M., and Tu, C. W. (2014). Vertically aligned ZnO nanorods on flexible substrates for multifunctional device applications: easy and cost-effective route. *Materials Letters, 120*: 62-64.

Rehman, S., Ullah, R., Butt, A. M., and Gohar, N. D. (2009). Strategies of making TiO_2 and ZnO visible light active. *Journal of Hazardous Materials, 170*(2–3): 560-569. doi:10.1016/j.jhazmat.2009.05.064

Rodriguez, C. A. D., and Tremiliosi-Filho, G. (2013). Electrochemical Deposition. In Q. J. Wang & Y.-W. Chung (Eds.), *Encyclopedia of Tribology* (pp. 918-922). Boston, MA: Springer US.

Rosenblatt, S. (1996). US5554659.

Rudd, A. L., and Breslin, C. B. (2000). Photo-induced dissolution of zinc in alkaline solutions. *Electrochimica Acta, 45*(10): 1571-1579. doi:10.1016/S0013-4686(99)00322-9

Ruiz Peralta, M. D. L., Pal, U., and Zeferino, R. S. (2012). Photoluminescence (PL) Quenching and Enhanced Photocatalytic Activity of Au-Decorated ZnO Nanorods Fabricated through Microwave-Assisted Chemical Synthesis. *ACS Applied Materials & Interfaces, 4*(9): 4807-4816. doi:10.1021/am301155u

Ryu, J., Suh, Y.-W., Suh, D. J., and Ahn, D. J. (2010). Hydrothermal preparation of carbon microspheres from mono-saccharides and phenolic compounds. *Carbon, 48*(7): 1990-1998.

Sanchez, S., Lévy-Clément, C., and Ivanova, V. (2012). Electrochemical Deposition of ZnO Thin Films and Nanowires for Photovoltaic Applications. *Journal of The Electrochemical Society, 159*(12): D705-D712. doi:10.1149/2.024212jes

Sapkal, R. T., Shinde, S. S., Waghmode, T. R., Govindwar, S. P., Rajpure, K. Y., and Bhosale, C. H. (2012). Photo-corrosion inhibition and photoactivity enhancement with tailored zinc oxide thin films. *Journal of Photochemistry and Photobiology B: Biology, 110*: 15-21. doi:10.1016/j.jphotobiol.2012.02.004

Schwan, J., Ulrich, S., Batori, V., Ehrhardt, H., and Silva, S. (1996). Raman spectroscopy on amorphous carbon films. *Journal of Applied Physics, 80*(1): 440-447.

Sengupta, D., Das, P., Mondal, B., and Mukherjee, K. (2016). Effects of doping, morphology and film-thickness of photo-anode materials for dye sensitized solar cell application – A review. *Renewable and Sustainable Energy Reviews, 60*: 356-376. doi:10.1016/j.rser.2016.01.104

Serrano, D. P., Botas, J. A., Fierro, J. L. G., Guil-López, R., Pizarro, P., and Gómez, G. (2010). Hydrogen production by methane decomposition: Origin of the catalytic

activity of carbon materials. *Fuel, 89*(6): 1241-1248. doi:10.1016/j.fuel.2009.11.030

Sevilla, M., and Fuertes, A. B. (2009a). Chemical and structural properties of carbonaceous products obtained by hydrothermal carbonization of saccharides. *Chemistry – A European Journal, 15*(16): 4195-4203. doi:10.1002/chem.200802097

Sevilla, M., and Fuertes, A. B. (2009b). The production of carbon materials by hydrothermal carbonization of cellulose. *Carbon, 47*(9): 2281-2289. doi:10.1016/j.carbon.2009.04.026

Sevilla, M., Maciá-Agulló, J. A., and Fuertes, A. B. (2011). Hydrothermal carbonization of biomass as a route for the sequestration of CO_2: Chemical and structural properties of the carbonized products. *Biomass and Bioenergy, 35*(7): 3152-3159. doi:10.1016/j.biombioe.2011.04.032

Sewell, G. L. (1963). Model of thermally activated hopping motion in solids. *Physical Review, 129*(2): 597-608.

Sha, D., Wang, J., Wu, X., Zou, H., Dai, Y., Ren, J., . . . Yan, X. (2016). One-step and large-scale preparation of TiO_2/amorphous carbon composites with excellent visible light photocatalytic properties. *RSC Advances, 6*(70): 65607-65612. doi:10.1039/C6RA11250A

Shang, H., Lu, Y., Zhao, F., Chao, C., Zhang, B., and Zhang, H. (2015). Preparing high surface area porous carbon from biomass by carbonization in a molten salt medium. *RSC Advances, 5*(92): 75728-75734. doi:10.1039/C5RA12406A

Shao, D., Yu, M., Lian, J., and Sawyer, S. M. L. (2013). Ultraviolet Photodetector Fabricated From Multiwalled Carbon Nanotubes/Zinc-Oxide Nanowires/p-GaN Composite Structure. *IEEE Electron Device Letters, 34*(9): 1169-1171. doi:10.1109/LED.2013.2273351

Sharma, D., Jha, R., and Kumar, S. (2016). Quantum dot sensitized solar cell: Recent advances and future perspectives in photoanode. *Solar Energy Materials and Solar Cells, 155*: 294-322. doi:10.1016/j.solmat.2016.05.062

Sharma, R., Alam, F., Sharma, A. K., Dutta, V., and Dhawan, S. K. (2014). ZnO anchored graphene hydrophobic nanocomposite-based bulk heterojunction solar cells showing enhanced short-circuit current. *Journal of Materials Chemistry C, 2*(38): 8142-8151. doi:10.1039/C4TC01056F

Sharma, V., Kumar, P., Shrivastava, J., Solanki, A., Satsangi, V. R., Dass, S., and Shrivastav, R. (2011). Vertically aligned nanocrystalline Cu–ZnO thin films for photoelectrochemical splitting of water. *Journal of Materials Science, 46*(11): 3792-3801. doi:10.1007/s10853-011-5293-2

Shen, Y., and Lua, A. C. (2016). A trimodal porous carbon as an effective catalyst for hydrogen production by methane decomposition. *Journal of Colloid and Interface Science, 462*: 48-55. doi:10.1016/j.jcis.2015.09.050

Shockley, W., and Read, W. T. (1952). Statistics of the recombinations of holes and electrons. *Physical Review, 87*(5): 835-842.

Singh, A. P., Kodan, N., Mehta, B. R., Held, A., Mayrhofer, L., and Moseler, M. (2016). Band Edge Engineering in $BiVO_4/TiO_2$ Heterostructure: Enhanced Photoelectrochemical Performance through Improved Charge Transfer. *ACS Catalysis, 6*(8): 5311-5318. doi:10.1021/acscatal.6b00956

Skompska, M., and Zarębska, K. (2014). Electrodeposition of ZnO nanorod arrays on transparent conducting substrates–a review. *Electrochimica Acta, 127*: 467-488. doi:10.1016/j.electacta.2014.02.049

Solanki, A., Shrivastava, J., Upadhyay, S., Choudhary, S., Sharma, V., Sharma, P., . . . Dass, S. (2013). Modified structural, morphological and photoelectrochemical properties of 120 MeV Ag^{9+} ion irradiated $BaTiO_3$ thin films. *Current Applied Physics, 13*(2): 344-350. doi:10.1016/j.cap.2012.08.005

Son, D. I., Kwon, B. W., Yang, J. D., Park, D. H., Seo, W. S., Lee, H., . . . Choi, W. K. (2012). Charge separation and ultraviolet photovoltaic conversion of ZnO quantum dots conjugated with graphene nanoshells. *Nano Research, 5*(11): 747-761. doi:10.1007/s12274-012-0258-6

Song, S. M., Park, J. K., Sul, O. J., and Cho, B. J. (2012). Determination of work function of graphene under a metal electrode and its role in contact resistance. *Nano Letters, 12*(8): 3887-3892. doi:10.1021/nl300266p

Srikant, V., and Clarke, D. R. (1998). On the optical band gap of zinc oxide. *Journal of Applied Physics, 83*(10): 5447-5451. doi:10.1063/1.367375

Steinmiller, E. M. P., and Choi, K.-S. (2009). Photochemical deposition of cobalt-based oxygen evolving catalyst on a semiconductor photoanode for solar oxygen production. *Proceedings of the National Academy of Sciences, 106*(49): 20633-20636. doi:10.1073/pnas.0910203106

Sugami, Y., Minami, E., and Saka, S. (2016). Renewable diesel production from rapeseed oil with hydrothermal hydrogenation and subsequent decarboxylation. *Fuel, 166*: 376-381. doi:10.1016/j.fuel.2015.10.117

Suib, S. L. (2013). Catalysis in fuel cells and hydrogen production. In S. L. Suib (Ed.), *New and future developments in catalysis: batteries, hydrogen storage and fuel cells* (pp. 249). Poland: Elsevier.

Sun, J.-X., Yuan, Y.-P., Qiu, L.-G., Jiang, X., Xie, A.-J., Shen, Y.-H., and Zhu, J.-F. (2012). Fabrication of composite photocatalyst g-C_3N_4-ZnO and enhancement of photocatalytic activity under visible light. *Dalton Transactions, 41*(22): 6756-6763. doi:10.1039/C2DT12474B

Sun, L., Yi, Z., Lin, J., Liang, F., Wu, Y., Cao, Z., and Wang, L. (2016). Fast and energy efficient synthesis of ZnO@RGO and its application in Ni–Zn secondary battery. *The Journal of Physical Chemistry C, 120*(23): 12337-12343. doi:10.1021/acs.jpcc.6b01025

Suryanarayana, C., and Norton, M. G. (2013). *X-ray diffraction: a practical approach*: Springer Science & Business Media.

Sutter, E., Albrecht, P., Camino, F. E., and Sutter, P. (2010). Monolayer graphene as ultimate chemical passivation layer for arbitrarily shaped metal surfaces. *Carbon, 48*(15): 4414-4420. doi:10.1016/j.carbon.2010.07.058

Swiegers, G. F., MacFarlane, D. R., Officer, D. L., Ballantyne, A., Boskovic, D., Chen, J., . . . Winther-Jensen, O. (2012). Towards hydrogen energy: Progress on catalysts for water splitting. *Australian Journal of Chemistry, 65*(6): 577-582. doi:10.1071/CH12048

Tan, S. T., Chen, B., Sun, X., Fan, W., Kwok, H., Zhang, X., and Chua, S. (2005). Blueshift of optical band gap in ZnO thin films grown by metal-organic chemical-vapor deposition. *Journal of Applied Physics, 98*(1): 0135051-0135055. doi:10.1063/1.1940137

Tang, L., Li, X., Ji, R., Teng, K. S., Tai, G., Ye, J., . . . Lau, S. P. (2012). Bottom-up synthesis of large-scale graphene oxide nanosheets. *Journal of Materials Chemistry, 22*(12): 5676-5683. doi:10.1039/C2JM15944A

Tavakoli, M. M., Tavakoli, R., Nourbakhsh, Z., Waleed, A., Virk, U. S., and Fan, Z. (2016). High Efficiency and Stable Perovskite Solar Cell Using ZnO/rGO QDs as an Electron Transfer Layer. *Advanced Materials Interfaces, 3*: 1500790 (1500791-1500710). doi:10.1002/admi.201500790

Thankalekshmi, R. R., Dixit, S., Bae, I.-T., VanHart, D., and Rastogi, A. C. (2013). Synthesis and characterization of Cu-doped ZnO film in nanowire like morphology using low temperature self-catalytic vapor-liquid-solid (VLS) method. *MRS Online Proceedings Library Archive, 1494*: 37-42. doi:doi:10.1557/opl.2012.1696

Thimsen, E., Le Formal, F., Grätzel, M., and Warren, S. C. (2011). Influence of plasmonic Au nanoparticles on the photoactivity of Fe_2O_3 electrodes for water splitting. *Nano Letters, 11*(1): 35-43. doi:10.1021/nl1022354

Tian, J., Liu, S., Li, H., Wang, L., Zhang, Y., Luo, Y., . . . Sun, X. (2012). One-step preparation of ZnO nanoparticle-decorated reduced graphene oxide composites and their application to photocurrent generation. *RSC Advances, 2*(4): 1318-1321. doi:10.1039/C2RA01114J

Titirici, M.-M., and Antonietti, M. (2010). Chemistry and materials options of sustainable carbon materials made by hydrothermal carbonization. *Chemical Society Reviews, 39*(1): 103-116.

Titirici, M.-M., Thomas, A., and Antonietti, M. (2007). Back in the black: hydrothermal carbonization of plant material as an efficient chemical process to treat the CO_2 problem? *New Journal of Chemistry, 31*(6): 787-789. doi:10.1039/B616045J

Toh, S. Y., Loh, K. S., Kamarudin, S. K., and Daud, W. R. W. (2014). Graphene production via electrochemical reduction of graphene oxide: synthesis and

characterisation. *Chemical Engineering Journal, 251*: 422-434. doi:10.1016/j.cej.2014.04.004

Toh, S. Y., Loh, K. S., Kamarudin, S. K., and Daud, W. R. W. (2016). The impact of electrochemical reduction potentials on the electrocatalytic activity of graphene oxide toward the oxygen reduction reaction in an alkaline medium. *Electrochimica Acta, 199*: 194-203. doi:10.1016/j.electacta.2016.03.103

Tong, X., Yang, P., Wang, Y., Qin, Y., and Guo, X. (2014). Enhanced photoelectrochemical water splitting performance of TiO_2 nanotube arrays coated with an ultrathin nitrogen-doped carbon film by molecular layer deposition. *Nanoscale, 6*(12): 6692-6700. doi:10.1039/C4NR00602J

Trotochaud, L., Ranney, J. K., Williams, K. N., and Boettcher, S. W. (2012). Solution-Cast Metal Oxide Thin Film Electrocatalysts for Oxygen Evolution. *Journal of the American Chemical Society, 134*(41): 17253-17261. doi:10.1021/ja307507a

Upadhyay, S., Bagheri, S., and Abd Hamid, S. B. (2014). Enhanced photoelectrochemical response of reduced-graphene oxide/$Zn_{1-x}Ag_xO$ nanocomposite in visible-light region. *International Journal of Hydrogen Energy, 39*(21): 11027-11034. doi:10.1016/j.ijhydene.2014.05.094

US Department of Energy. (2013). *Report of the Hydrogen Production Expert Panel: A Subcommittee of the Hydrogen & Fuel Cell Technical Advisory Committee*. Retrieved from US: https://www.hydrogen.energy.gov/pdfs/hpep_report_2013.pdf

Valverde-Aguilar, G., and Manríquez Zepeda, J. L. (2015). Photoluminescence and photoconductivity studies on amorphous and crystalline ZnO thin films obtained by sol–gel method. *Applied Physics A, 118*(4): 1305-1313. doi:10.1007/s00339-014-8836-y

van Heek, K. H. (2000). Progress of coal science in the 20th century. *Fuel, 79*(1): 1-26. doi:10.1016/S0016-2361(99)00190-8

Vasudevan, V., and Mushrif, S. H. (2015). Insights into the solvation of glucose in water, dimethyl sulfoxide (DMSO), tetrahydrofuran (THF) and N,N-dimethylformamide (DMF) and its possible implications on the conversion of glucose to platform chemicals. *RSC Advances, 5*(27): 20756-20763. doi:10.1039/C4RA15123B

Veldsink, J. W., Bouma, M. J., Schöön, N. H., and Beenackers, A. A. C. M. (1997). Heterogeneous Hydrogenation of Vegetable Oils: A Literature Review. *Catalysis Reviews, 39*(3): 253-318. doi:10.1080/01614949709353778

Walter, M. G., Warren, E. L., McKone, J. R., Boettcher, S. W., Mi, Q., Santori, E. A., and Lewis, N. S. (2010). Solar Water Splitting Cells. *Chemical Reviews, 110*(11): 6446-6473. doi:10.1021/cr1002326

Wang, D., Czernik, S., and Chornet, E. (1998). Production of Hydrogen from Biomass by Catalytic Steam Reforming of Fast Pyrolysis Oils. *Energy & Fuels, 12*(1): 19-24. doi:10.1021/ef970102j

Wang, J., Tsuzuki, T., Tang, B., Hou, X., Sun, L., and Wang, X. (2012a). Reduced graphene oxide/ZnO composite: reusable adsorbent for pollutant management. *ACS Applied Materials & Interfaces, 4*(6): 3084-3090. doi:10.1021/am300445f

Wang, J., Wang, Z., Huang, B., Ma, Y., Liu, Y., Qin, X., . . . Dai, Y. (2012b). Oxygen Vacancy Induced Band-Gap Narrowing and Enhanced Visible Light Photocatalytic Activity of ZnO. *ACS Applied Materials & Interfaces, 4*(8): 4024-4030. doi:10.1021/am300835p

Wang, T., Lv, R., Zhang, P., Li, C., and Gong, J. (2015a). Au nanoparticle sensitized ZnO nanopencil arrays for photoelectrochemical water splitting. *Nanoscale, 7*(1): 77-81. doi:10.1039/C4NR03735A

Wang, X., Zhi, L., and Müllen, K. (2008). Transparent, conductive graphene electrodes for dye-sensitized solar cells. *Nano Letters, 8*(1): 323-327. doi:10.1021/nl072838r

Wang, Y., Tang, W., Zhu, J., and Liu, J. (2015b). Strain induced change of band structure and electron effective mass in wurtzite ZnO: A first-principles study. *Computational Materials Science, 99*: 145-149. doi:10.1016/j.commatsci.2014.12.014

Wang, Y., Yang, R., Li, M., and Zhao, Z. (2015c). Hydrothermal preparation of highly porous carbon spheres from hemp (*Cannabis sativa L.*) stem hemicellulose for use in energy-related applications. *Industrial Crops and Products, 65*: 216-226. doi:10.1016/j.indcrop.2014.12.008

Wang, Z., Wu, S., Zhang, J., Chen, P., Yang, G., Zhou, X., . . . Zhang, H. (2012c). Comparative studies on single-layer reduced graphene oxide films obtained by electrochemical reduction and hydrazine vapor reduction. *Nanoscale Research Letters, 7*(1): 1-7. doi:10.1186/1556-276x-7-161

Wang, Z., Zhang, H., Wang, Z., Zhang, L., Yuan, J., Yan, S., and Wang, C. (2003). Structure and strong ultraviolet emission characteristics of amorphous ZnO films grown by electrophoretic deposition. *Journal of Materials Research, 18*(01): 151-155. doi:doi:10.1557/JMR.2003.0021

Warren, S. C., and Thimsen, E. (2012). Plasmonic solar water splitting. *Energy & Environmental Science, 5*(1): 5133-5146. doi:10.1039/C1EE02875H

Warren, S. C., Voïtchovsky, K., Dotan, H., Leroy, C. M., Cornuz, M., Stellacci, F., . . . Grätzel, M. (2013). Identifying champion nanostructures for solar water-splitting. *Nature Materials, 12*(9): 842-849. doi:10.1038/nmat3684

Watanabe, M., Aizawa, Y., Iida, T., Aida, T. M., Levy, C., Sue, K., and Inomata, H. (2005). Glucose reactions with acid and base catalysts in hot compressed water at 473K. *Carbohydrate research, 340*(12): 1925-1930.

Wei, X. Q., Man, B. Y., Liu, M., Xue, C. S., Zhuang, H. Z., and Yang, C. (2007). Blue luminescent centers and microstructural evaluation by XPS and Raman in ZnO thin films annealed in vacuum, N_2 and O_2. *Physica B: Condensed Matter, 388*(1–2): 145-152. doi:10.1016/j.physb.2006.05.346

Wei, Y., Du, H., Kong, J., Lu, X., Ke, L., and Sun, X. W. (2014). Multi-walled carbon nanotubes modified ZnO nanorods: a photoanode for photoelectrochemical cell. *Electrochimica Acta, 143*: 188-195. doi:10.1016/j.electacta.2014.08.026

Wei, Y., Ke, L., Kong, J., Liu, H., Jiao, Z., Lu, X., . . . Sun, X. W. (2012). Enhanced photoelectrochemical water-splitting effect with a bent ZnO nanorod photoanode decorated with Ag nanoparticles. *Nanotechnology, 23*(23): 235401. doi:10.1088/0957-4484/23/23/235401

Wolcott, A., Smith, W. A., Kuykendall, T. R., Zhao, Y., and Zhang, J. Z. (2009). Photoelectrochemical Study of Nanostructured ZnO Thin Films for Hydrogen Generation from Water Splitting. *Advanced Functional Materials, 19*(12): 1849-1856. doi:10.1002/adfm.200801363

Wu, Q., Li, W., Tan, J., Wu, Y., and Liu, S. (2015). Hydrothermal carbonization of carboxymethylcellulose: One-pot preparation of conductive carbon microspheres and water-soluble fluorescent carbon nanodots. *Chemical Engineering Journal, 266*: 112-120. doi:10.1016/j.cej.2014.12.089

Wu, S., and Zhang, H. (2014). Graphene oxides and reduced graphene oxide sheets: synthesis, characterization, fundamental properties, and applications. In Y. W. Wu, Z. Shen, & T. Yu (Eds.), *Two-Dimensional Carbon - Fundamental Properties, Synthesis, Characterization, and Applications* (pp. 297-328). USA: CRC Press.

Xiang, C., Papadantonakis, K. M., and Lewis, N. S. (2016). Principles and implementations of electrolysis systems for water splitting. *Materials Horizons, 3*(3): 169-173. doi:10.1039/C6MH00016A

Xiao, L.-P., Shi, Z.-J., Xu, F., and Sun, R.-C. (2012). Hydrothermal carbonization of lignocellulosic biomass. *Bioresource technology, 118*: 619-623.

Xie, G., Zhang, K., Guo, B., Liu, Q., Fang, L., and Gong, J. R. (2013). Graphene-based materials for hydrogen generation from light-driven water splitting. *Advanced Materials, 25*(28): 3820-3839. doi:10.1002/adma.201301207

Xu, F., Lu, Y., Xia, L., Xie, Y., Dai, M., and Liu, Y. (2009a). Seed layer-free electrodeposition of well-aligned ZnO submicron rod arrays via a simple aqueous electrolyte. *Materials Research Bulletin, 44*(8): 1700-1708. doi:10.1016/j.materresbull.2009.04.002

Xu, F., Lu, Y., Xie, Y., and Liu, Y. (2009b). Controllable morphology evolution of electrodeposited ZnO nano/micro-scale structures in aqueous solution. *Materials & Design, 30*(5): 1704-1711. doi:10.1016/j.matdes.2008.07.024

Xu, L., Guo, Y., Liao, Q., Zhang, J., and Xu, D. (2005). Morphological control of ZnO nanostructures by electrodeposition. *The Journal of Physical Chemistry B, 109*(28): 13519-13522. doi:10.1021/jp051007b

Xue, B., Liang, Y., Donglai, L., Eryong, N., Congli, S., Huanhuan, F., . . . Xiaosong, S. (2011). Electrodeposition from ZnO nano-rods to nano-sheets with only zinc

nitrate electrolyte and its photoluminescence. *Applied Surface Science, 257*(24): 10317-10321. doi:10.1016/j.apsusc.2011.05.132

Yang, H., Yan, R., Chen, H., Lee, D. H., and Zheng, C. (2007). Characteristics of hemicellulose, cellulose and lignin pyrolysis. *Fuel, 86*(12): 1781-1788.

Yang, J.-S., and Wu, J.-J. (2017). Low-potential driven fully-depleted $BiVO_4$/ZnO heterojunction nanodendrite array photoanodes for photoelectrochemical water splitting. *Nano Energy, 32*: 232-240. doi:10.1016/j.nanoen.2016.12.039

Yang, J., Wang, D., Han, H., and Li, C. (2013). Roles of Cocatalysts in Photocatalysis and Photoelectrocatalysis. *Accounts of Chemical Research, 46*(8): 1900-1909. doi:10.1021/ar300227e

Yang, K., Xu, C., Huang, L., Zou, L., and Wang, H. (2011). Hybrid nanostructure heterojunction solar cells fabricated using vertically aligned ZnO nanotubes grown on reduced graphene oxide. *Nanotechnology, 22*(40): 405401.

Yang, L. L., Zhao, Q. X., Willander, M., Liu, X. J., Fahlman, M., and Yang, J. H. (2010). Origin of the surface recombination centers in ZnO nanorods arrays by X-ray photoelectron spectroscopy. *Applied Surface Science, 256*(11): 3592-3597. doi:10.1016/j.apsusc.2009.12.160

Yang, M.-Q., and Xu, Y.-J. (2013). Basic principles for observing the photosensitizer role of graphene in the graphene–semiconductor composite photocatalyst from a case study on graphene–ZnO. *The Journal of Physical Chemistry C, 117*(42): 21724-21734. doi:10.1021/jp408400c

Yang, M.-Q., Zhang, N., Pagliaro, M., and Xu, Y.-J. (2014). Artificial photosynthesis over graphene-semiconductor composites. Are we getting better? *Chemical Society Reviews, 43*(24): 8240-8254. doi:10.1039/C4CS00213J

Yang, X., Wolcott, A., Wang, G., Sobo, A., Fitzmorris, R. C., Qian, F., . . . Li, Y. (2009). Nitrogen-doped ZnO nanowire arrays for photoelectrochemical water splitting. *Nano Letters, 9*(6): 2331-2336. doi:10.1021/nl900772q

Ye, S., Wang, R., Wu, M.-Z., and Yuan, Y.-P. (2015). A review on g-C_3N_4 for photocatalytic water splitting and CO_2 reduction. *Applied Surface Science, 358, Part A*: 15-27. doi:10.1016/j.apsusc.2015.08.173

Yi, Z., Guofeng, C., Ma, W., and Wei, W. (2008). Effect of external bias voltage and coating thickness on the photocatalytic activity of thermal sprayed TiO_2 coating. *Progress in Organic Coatings, 61*(2–4): 321-325. doi:10.1016/j.porgcoat.2007.09.030

Yin, Z., Wu, S., Zhou, X., Huang, X., Zhang, Q., Boey, F., and Zhang, H. (2010). Electrochemical deposition of ZnO nanorods on transparent reduced graphene oxide electrodes for hybrid solar cells. *Small, 6*(2): 307-312.

Yu, S.-H., Cui, X., Li, L., Li, K., Yu, B., Antonietti, M., and Cölfen, H. (2004). From starch to metal/carbon hybrid nanostructures: hydrothermal metal‐catalyzed carbonization. *Advanced Materials, 16*(18): 1636-1640.

Yu, W., Zhang, J., and Peng, T. (2016). New insight into the enhanced photocatalytic activity of N-, C- and S-doped ZnO photocatalysts. *Applied Catalysis B: Environmental, 181*: 220-227. doi:10.1016/j.apcatb.2015.07.031

Yu, Y., He, T., Guo, L., Yang, Y., Guo, L., Tang, Y., and Cao, Y. (2015). Efficient visible-light photocatalytic degradation system assisted by conventional Pd catalysis. *Scientific reports, 5*: 9561. doi:10.1038/srep09561

Yun, H. J., Paik, T., Diroll, B., Edley, M. E., Baxter, J. B., and Murray, C. B. (2016). Nanocrystal Size-Dependent Efficiency of Quantum Dot Sensitized Solar Cells in the Strongly Coupled CdSe Nanocrystals/TiO_2 System. *ACS Applied Materials & Interfaces, 8*(23): 14692-14700. doi:10.1021/acsami.6b05552

Yusoff, N., Kumar, S. V., Pandikumar, A., Huang, N. M., Marlinda, A. R., and An'amt, M. N. (2015). Core-shell Fe_3O_4-ZnO nanoparticles decorated on reduced graphene oxide for enhanced photoelectrochemical water splitting. *Ceramics International, 41*(3, Part B): 5117-5128. doi:10.1016/j.ceramint.2014.12.084

Zandi, O., and Hamann, T. W. (2016). Determination of photoelectrochemical water oxidation intermediates on haematite electrode surfaces using operando infrared spectroscopy. *Nature Chemistry, 8*(8): 778-783. doi:10.1038/nchem.2557

Zeng, K., and Zhang, D. (2010). Recent progress in alkaline water electrolysis for hydrogen production and applications. *Progress in Energy and Combustion Science, 36*(3): 307-326. doi:10.1016/j.pecs.2009.11.002

Zhang, C., Shao, M., Ning, F., Xu, S., Li, Z., Wei, M., . . . Duan, X. (2015a). Au nanoparticles sensitized ZnO nanorod@nanoplatelet core–shell arrays for enhanced photoelectrochemical water splitting. *Nano Energy, 12*: 231-239. doi:10.1016/j.nanoen.2014.12.037

Zhang, J., Ma, H., and Liu, Z. (2017). Highly efficient photocatalyst based on all oxides WO_3/Cu_2O heterojunction for photoelectrochemical water splitting. *Applied Catalysis B: Environmental, 201*: 84-91. doi:10.1016/j.apcatb.2016.08.025

Zhang, K., Zhang, Y., and Wang, S. (2013a). Enhancing thermoelectric properties of organic composites through hierarchical nanostructures. *Scientific reports, 3*: 3448. doi:10.1038/srep03448

Zhang, L., Cheng, H., Zong, R., and Zhu, Y. (2009a). Photocorrosion suppression of ZnO nanoparticles via hybridization with graphite-like carbon and enhanced photocatalytic activity. *The Journal of Physical Chemistry C, 113*(6): 2368-2374. doi:10.1021/jp807778r

Zhang, L., Du, L., Cai, X., Yu, X., Zhang, D., Liang, L., . . . Tan, S. (2013b). Role of graphene in great enhancement of photocatalytic activity of ZnO nanoparticle–graphene hybrids. *Physica E: Low-dimensional Systems and Nanostructures, 47*: 279-284.

Zhang, L., Wang, Q., Wang, B., Yang, G., Lucia, L. A., and Chen, J. (2015b). Hydrothermal carbonization of corncob residues for hydrochar production. *Energy & Fuels, 29*(2): 872-876.

Zhang, R., Yin, P.-G., Wang, N., and Guo, L. (2009b). Photoluminescence and Raman scattering of ZnO nanorods. *Solid State Sciences, 11*(4): 865-869. doi:10.1016/j.solidstatesciences.2008.10.016

Zhang, W.-D., Jiang, L.-C., and Ye, J.-S. (2009c). Photoelectrochemical study on charge transfer properties of ZnO nanowires promoted by carbon nanotubes. *The Journal of Physical Chemistry C, 113*(36): 16247-16253. doi:10.1021/jp905500n

Zhang, X., Qin, J., Xue, Y., Yu, P., Zhang, B., Wang, L., and Liu, R. (2014). Effect of aspect ratio and surface defects on the photocatalytic activity of ZnO nanorods. *Scientific reports, 4*: 4596. doi:10.1038/srep04596

Zhang, Y., Chen, Z., Liu, S., and Xu, Y.-J. (2013c). Size effect induced activity enhancement and anti-photocorrosion of reduced graphene oxide/ZnO composites for degradation of organic dyes and reduction of Cr(VI) in water. *Applied Catalysis B: Environmental, 140–141*: 598-607. doi:10.1016/j.apcatb.2013.04.059

Zhang, Y., Zhang, L., and Zhou, C. (2013d). Review of Chemical Vapor Deposition of Graphene and Related Applications. *Accounts of Chemical Research, 46*(10): 2329-2339. doi:10.1021/ar300203n

Zhang, Z., Dua, R., Zhang, L., Zhu, H., Zhang, H., and Wang, P. (2013e). Carbon-layer-protected cuprous oxide nanowire arrays for efficient water reduction. *ACS Nano, 7*(2): 1709-1717. doi:10.1021/nn3057092

Zhang, Z., and Yates, J. T. (2012). Band Bending in Semiconductors: Chemical and Physical Consequences at Surfaces and Interfaces. *Chemical Reviews, 112*(10): 5520-5551. doi:10.1021/cr3000626

Zhang, Z., and Zhao, Z. K. (2010). Microwave-assisted conversion of lignocellulosic biomass into furans in ionic liquid. *Bioresource technology, 101*(3): 1111-1114. doi:10.1016/j.biortech.2009.09.010

Zhao, G., Wen, T., Chen, C., and Wang, X. (2012). Synthesis of graphene-based nanomaterials and their application in energy-related and environmental-related areas. *RSC Advances, 2*(25): 9286-9303. doi:10.1039/C2RA20990J

Zhong, M., Kim, E. K., McGann, J. P., Chun, S.-E., Whitacre, J. F., Jaroniec, M., . . . Kowalewski, T. (2012). Electrochemically active nitrogen-enriched nanocarbons with well-defined morphology synthesized by pyrolysis of self-assembled block copolymer. *Journal of the American Chemical Society, 134*(36): 14846-14857. doi:10.1021/ja304352n

Zhou, M., Wang, Y., Zhai, Y., Zhai, J., Ren, W., Wang, F., and Dong, S. (2009). Controlled synthesis of large-area and patterned electrochemically reduced graphene oxide films. *Chemistry – A European Journal, 15*(25): 6116-6120. doi:10.1002/chem.200900596

Zhu, H., Iqbal, J., Xu, H., and Yu, D. (2008). Raman and photoluminescence properties of highly Cu doped ZnO nanowires fabricated by vapor-liquid-solid process. *The Journal of Chemical Physics, 129*(12): 124713. doi:10.1063/1.2981050

Zhu, K., Kopidakis, N., Neale, N. R., van de Lagemaat, J., and Frank, A. J. (2006). Influence of Surface Area on Charge Transport and Recombination in Dye-Sensitized TiO_2 Solar Cells. *The Journal of Physical Chemistry B, 110*(50): 25174-25180. doi:10.1021/jp065284+

Zhu, X., Qian, F., Liu, Y., Zhang, S., and Chen, J. (2015). Environmental performances of hydrochar-derived magnetic carbon composite affected by its carbonaceous precursor. *RSC Advances, 5*(75): 60713-60722. doi:10.1039/C5RA07339A

Zhu, Y., Murali, S., Cai, W., Li, X., Suk, J. W., Potts, J. R., and Ruoff, R. S. (2010). Graphene and graphene oxide: Synthesis, properties, and applications. *Advanced Materials, 22*(35): 3906-3924. doi:10.1002/adma.201001068

Zi, M., Zhu, M., Chen, L., Wei, H., Yang, X., and Cao, B. (2014). ZnO photoanodes with different morphologies grown by electrochemical deposition and their dye-sensitized solar cell properties. *Ceramics International, 40*(6): 7965-7970. doi:10.1016/j.ceramint.2013.12.146

Znaidi, L. (2010). Sol–gel-deposited ZnO thin films: a review. *Materials Science and Engineering: B, 174*(1–3): 18-30. doi:10.1016/j.mseb.2010.07.001

LIST OF PUBLICATIONS AND PAPERS PRESENTED

1. Teh, S. J., Hamid, S. B. A., Lai, C. W., and Lim, Y. S. (2015). $ZnCl_2$/NaCl-Catalysed Hydrothermal Carbonisation of Glucose and Oil Palm Shell Fiber. *Nanoscience and Nanotechnology Letters, 7*(7): 611-615. doi:10.1166/nnl.2015.2000
2. Teh, S. J., Lai, C. W., and Hamid, S. B. A. (2016). Novel layer-by-layer assembly of rGO-hybridised ZnO sandwich thin films for the improvement of photo-catalysed hydrogen production. *Journal of Energy Chemistry, 25*(2): 336-344. doi:10.1016/j.jechem.2016.01.009